THE PRACTICAL IMPLEMENTATION OF A RETRODIRECTIVE CROSS-EYE JAMMER BY USING SOFTWARE-DEFINED RADIO (SDR)

by

Frans-Paul Pieterse

Submitted in partial fulfillment of the requirements for the degree
Master of Engineering (Electronic Engineering)

in the

Department of Electrical, Electronic and Computer Engineering
Faculty of Engineering, Built Environment and Information Technology

UNIVERSITY OF PRETORIA

January 2022

SUMMARY

THE PRACTICAL IMPLEMENTATION OF A RETRODIRECTIVE CROSS-EYE JAMMER BY USING SOFTWARE-DEFINED RADIO (SDR)

by

Frans-Paul Pieterse

Supervisor(s):	Prof. W. P. du Plessis
Department:	Electrical, Electronic and Computer Engineering
University:	University of Pretoria
Degree:	Master of Engineering (Electronic Engineering)
Keywords:	Angular deception, cross-eye, electronic attack (EA), electronic countermeasures (ECM), electronic warfare (EW), glint, monopulse, radar, wavefront distortion.

Radar-guided missiles have the potential to cause extreme damage to vital military assets. Although traditional deception techniques can deceive radars in range and Doppler shift, only a few methods can deceive them in angle. Cross-eye jamming was identified as a possible countermeasure against angular radar threats. This electronic attack (EA) method works by artificially creating the worst case of glint in angular radars.

Numerous analyses of cross-eye jamming exist in the literature. The earlier analyses were derivative glint analyses that made two incorrect assumptions. The first was to use linear fits to the monopulse antenna patterns, which is only valid when the target platform is on broadside of the radar. The second was to assume that the target platform is an infinite distance from the radar, which is not possible. The analyses also did not consider retrodirectivity. It was only during a later cross-eye jamming analysis that the limitations were identified and corrected. The limitations in the analysis could have been identified much sooner if practical measurements were made. The extended cross-eye jamming analysis made fewer assumptions and was proven accurate by numerous simulations and some experimental results. However, the only available experiments where the radar rotation was

considered did not implement true retrodirectivity but simulated it by combining isolated channel measurements. A need was identified for the development of a truly-retrodirective cross-eye jammer in a laboratory environment to expand the body of knowledge available about cross-eye jamming. The cost-effective jammer would be used to identify any real-world effects or anomalies that could not be predicted by the extended analysis or identified by simulation.

This dissertation presents the development of a truly-retrodirective cross-eye jammer by using a software-defined radio (SDR). The development is accompanied by a method of calibrating the cross-eye jammer to obtain the ideal magnitude factor and phase difference between the retrodirective paths by minimising the magnitude of the sum-channel return of a monopulse radar. The developed system was tested in an anechoic environment against a self-implemented phase-comparison monopulse radar. It was shown that significant angular errors could be induced. The angular errors were larger than 10° at broadside of the radar. This equated to a minimum miss-distance of around 1 m at a range of 6 m. It was shown that a cross-eye gain of around ten was obtained, which resulted in the indicated angle of the radar never becoming zero, regardless of the radar rotation. This suggested that tracking radars, such as that used by active homing missiles, would lose lock on the target platform. Further experiments also proved the jammer to be retrodirective, with large angular errors for all rotations of the jammer antennas. All results correlated very well with that predicted by the extended analysis, with only minor deviations between radar rotations of 0° and 5°. After further investigation, it was concluded that the deviations were most likely caused by mutual coupling between the radar antennas and were not caused by a reduction in the performance of the jammer.

ACKNOWLEDGEMENTS

I would like to thank the Radar and Electronic Warfare team at the Council for Scientific and Industrial Research (CSIR) for the use of their anechoic chamber and facilities. I wish to thank Johann de Jager for organising the use of the facilities and Jacques Cilliers for providing us with the antennas that were used in the measurements.

I would like give a myriad of thanks to Professor Warren P. du Plessis for being the best postgraduate supervisor that a student could wish for. Not only did his guidance and support help me to the reach my postgraduate goals, but his contagious passion for radar and electronic warfare sparked my interest for the field.

I sincerely thank my good friends, Juandré Bester and Heinrich Laue for all their friendship, contributions, and support. I also thank them for reviewing the critical content and formatting of this dissertation.

I thank my parents, Rina and Frans Pieterse for all their love and support. I would never have reached this point without them.

I would like to give special thanks to my love, Catherine Stow. Thank you for all your love, and for always believing in me. I would also want to thank Catherine for reviewing the language in this dissertation.

Finally, I want to thank my Lord, Jesus Christ. Thank You for the talents that You bestowed upon me and thank You for placing such driven and amazing people in my life.

LIST OF ABBREVIATIONS

AAM	air-to-air missile
ADC	analogue-to-digital converter
AGC	automatic gain control
AoA	angle of arrival
ASM	anti-ship missile
ATC	air traffic control
AWGN	additive white Gaussian noise
CLI	command line interface
CSIR	Council for Scientific and Industrial Research
CW	continuous wave
DAC	digital-to-analogue converter
DF	direction-finding
DRFM	digital radio-frequency memory
DSP	digital signal processor
EA	electronic attack
EJ	escort jamming
ELINT	electronic intelligence
EM	electromagnetic
EMS	electromagnetic spectrum
EP	electronic protection
ES	electronic support
EW	electronic warfare
FFT	fast Fourier transform

FNBW	first null beamwidth
FPGA	field-programmable gate array
GPS	Global Positioning System
GUI	graphical user interface
IFFT	inverse fast Fourier transform
IR	infrared
JSR	jammer-to-signal ratio
LFM	linear frequency modulation
RCS	radar cross section
RF	radio-frequency
RGPO	range gate pull off
SAM	surface-to-air missile
SDR	software-defined radio
SLL	sidelobe level
SNR	signal-to-noise ratio
SOJ	stand-off jamming
SPJ	self-protection jamming
SQP	sequential quadratic programming
VGPO	velocity gate pull off

TABLE OF CONTENTS

CHAPTER 1 INTRODUCTION

1.1 PROBLEM STATEMENT

1.1.1 Context of the problem

Missiles can do substantial damage to the military by destroying some of its most vital assets. Two vulnerable sectors of the military, with regards to this, are its air force and navy. A surface-to-air missile (SAM) or air-to-air missile (AAM) can destroy the largest of aircraft [1]. If the crew does not react fast enough to the threat, this may result in death. Furthermore, if the crew does manage to escape from the aircraft in time, they run the risk of being captured and interrogated by their adversaries [2]. Similarly, an anti-ship missile (ASM) can sink enormous naval vessels [3]. Unlike military aircraft, large ships have very little manoeuvrability, making them even more vulnerable to missile threats.

Missiles can be divided into two categories with regards to target pursuit. Those in the first category do not pose a threat to aircraft or moving ships as they use means such as the Global Positioning System (GPS) to attack targets with fixed locations [3]. However, those in the second category use specialised sensors and guidance systems to track and pursue moving targets [1], [3]. Active radar seekers are predominantly used on missiles that have larger operating ranges [4].

Previous radar-guided missiles either used conical scan, lobe switching or monopulse radar to track their targets, while modern systems tend to use only monopulse [1], [4]. Monopulse is suggested as a good model for testing angular deception techniques against, as it is much more immune to angular countermeasures than sequential lobing and conical scan radars [4], [5]. The beams of monopulse and sequential lobing radars are formed in the same way. The difference is that the radar return is measured simultaneously at all the beams in the case of monopulse, where it is measured separately, and at different time instances, at each beam for sequential lobing [4], [5]. This suggests that sequential

lobing radars are susceptible to countermeasures that vary the amplitude of the repeated radar return in time, where monopulse radars are not affected by such threats at all [1]. Another reason why monopulse processing is very robust is that the error signal is created in the form of a ratio, resulting in the performance of the radar being independent of signal strength [4].

Numerous techniques of deceiving radars in range and Doppler shift exist. These include noise jamming and multiple false targets in both range and Doppler shift [1], [6], [7]. More advanced forms of deception jamming are range gate pull off (RGPO) and velocity gate pull off (VGPO), which can be very efficient – mainly when used in conjunction [1]. The problem is that very few countermeasures can deceive radars in angle and are all limited in certain ways [1], [8]. Countermeasures, such as chaff and towed decoys, are expendable and are therefore limited to the number of times that they can be used before requiring replacement [1], [6], [8].

Cross-polarisation jamming and cross-eye jamming have been identified as potential active countermeasures against angular radars, with cross-eye jamming having the fewest disadvantages in the opinion of at least one researcher [8]. Although both methods require relatively high jammer-to-signal ratio (JSR) and very accurate calibration, cross-polarisation is also affected by reflections, which can change the polarity of the signals. Such reflections could potentially turn the jammer into a beacon, meaning that the jammer would not deceive radar systems but rather illuminate the platform that is intended to be protected [8]. This could potentially counteract the polarity of the antennas. In this regard, two examples of vulnerable platforms are ground- and naval-based operations, as both land and sea are enormous scattering surfaces. Even though a cross-eye jammer can also become a beacon if the phase offset between the jammer paths deviates too much from the ideal, reflections from the environment will not interfere with its performance, as the two retrodirective paths cancel. This is true under the assumption that the same phase centres are used for both reception and transmission [9].

1.1.2 Research gap

Numerous analyses of cross-eye jamming exist in the literature. However, most of the results are limited in some way – such as being confined to simulation [10]–[14]. Two authors suggested that cross-eye jamming measurements were made, but the results were never published [15], [16]. There are only a few incidences of published experimental cross-eye jamming results [14], [17]. In the two most recent publications, the effects of placing a cross-eye jammer in the presence of a monopulse radar

were investigated. Both experiments were conducted in anechoic chambers to reduce environmental effects [14], [17].

In the first study, the effects of each of the two jammer paths on a monopulse radar's sum- and difference-channel patterns were measured separately. The results were computationally combined after the measurement process was complete. The limitations were that the jammer paths were not operating simultaneously, removing the need for high isolation between them and the implementation was not truly-retrodirective – it did, however, simulate retrodirectivity [14].

In the second study, a signal generator was used to transmit a signal using two spaced-apart antennas. A 180° hybrid coupler was used to add the required phase shift to one of the signals before transmission [17]. Substantial limitations were present in this experiment. Firstly, the system did not use two jammer paths but rather transmitted predefined signals continuously like a beacon. This meant that the system had no retrodirectivity whatsoever. The second limitation was that the radar was never rotated in the presence of the jammer. This suggested that a cross-eye effect may only be obtained for a specific orientation of the radar relative to the jammer.

It is apparent that there is a need to implement a practical retrodirective cross-eye jammer to confirm the validity of previous analyses and ensure that no anomalies that were not predicted by these analyses occur during practical implementations. It can be argued that some of the limitations in previous analyses of cross-eye jamming could have been avoided or corrected had measurements been made [11], [12], [18]. The development of methods for implementing and calibrating retrodirective cross-eye jammers can also be used in future research to practically investigate other aspects of cross-eye jamming, such as platform skin-return and the effects of path-length differences when using multiloop configurations [19]–[21]. Ultimately, this research will contribute to the expansion of the available knowledge of cross-eye jamming.

1.2 RESEARCH OBJECTIVE AND QUESTIONS

The primary objective of this research was to develop a truly-retrodirective cross-eye jammer for laboratory experiments to validate previous cross-eye jamming analyses and test simulated results. A further objective was to determine whether anomalies would arise during practical implementations, as these could change the course of future cross-eye jamming work. The last objective was to determine

whether a low-cost software-defined radio (SDR) would have acceptable performance and stability to be used in the practical implementation of a cross-eye jammer.

In the pursuit of achieving these objectives, the following research questions were addressed.

1. Do the practical results from a retrodirective cross-eye jammer correspond to the results obtained from previous analyses and simulations?
2. Is it possible to obtain a cross-eye gain of more than five if a cross-eye jammer is implemented by using an SDR?
3. Can a retrodirective cross-eye jammer be calibrated without explicitly measuring the phases and amplitudes of the jammer paths?

The first research question is essential, as it requires the validation of the previous work. As discussed, practical results are needed to test previous analyses and determine if the assumptions in the analyses are correct. Results are also needed to determine if any anomalies arise that were not predicted by previous analyses.

Previous analyses suggested that a cross-eye gain of more than five can create a missile miss distance of at least 20 m for a standard fighter aircraft with a wingspan of 10 m if the jammer has no rotation relative to the radar [22]. Therefore, it is apparent that cross-eye gain is an essential metric of the performance of such a jammer, and the first objective was to implement a cross-eye jammer that could achieve a cross-eye gain of five or more by using an SDR. The significance of using an SDR is that it is a low-cost device that promotes rapid radio-frequency (RF) prototyping. Its use may promote and accelerate future cross-eye jamming research. However, there was uncertainty whether restrictions on such a device, such as phase and amplitude resolution or phase drift, might impair the implementation of an effective cross-eye jammer with it. It should be noted that SDRs were not developed for this application.

For a practical cross-eye jammer to be sufficient for the validation of previous analyses, it has to be retrodirective. This means that the performance of the jammer should not decrease when the jammer is rotated relative to a monopulse radar [13]. Therefore, another objective was to ensure that the implementation of the jammer was retrodirective.

The last objective was to develop a method of calibrating a retrodirective cross-eye jammer without explicitly measuring the phases and amplitudes of the jammer paths. Calibration can be a daunting and time-consuming task, requiring specialised equipment. Suppose the calibration can be done without explicitly measuring the amplitudes and phases of the paths. In that case, this will substantially reduce the complexity of the calibration process and remove the need for expensive measurement equipment during field measurements.

1.3 APPROACH

1.3.1 Hypotheses

It is expected that the practical results will deviate significantly from the traditional cross-eye jamming analyses but will show minimal deviation from the extended analysis. This is due to the extended analysis's consideration of retrodirectivity and the effects of realistic antenna patterns in the extreme cases of glint – aspects that were omitted by the traditional analyses [11], [13].

It is also expected that a cross-eye gain of more than five can be achieved by using a low-cost SDR, but only if the SDR channels are coherent and if the calibration is sufficient. It was shown that a cross-eye gain of ten could be achieved if the gain between jammer paths is less than 2 dB, while the phase-difference is within 5° of the ideal 180° [22]. This means that larger tolerances are allowable and will further compensate for adverse effects such as non-linearities of RF components and noise in the system.

Finally, it is expected that a cross-eye jammer can be calibrated without explicitly measuring the amplitudes and phases of its jammer paths if access to a monopulse radar and the measurements of its sum-channel magnitudes are available. As it is known through the theory that the cancellation of the jammer's retrodirective paths causes the magnitude of the sum-channel return to approach a minimum, it should be possible to adjust the magnitudes and phases of the jammer paths to practically mimic this effect [9].

1.3.2 Methodology

The following methodology was followed in pursuit of reaching the primary research objective.

1. **The implementation of a monopulse radar**

   A one-dimensional phase-comparison monopulse radar was implemented by using an SDR.

Pulse compression was added to increase the signal-to-noise ratio (SNR) of the radar and aid in detecting radar return signals. As the system was only used in an anechoic environment at a short range, a simple peak detector was implemented to determine whether a radar return signal was received.

2. **The calibration and characterisation of the radar**

   The radar was calibrated and characterised to prove its validity as a system to test angular deception methods against, improving the integrity of jammer measurements. The calibration was done by transmitting a continuous wave (CW) signal on broadside of the radar and digitally removing the phase offset between the radar elements while ensuring that the amplitudes are equal. The characterisation process was conducted by transmitting the CW pulse from a fixed position and rotating the radar. The monopulse ratio, sum- and difference-channel antenna pattern magnitudes were recorded for multiple radar angles.

3. **The implementation of a retrodirective repeater**

   A retrodirective repeater was implemented by using an SDR. Two antennas were connected to the two receive and two transmit channels of the SDR by using power dividers so that the system had a Van Atta configuration. On the back-end, the SDR was connected to a personal computer (PC), and GNU Radio was used to connect the jammer paths in software. Feedback reduction techniques and phase and gain control were digitally applied to the jammer paths through GNU Radio.

4. **The calibration of the retrodirective cross-eye jammer**

   The retrodirective repeater was transformed into a retrodirective cross-eye jammer using calibration. This was done by measuring the magnitude of the sum-channel return of the radar in the presence of the jammer while the radar and jammer were on each other's broadside. Phase offsets were added to one of the repeater paths until the magnitude of the sum-channel return was at a minimum. Similarly, the magnitude of the same path was adjusted until the magnitude of the sum-channel return reached a new, lower minimum. This led to the jammer having a phase difference approaching 180° between the jammer paths, with the paths being near-equal in magnitude. Under these conditions, the sum-channel return was minimised, resulting in the radar experiencing significant angular errors.

5. **Cross-eye measurement**

   The results were obtained by recording measurements in a tapered anechoic chamber, with the distance between the radar and jammer estimated as about 5 m. The purpose of the anechoic chamber was to remove environmental effects, such as reflections. The calibrated jammer was

placed at the opening of the tapered chamber, while the radar was placed inside the chamber on a positioner. While the jammer had no rotation, the radar was rotated to multiple angles where the monopulse ratio, sum- and difference channel magnitudes were measured. This set of measurements was made to confirm the cross-eye jammer's operation and obtain results that could be used to compare previous cross-eye analyses against.

6. **Retrodirectivity measurement**

   The monopulse radar was placed at the opening of the tapered anechoic chamber while the calibrated jammer was placed on the positioner. The radar rotation was kept at zero while the jammer was rotated to multiple angles. At each angle, monopulse measurements were recorded. This set of measurements was made to prove that the cross-eye jammer was retrodirective.

1.4 RESEARCH GOALS

Different cross-eye jamming analyses are given in the literature, but all make certain assumptions. For example, some assume that the extreme case of glint can be expressed by using linear fits to the monopulse antenna patterns [10], [11], [18]. Furthermore, most cross-eye jamming results were obtained by simulation [13], [22]. The few available experimental results are very restricted and did not implement retrodirectivity [14], [17]. The first goal of this research was to remove doubt as to which cross-eye jamming analyses are the most accurate and make the most accurate assumptions. The next goal was to develop a basic single-loop retrodirective cross-eye jammer on an affordable platform that can be altered and extended, as needed, for future research on the topic.

1.5 RESEARCH CONTRIBUTION

The following contributions were made to the body of knowledge currently available in the field of electronic warfare (EW) with respect to cross-eye jamming.

1. **A new low-cost method of implementing and calibrating a retrodirective cross-eye jammer by using an SDR**

   A new method of implementing a retrodirective cross-eye jammer by using an SDR and GNU Radio was presented. This was accompanied by a method of calibrating a cross-eye jammer without explicitly measuring the magnitudes and phases of the jammer paths. These methods can be used and extended on in future research to investigate other aspects of cross-eye jamming, such as the effects of using multiloop configurations.

2. **The validation of previous analyses**

   Monopulse measurements were made with the radar in the presence of a retrodirective cross-eye jammer. The data were processed, and the results were compared to the traditional and extended cross-eye jamming models. The practical results correlated well with the extended analysis in terms of cross-eye gain and induced angular error, proving its validity. It was also shown that no anomalies that the previous cross-eye jamming models could not predict occurred during the measurement process. This work proved that the extended analysis is a good model for the behaviour of a cross-eye jammer and that the assumptions that were made are correct. This model can be used with confidence in future cross-eye jamming research.

1.6 RESEARCH OUTPUTS

By the time of writing this, a conference paper was published, while a journal article was submitted. The conference paper was the first known publication that presented truly-retrodirective cross-eye jamming results [23]:

> F. Pieterse and W. P. du Plessis, "Retrodirective cross-eye jammer implementation using software-defined radio (SDR)," in 2021 IEEE Radar Conference (RadarConf21), 2021, pp. 1–4.

The journal article was submitted to the IEEE Transactions on Aerospace and Electronic Systems for peer review:

> F. Pieterse and W. P. du Plessis, "Implementation and Testing of a Retrodirective Cross-Eye Jammer" (submitted November 2021 and awaiting feedback).

1.7 OVERVIEW OF DISSERTATION

An overview of the content of this dissertation is given below.

Chapter 2

The theoretical background of radar and electronic warfare is presented. The chapter starts with the basic concepts of radar, after which more advanced techniques, such as pulse compression, Doppler processing and angular radar are discussed. EW is introduced, and passive and active countermeasures against radar systems are discussed. Angular deception techniques, including cross-polarisation jamming and cross-eye jamming, are explained. The section ends with an overview of essential hardware in EW and RF-prototyping.

Chapter 3

An analysis of phase-comparison monopulse radar is presented, after which different previous analyses are recreated to understand cross-eye jamming better. The effects of using different cross-eye parameters are then investigated by using simulation.

Chapter 4

The chapter starts with the implementation of a phase-comparison monopulse radar for angular deception testing. The development of a retrodirective repeater, with the ability to be configured as either a beacon or a cross-eye jammer, is then presented. The implementation includes the hardware choices and software design.

Chapter 5

The experimental setup and procedures that were used to obtain the results are discussed in this chapter. A new method of calibrating a retrodirective cross-eye jammer by minimising the sum-channel return of an available radar is also presented. The chapter ends with a method of calibrating the results for deviations of the practical measurement setup from the ideal experimental setup.

Chapter 6

The results that were obtained from the experiments in Chapter 5 are presented. The results include the monopulse antenna patterns as well as the results of the radar in the presence of the repeater for both the case where the radar antennas were rotated with the positioner, as well as the case where the repeater antennas were rotated.

Chapter 7

The work in the dissertation is summarised, and some of the main contributions are highlighted. The chapter ends with proposed future research based on the outcome of this dissertation.

CHAPTER 2 AN INTRODUCTION TO RADAR AND ELECTRONIC WARFARE

2.1 CHAPTER OVERVIEW

This chapter introduces and discusses radar and EW. The basic principles of radar are emphasised, and more advanced radar techniques such as pulse compression and Doppler processing are introduced. In addition to this, background theory on angular radars, focusing on monopulse radar, are given. Glint is introduced as a phenomenon that causes angular errors in radars and is significant as cross-eye jammers exploit its existence. EW can be divided into three categories, namely electronic attack (EA), electronic support (ES) and electronic protection (EP), with cross-eye jamming being considered as part of EA. Other EA methods that can induce angular errors in radars, including chaff, towed decoys and cross-polarisation jamming, are also highlighted in this chapter.

2.2 AN INTRODUCTION TO RADAR AND RADAR TECHNIQUES

2.2.1 The principles of radar

Radar is a technology that receives scattered electromagnetic (EM) energy to detect target platforms and extract valuable information about their whereabouts [5].

In the most basic case, as shown in Figure 2.1, a radar pulse is transmitted into the general direction of an expected target platform, after which the radar's receiver is enabled. If a platform is present, the radiated energy is reflected from the platform and received by the radar [24]. The period between the transmission of the pulse and its reception is used to determine the range of the target platform, as the approximate propagation velocity of EM radiation in air is known to be 2.998×10^8 m/s [5], [24], [25]. Note that the propagation velocity of EM radiation through air can be approximated to be the

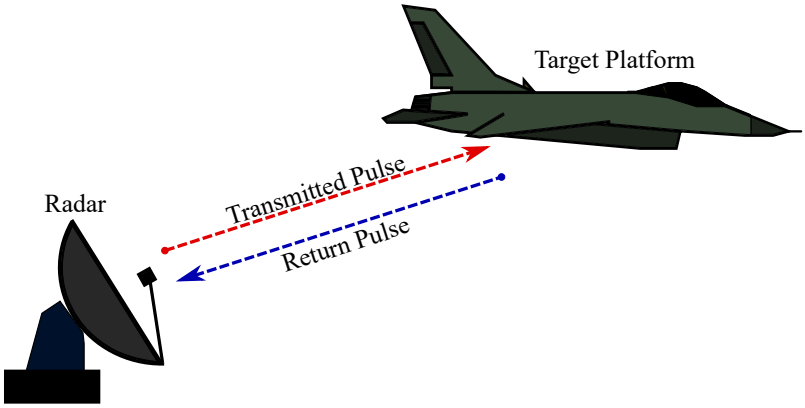

Figure 2.1. Illustration of radar operation.

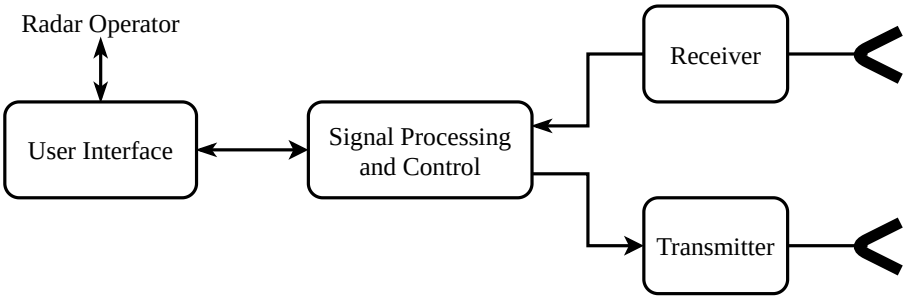

Figure 2.2. High-level flow diagram of a radar system.

same as that in a vacuum due to the low refraction index [25]. The range of the target platform can be expressed as

$$R = \frac{\Delta t}{2c}, \tag{2.1}$$

where R is the range between the radar and the platform, Δt is the time between the transmission and reception of the pulse, and c is the propagation velocity of EM radiation in a vacuum. The factor of two in the denominator is because the EM energy has to travel to the target platform and back to the radar.

A high-level overview of a radar system and subsystems can be seen in Figure 2.2 [24]. Firstly, as an active radar system has to transmit and receive EM energy in the form of a radar pulse, antennas are needed. Usually, only one antenna is used for transmission and reception, but two antennas are shown here to simplify the concept. A transmitter generates a radar signal and sends it to one of the

antennas where it is transmitted. Shortly after this, the receiver is enabled, and all signals of the same frequency as the radar are received through the second antenna. A digital system usually controls the transmission and reception. After the reception, the received signal undergoes signal processing to determine whether any echoed radar signal returned from a target. All results are then sent to a user interface, where a radar operator interprets it.

As the radar signal propagates through air, its power is attenuated [5]. When reaching the target, the platform absorbs some of its power, and the remainder is reflected. However, due to a complex platform's geometry, the signal is scattered into multiple directions, and only some of it is sent in the direction of the radar [5], [24]. Only a small fraction of the originally transmitted signal returns to the radar. The relationship between these variables can be described by the radar range equation [5], [24], which states that

$$P_r = \frac{P_t G_t \sigma A_e}{(4\pi)^2 R^4} , \tag{2.2}$$

where P_r is the power received of the return signal, P_t is the power of the transmitted signal, G_t is the gain of the transmitting antenna, A_e is the effected aperture of the receiving antenna, and R is the range of the target. The radar cross section (RCS) is denoted by σ, and is a metric of the effective area of the scattering surface that reflects EM radiation in the direction of the radar [5]. It should be noted that range is the variable that contributes the most to the signal's attenuation.

2.2.2 Pulse compression

For the best detection performance, a radar has to transmit the maximum amount of energy [5], [24]. This energy is directly proportional to the duration of transmission of a radar signal, which is determined by the width of each pulse and the amount of pulses used [5]. Figure 2.3 shows an uncompressed transmitted pulse, denoted by TX Pulse, with its three returned pulses in time. The transmitted pulse and its returns all have a pulsewidth of τ seconds.

Firstly, consider the transmitted pulse and its first return. It can be seen that if the return pulse was received before the transmission was complete, the two would have overlapped, leading to the first return not being detected. Therefore, the minimum separation in time between the transmitted pulse and its return for which the return can be distinguished is τ. This can be translated into a minimum range as

$$R_{min} = \frac{\tau c}{2} , \tag{2.3}$$

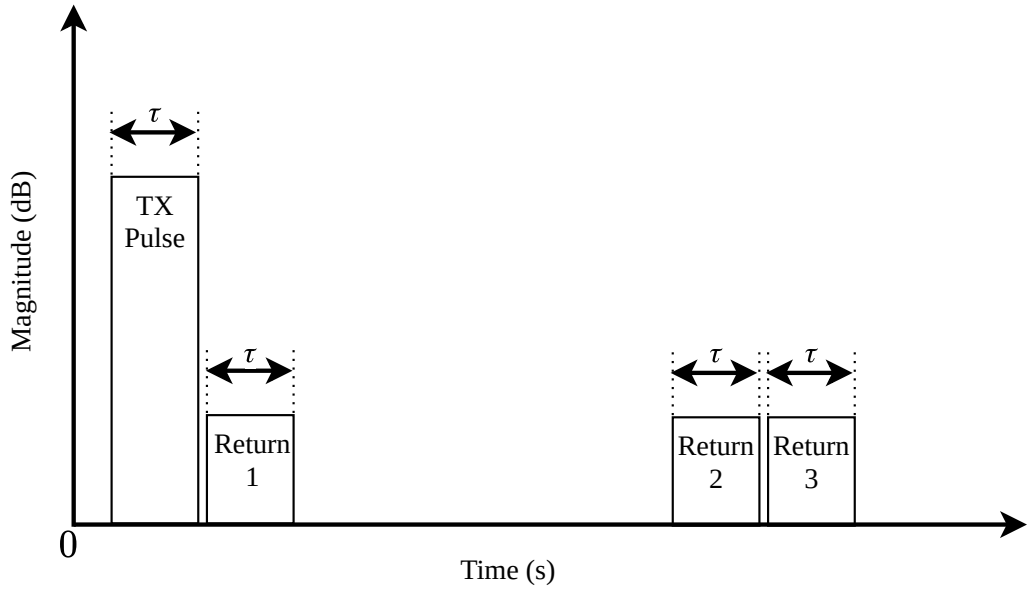

Figure 2.3. An illustration of minimum range and range resolution.

where c is the speed of light. If a target is closer to the radar than this range, its return will overlap with the initial radar pulse transmission.

Now consider the second and third return pulses. Similarly, as with the minimum range, if these two pulses have a separation of less than τ in time, they will overlap, and it would not be possible to distinguish between them. The equivalent of this time separation in range is called the range resolution and is the same as the minimum range if pulse compression is not used [5].

It is clear that by increasing the pulsewidth of a radar signal to improve its detection performance, the minimum range of a target is increased, and the range resolution of the radar is sacrificed [5], [24].

Pulse compression is a technique used by radar systems to improve its range resolution and increase the received signal's SNR while still using the maximum pulse width [5]. Pulse compression is implemented by modulating the radar pulse before transmission and correlating the received signal with the modulated pulse after receiving it. The modulation leads to the better utilisation of the bandwidth of the signal, improving the range resolution after correlation [5].

The most common pulse compression waveform used in radar systems is a linear frequency modulation

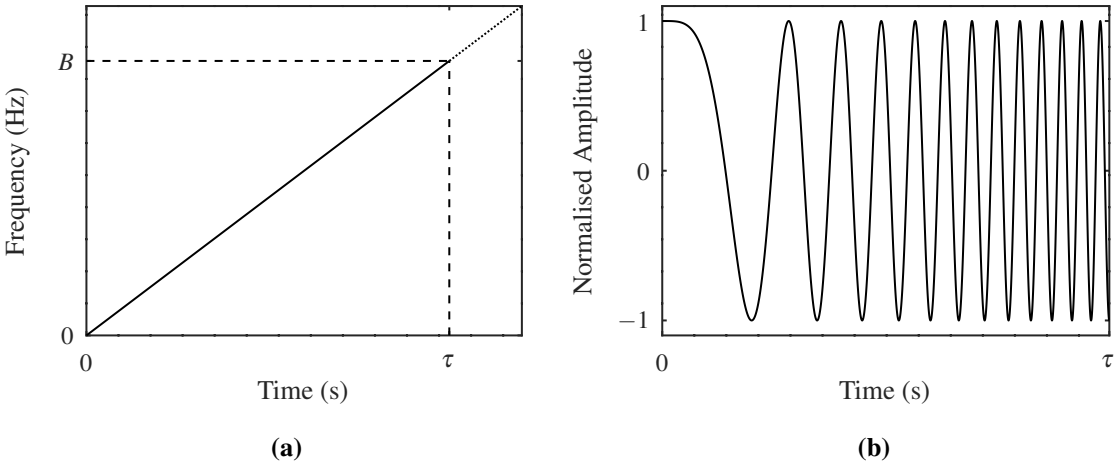

Figure 2.4. The (a) frequency and (b) time domain representations of a linear frequency modulation (LFM) pulse. The bandwidth and pulse width of the LFM signal is denoted by B and τ, respectively.

(LFM) pulse. This is due to improved time and Doppler sidelobe level (SLL) performance [5]. As the name suggests, the frequency of an LFM pulse changes linearly as a function of time, as can be seen in Figure 2.4(a). This frequency, assuming an up-chirp, can be expressed as

$$f(t) = \frac{B}{\tau} t \,, \tag{2.4}$$

where B is the bandwidth of the signal and τ is the pulse width. The phase corresponding to this frequency can be calculated by taking the integral of the angular frequency for time as

$$\begin{aligned} \phi(t) &= 2\pi \int \frac{B}{\tau} t \, dt \\ &= \frac{\pi B}{\tau} t^2 + \phi_0 \,, \end{aligned} \tag{2.5}$$

where ϕ_0 is an arbitrary constant phase that may be omitted. An arbitrary signal can be expressed in terms of its amplitude and phase as

$$p(t) = a(t) e^{j\phi(t)} \,. \tag{2.6}$$

By substituting (2.5) into (2.6) and assuming a constant amplitude, the function of an LFM signal that is not limited in time can be expressed as

$$p(t) = e^{j\frac{\pi B}{\tau} t^2} \,. \tag{2.7}$$

If a rectangular function is modulated onto the LFM waveform to make it causal, the resultant LFM pulse can be expressed as

$$p(t) = \text{rect}\left(\frac{t}{\tau} - \frac{1}{2}\right) e^{j\frac{\pi B}{\tau} t^2} \,, \tag{2.8}$$

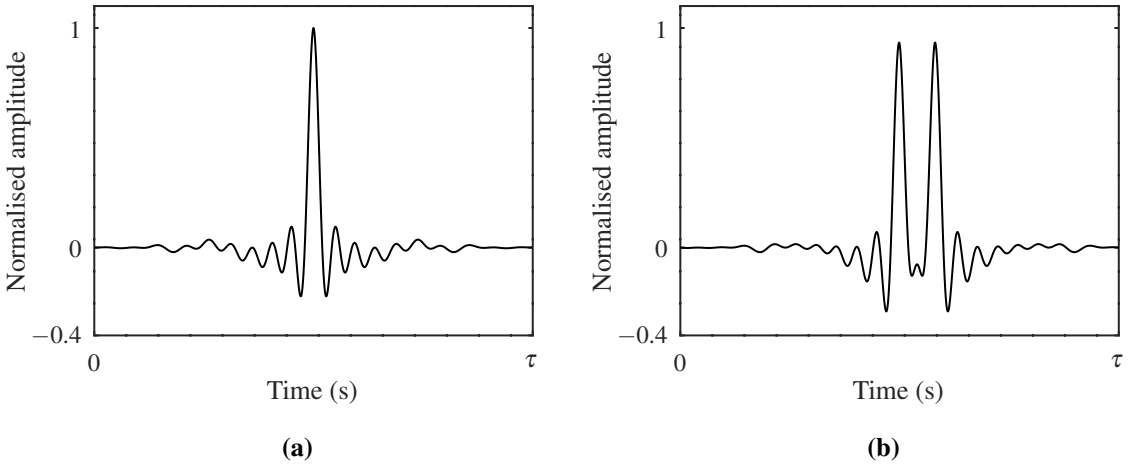

Figure 2.5. An illustration of (a) the autocorrelation of an LFM pulse and (b) the effect of pulse compression on the range resolution of a radar.

where the $1/2$ term is the rectangular function undergoing a shift in time to make the pulse causal [26]. An example of an LFM pulse's time-domain response is shown in Figure 2.4(b). It can be seen that the pulse has a sinusoidal nature with an increase of frequency as time progresses.

To complete the process of pulse compression, the received signal has to be correlated with the transmitted pulse [5]. The correlation increases the signal-to-noise ratio (SNR) as it averages out the noise [26]. In addition to this, the result of correlating the radar return with the transmitted pulse is that a pulse with a very narrow main lobe and low sidelobes levels is obtained [5]. This also increases the SNR as the lower sidelobes result in the main lobe having a larger magnitude. The width of the resultant pulse is equal to that of the transmitted. This is demonstrated in Figure 2.5(a), where the result of the autocorrelation of the LFM pulse is shown.

The effectiveness of pulse compression in improving range resolution is demonstrated in Figure 2.5(b), where two autocorrelated LFM pulses with a slight difference in delay were superposed. As range directly translates to time, it can be seen that the two targets can be within a fraction of a pulsewidth apart, and it would still be possible to distinguish them. It should be noted that autocorrelation is used in these demonstrations as an ideal representation of the potential practical result, where a received pulse is correlated with the transmitted pulse.

Finally, the measure of the level of pulse compression that is applied is called the pulse compression ratio. It is a ratio between the original pulsewidth of the signal and the width of the main lobe after correlation [5]. For example, if a pulse compression ratio of 10 is used, the system's effective range resolution will be improved by a factor of 10. In other terms, the width of the main lobe will be ten times narrower than that of the original pulse.

2.2.3 Pulse-Doppler radar

The Doppler effect is a phenomenon where a wave's frequency is different at an observer than at its source when there is relative motion between them [27]. This effect is generally utilised in radars to determine the radial velocity of target platforms, as a radar system's carrier frequency is chosen [5], [24]. This is done by extracting the Doppler information of a target from the radar return. The term radial velocity refers to that the target will likely never move precisely perpendicular to the radar's broadside, leading to a difference between its actual velocity and that perceived by the radar [5]. The relationship between the change in frequency, known as the Doppler shift, and the relative velocity between the radar and the target is given by

$$f_d = \frac{-2v_t}{\lambda}\,, \tag{2.9}$$

where f_d is the Doppler shift, v_t is the relative radial velocity, and λ is the wavelength of the signal that was transmitted by the radar [5]. In addition to determining the radial velocity of targets, Doppler processing is also used to distinguish moving target platforms from environmental clutter for ground-based radar systems [5]. This is possible since the platform in question (e.g. an aircraft) induces a Doppler shift, where objects in the environment (e.g. trees) are mostly stationary and do not cause large Doppler shifts [5]. When considering airborne radar, Doppler processing will have poor performance in the removal of clutter, as the reflections from the ground, which are significant, will produce Doppler shifts [24].

2.3 ANGULAR RADAR

Even though it is beneficial to know the range and velocity of a target platform, the exact location relative to the radar can be of extreme value. Angular radar systems can solve this problem by measuring the angle of arrival (AoA) of radar signals in azimuth and elevation [4], [5].

Angular radars are used by air traffic control (ATC) to determine the locations of multiple aircraft and use this information to avoid mid-air collisions [4]. In a military scenario, angular radar can be used to

detect and track adversarial target platforms. In addition to this, it is commonly used as a method of guiding long-range missiles to their targets [1].

Various implementations of angular radar exist, including sequential lobing and conical scan radars, but the most popular is arguably monopulse [4], [8].

2.3.1 Monopulse radar

Monopulse is an angular radar processing technique where the phases or amplitudes of radar return signals at multiple antennas are compared simultaneously to determine the angle of a target platform [4], [28]. The comparison is made by forming a monopulse ratio, where the difference-channel antenna pattern is divided by the sum-channel antenna pattern. The monopulse ratio of the exact monopulse processor is therefore given by

$$M(\theta) = \frac{D(\theta)}{S(\theta)}\,, \tag{2.10}$$

where $S(\theta)$ and $D(\theta)$ are the sum-channel and difference-channel antenna patterns, respectively.

The difference-channel is used as a measure of the angle of a target, where the sum-channel normalises this result and turns it into a ratio [4]. The way that the monopulse ratio is created makes monopulse more robust than other angular radar processors. Therefore, the angular information conveyed is not dependent on the strength of the received signal [4]. Note that the monopulse ratio will almost always result in a complex number. This is resolved by using only the real part of the monopulse ratio in the case of amplitude-comparison monopulse, and the imaginary part in the case of phase-comparison monopulse [4], [9]

2.3.1.1 Amplitude Comparison Monopulse

In amplitude-comparison monopulse radar, the angle of a target platform is determined by effectively comparing the radar return signal amplitudes at two antenna lobes and processing the results as ratios [4]. To do so, these antennas all have to have the same phase centre, and their lobes have to be squinted so that they partially overlap [4]. Two of these systems are usually used in conjunction to determine the angle of the target in both azimuth and elevation, therefore making the angular processing two-dimensional. Due to the squint, the effective patterns of the antenna will vary, even if the antennas are identical.

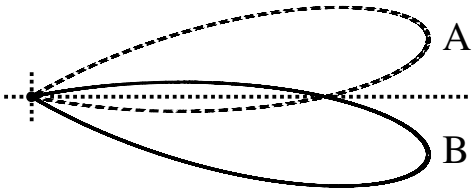

Figure 2.6. An illustration of the antenna lobes of a one-dimensional amplitude-comparison monopulse radar. It can be seen that both lobes have the same phase-centre.

Figure 2.6 shows the lobes of a one-dimensional amplitude comparison monopulse radar. If a pulse, $p(t)$, is received from an angle relative to broadside, θ, the sum-channel antenna pattern can be expressed as

$$S(\theta) = p(t)P_{\mathrm{A}}(\theta) + p(t)P_{\mathrm{B}}(\theta)\,, \tag{2.11}$$

where $P_{\mathrm{A}}(\theta)$ and $P_{\mathrm{B}}(\theta)$ are the effective patterns of A and B, respectively. Similarly, the difference-channel antenna pattern can be expressed as

$$D(\theta) = p(t)P_{\mathrm{A}}(\theta) - p(t)P_{\mathrm{B}}(\theta)\,. \tag{2.12}$$

From (2.11) and (2.12), the monopulse ratio is calculated as

$$M(\theta) = \Re\left\{\frac{p(t)P_{\mathrm{A}}(\theta) - p(t)P_{\mathrm{B}}(\theta)}{p(t)P_{\mathrm{A}}(\theta) + p(t)P_{\mathrm{B}}(\theta)}\right\}\,. \tag{2.13}$$

If lobes A and B are created by antennas with the same element pattern, and both are squinted to each side of the phase-centre by an angle of θ_s, the effective pattern at A can be written as $P_{\mathrm{A}}(\theta) = P(\theta - \theta_s)$, and the pattern at B can be written as $P_{\mathrm{B}}(\theta) = P(\theta + \theta_s)$. The monopulse ratio can therefore be simplified to

$$M(\theta) = \frac{P(\theta - \theta_s) - P(\theta + \theta_s)}{P(\theta - \theta_s) + P(\theta + \theta_s)}\,. \tag{2.14}$$

It is apparent from (2.14) that the monopulse ratio is independent of the incoming pulse itself and is only formed by comparing the effective antenna patterns at the angle from which the pulse is inbound [4]. Therefore, it is proven to be independent of signal strength. It should be noted that noise will still affect the accuracy of the result. In addition, the dependence of the monopulse ratio on solely the effective patterns can be detrimental, as any change to the immediate environment or installation platform can distort these patterns and lead to erroneous results.

2.3.1.2 Phase Comparison Monopulse

In phase-comparison monopulse radar, the phases of a radar return signal at multiple antenna elements are used to form the monopulse ratio. This is only possible if the phase-centres of the antenna elements

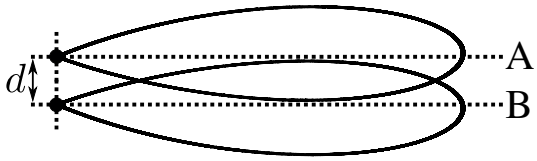

Figure 2.7. An illustration of the antenna lobes of a one-dimensional phase-comparison monopulse radar. The lobes have two different phase-centres that are spaced d m apart.

are spaced apart [9]. Figure 2.7 shows the lobes of a one-dimensional phase-comparison monopulse radar, where the antennas are spaced d m apart. If a signal is received on broadside of the radar, the pulse will have the same phase at both antennas. However, if the signal is received from a different angle, it will reach the antenna on the side from which it is inbound first before reaching the other antenna. This will create a phase difference between the return at each antenna. If a return pulse, with waveform $p(t)$, has a different phase at A than at B, the sum-channel can be expressed as

$$S(\theta) = p(t)e^{j\phi_{\mathrm{A}}(\theta)}P_{\mathrm{A}}(\theta) + p(t)e^{j\phi_{\mathrm{B}}(\theta)}P_{\mathrm{B}}(\theta)\,, \tag{2.15}$$

where $\phi_{\mathrm{A}}(\theta)$ and $\phi_{\mathrm{B}}(\theta)$ are the phases of the pulse at A and B. The element antenna patterns of A and B are given by $P_{\mathrm{A}}(\theta)$ and $P_{\mathrm{B}}(\theta)$, respectively. Similarly, the difference-channel can be expressed as

$$D(\theta) = p(t)e^{j\phi_{\mathrm{A}}(\theta)}P_{\mathrm{A}}(\theta) - p(t)e^{j\phi_{\mathrm{B}}(\theta)}P_{\mathrm{B}}(\theta)\,. \tag{2.16}$$

If the antenna patterns of the elements are equal, therefore $P_{\mathrm{A}}(\theta) = P_{\mathrm{B}}(\theta) = P(\theta)$, the monopulse ratio can be expressed as

$$M(\theta) = \Im\left\{\frac{e^{j\phi_{\mathrm{A}}(\theta)} - e^{j\phi_{\mathrm{B}}(\theta)}}{e^{j\phi_{\mathrm{A}}(\theta)} + e^{j\phi_{\mathrm{B}}(\theta)}}\right\}\,. \tag{2.17}$$

It can be seen that if the element antenna patterns are equal they will cancel when forming the monopulse ratio. Therefore, monopulse ratio is neither dependent on antenna patterns, nor signal strength, making it even more robust than in the amplitude-comparison case. A full analysis of phase-comparison monopulse radar is given in Chapter 3.

2.3.2 Glint

Glint is an angular error induced on radars that is caused by multiple scattering surfaces on a target platform. This occurs when each platform reflects the radar signal with a different amplitude and phase, distorting the wavefront of the radar [4], [5], [29]. The net effect is a linear offset between the location of the apparent and the actual target, as perceived by the radar [29].

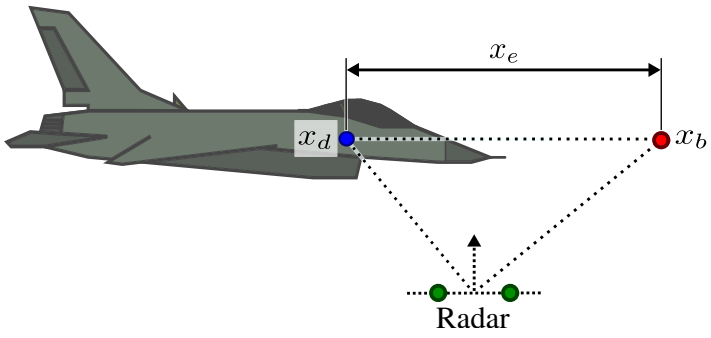

Figure 2.8. An illustration of how an angular radar perceives a target in the presence of glint.

This is shown in Figure 2.8, where just the x component is considered. When no glint is present, the x component of a target platform's position, as seen by the radar, is given by x_d. This position, known as the centroid, can be used as a reference point when determining the glint error. The balancing point, x_b, is the position that the radar perceives the target to be at in the presence of glint. The offset between the centroid and the balancing point is called the pointing error and is given by x_e [29].

When considering a case where glint is caused by point scatterers, the centroid of a platform relative to the radar can be expressed as

$$x_d = \Re\left\{\frac{\sum_{i=1}^{N} x_i A_i}{\sum_{i=1}^{N} A_i}\right\}, \tag{2.18}$$

where x_i is the x component of the i^{th} point scatterer, A_i is the amplitude of the field radiated by the i^{th} scatterer, and N is the number of point scatterers on the target [29]. The balancing point can be expressed as

$$x_b = \Re\left\{\frac{\sum_{i=1}^{N} x_i A_i e^{j\theta_i}}{\sum_{i=1}^{N} A_i e^{j\theta_i}}\right\}, \tag{2.19}$$

where θ_i is the phase of the radiated field by the i^{th} scatterer [29]. Lastly, the measure of the angular error, when considering just the x component, can be given by subtracting the balance point from the centroid. This is done as

$$x_e = x_d - x_b\ . \tag{2.20}$$

It should be noted that glint causes a fixed offset from the target and that the magnitude of the angular error on a radar will increase as the distance between the platform and the radar is decreased.

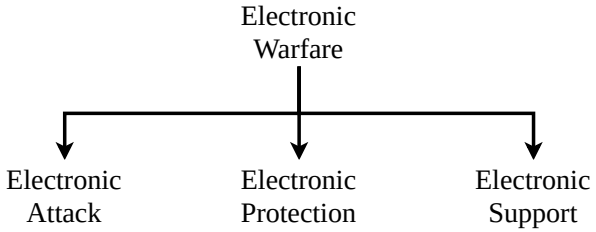

Figure 2.9. Branches of EW.

2.4 ELECTRONIC WARFARE

The term EW can be defined as the observation and manipulation of the electromagnetic spectrum (EMS) to gain benefit over an adversary [3]. As the EMS ranges from radio waves to gamma rays, with visible light and infrared (IR) in between [25], a large number of different systems is covered by this definition. Initially, EW was only restricted to radar waves, as it is used for communication and navigation [1], [2]. Later on, IR was added to the list when it was discovered that optical sensors could be used to detect IR-radiating heat sources – such as the jet engine of a fighter aircraft [3]. In the modern age that we live in, vast amounts of information are stored on computers. Most of which are connected to networks, and ultimately, the internet. Although cyber attacks are done to steal sensitive and valuable information about individuals or large entities, the military can also become vulnerable. Therefore, cyber security can also be considered as part of EW [1].

2.4.1 Classifications

EW can be branched into three different categories, namely EA, ES, and EP [3]. These branches can be seen in Figure 2.9.

EA can be described as the offensive part of EW as it is used to disrupt and deceive communication and navigation systems [3]. This is traditionally called jamming, and an example is noise jamming [1]. EP is the part of EW where countermeasures against EA are implemented to safeguard the operation of communication and navigation systems [3]. An example of this is sidelobe blanking [1]. Lastly, ES is the gathering of information and intelligence to gain an advantage over adversaries. ES is completely passive, as the EMS is only observed without transmitting anything [3]. One example of an ES system is an electronic intelligence (ELINT) system [1].

2.5 ELECTRONIC ATTACK

2.5.1 Passive jamming

Passive jamming refers to means of deceiving radar systems without transmitting signals [6]. The two most common passive methods used by airborne platforms to deceive radar systems towed decoys and chaff are both off-board [1]. This means that they are not installed on the platform that needs protection. The disadvantage of off-board systems like these is that they are expendable. If a towed decoy is shot out of the air, or if the chaff cartridges are empty, the platform is vulnerable to threats again [1].

2.5.1.1 Chaff

Chaff is a collection of millions of fibres that are each coated with a conductive layer [1]. These fibres are released as a cloud behind a fighter aircraft to create an enormous RCS, while the fighter quickly tries to escape [3]. The large RCS is formed due to the fibres being conductive and cut into certain lengths, which is each is usually half the wavelength of the expected radar signal. Multiple lengths are used to make it effective against a larger band of radar signals [1].

Except for limited times of use, chaff also has the disadvantage of being easily dispersed by wind, leaving the platform exposed. Additionally, most modern radar systems use pulse-Doppler processing and can easily distinguish between chaff and the actual platform [1].

2.5.1.2 Towed Decoys

A towed decoy is an aerodynamic missile-shaped craft that is towed behind an aircraft to mislead radar systems, as illustrated in Figure 2.10 [1]. The idea behind this is to create a second target platform behind the platform that is being protected. The problem is that modern radar systems can distinguish between a decoy and the real platform [1]. Note that the towed decoys referred to here are the traditional towed decoys that do not use jamming. Modern towed decoys have jammers installed and are considered as active countermeasures.

2.5.2 Active jamming

Active jamming is the transmission of EM signals to disrupt adverse signals or artificially modify how adversaries perceive them [1], [3], [6]. The advantage of active jamming, as opposed to passive

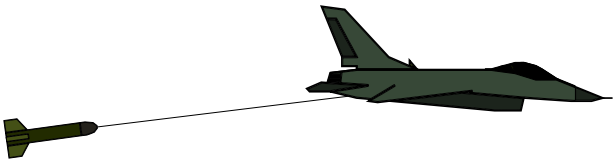

Figure 2.10. An illustration of a towed decoy. Note that a towed-decoy is usually much further behind an aircraft than shown here.

jamming, is that its use is infinite [1]. It remains operational for as long as an operator or a pilot keeps it switched on. Active jamming can either be off- or on-board.

Two off-board methods are stand-off jamming (SOJ) and escort jamming (EJ). The former is a method where the jammer is generally far from a radar, and out of reach for adversarial weapons. In EJ, an aircraft, usually with the sole purpose of jamming, accompanies other aircraft into the enemy territory. This creates a distraction so that allies can quickly penetrate the enemy territory without being detected [1]. Escorting aircraft can be equipped with more powerful jamming technology, as they generally do not carry missiles and can afford the extra payloads [1].

The most common form of jamming is self-protection jamming (SPJ), and is categorised as an onboard method, which means that the jammer is installed on the same platform that it aims to protect [3]. This creates the risk of a platform illuminating itself with EM radiation, leading to easier detection by adversaries [1].

2.5.2.1 Noise Jamming

Noise jamming is defined as the transmission of a signal with the purpose to obscure the signal of an adversary [3]. The optimal signal to use in noise jamming is additive white Gaussian noise (AWGN), as that corresponds to the noise in a standard RF receiver [3], [26].

Any transmitter can only transmit a finite amount of power, making it a vital resource to manage in any transmitter – especially a noise jammer [26]. There are two methods of applying noise jamming while considering the available power of the RF transmitter, and both are effective in different scenarios.

The first scenario is by transmitting a large amount of power over a very narrow frequency band and is

called spot jamming [1]. In this case, any signal that operates within the same band as the jammer will be completely obscured. However, when a signal with a large bandwidth or frequency agility is used, the signal will not only be available for use, it will also be apparent that there is a noise jamming source. Therefore, direction-finding (DF) could be used to determine the location of the jammer [1].

The second method is by spreading the power over a large band. The power at each frequency will be much lower and might only obscure signals partially, but the jammer will be more effective against wideband signals or signals with frequency agility [1]. This is known as barrage jamming [1].

2.5.2.2 False Target Creation

If a platform detects an adverse radar signal, it can be altered and transmitted back to the radar. Two primary modifications that are done are delaying the signal and adding a frequency offset [1]. By inducing a small delay in the signal, it can appear as if the target platform is further from the radar than what it is, misleading the radar in range. The frequency shift will result in the false target having a Doppler shift that differs from that of the actual target, misleading the radar in velocity [1]. To further add to the deception, multiple versions of the false target can be transmitted simultaneously, each with a different range and velocity. The modification to the signal can be described mathematically as

$$y(t) = x(t) \sum_{n=1}^{N} e^{j2\pi\Delta f_n (t-\Delta T_n)} , \tag{2.21}$$

where $x(t)$ is the intercepted radar signal and $y(t)$ is the signal transmitted back to the radar. The number of false is given by N, while ΔT_n is the time delay and Δf_n is the frequency adjustment of the n^{th} false target, respectively. Figure 2.11 demonstrates how three false targets can be created.

2.5.2.3 Range- and Velocity Gate Pull-Off

RGPO is an extension of false target creation, where the false target initially has the same apparent range and velocity as the platform, but with a much higher power to force the radar to reduce its reception gain by using automatic gain control (AGC) [1]. Therefore, the power level of the actual radar return is much lower than that of the false target, resulting in the radar only detecting the false target. The false target is gradually delayed in range to pull the radar's range gate away from the actual platform to follow the false target and lose its lock on the true platform [1], [3], [7]. This is usually followed by a fast manoeuvre by the target platform to escape safely [3]. VGPO works the same as RGPO, with the only difference being that the Doppler shift of the false target is changed, instead

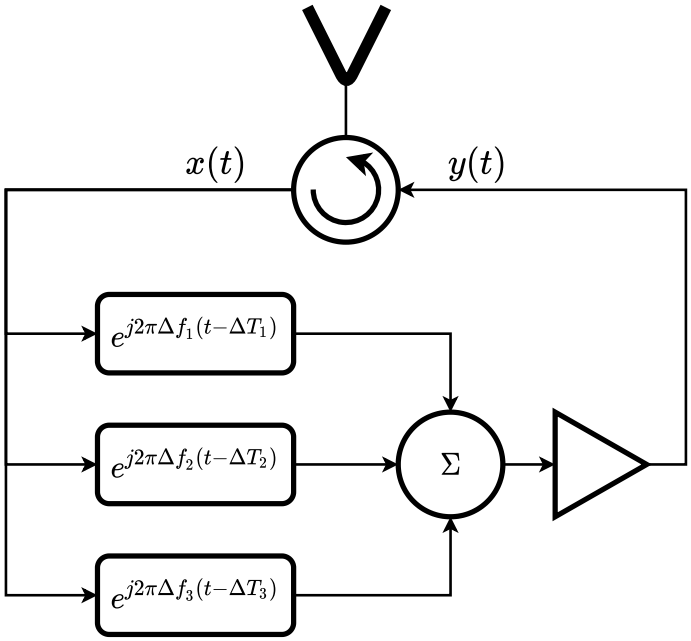

Figure 2.11. An illustration of how multiple false targets are created.

of the range, in an attempt to pull the velocity (or Doppler) gate of the radar away from the actual platform [1], [3], [7].

The two methods are seldom used separately, as both are needed simultaneously to mimic best how an actual target will react on a range-Doppler map [1]. The problem with both these methods and traditional false targets is that actual target platforms are complex in geometry. The RCS of such a platform, as observed by a radar, changes as the target manoeuvres [1]. Therefore, the appearance of an actual target on a range-Doppler map is very different from that of a single point scatterer (which is how false targets are perceived). This appearance changes as the range and velocity of the target changes [1]. Many false targets, placed together by sophisticated processors to mimic an actual target's appearance, will be needed to deceive modern radar systems.

RGPO and VGPO are also ineffective against angular radars [1]. Angular processors, such as monopulse, do not use a target platform's range or velocity to determine its angle – just the presence of a signal [4]. Therefore, any angular radar will perceive real and false targets to have the same angle, resulting in false targets acting as beacons for these radars to track platforms easily [4].

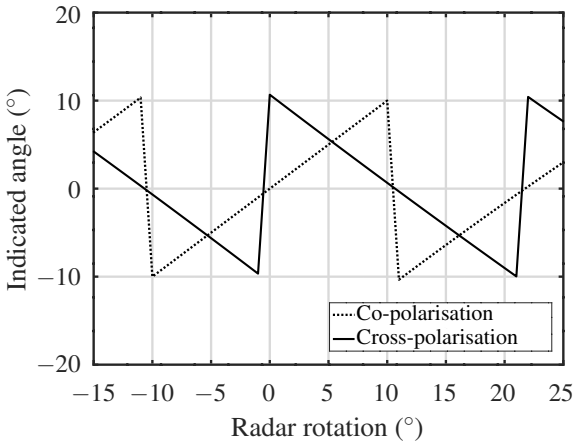

Figure 2.12. The effect of polarisation on the indicated angle of a monopulse radar.

2.5.3 Cross-polarisation jamming

Cross-polarisation jamming is an active EA method where the radar signal that arrives at a target platform is repeated back to the radar by using an antenna polarisation orthogonal to that of the radar [1], [3].

When considering a monopulse radar transmitting and receiving on a particular polarisation, the sum-channel has a peak at broadside, while the difference-channel has a null [4]. At the same patterns' orthogonal polarisation, the sum-channel has a null at broadside, while the difference-channel has a peak [1].

Therefore, if a jammer repeats the radar signal using the orthogonal polarisation, the radar will perceive the sum-channel as the difference-channel and vice versa [1]. Effectively, the monopulse ratio will be calculated by dividing the sum-channel by the difference-channel. This effect can be seen in Figure 2.12, where the indicated angle of a monopulse processor is shown as a function of the physical angle for two monopulse signals. The first is an arbitrary monopulse signal that is transmitted and received by using the same antenna polarisation. Therefore, the antenna pair is co-polarised. The second signal is identical to the first, but the receiving and transmitting antennas' polarisation are now orthogonal, therefore, cross-polarised. It is apparent that the second signal is a mirror of the first but with an angular offset. This offset is equal to half the first null beamwidth (FNBW) of the sum-channel.

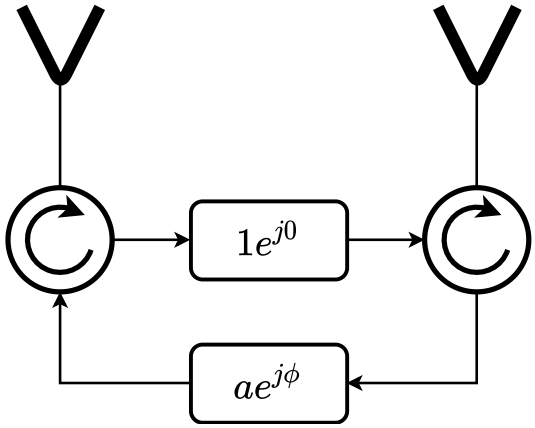

Figure 2.13. Retrodirective cross-eye paths.

There are a few limitations to cross-polarisation jamming. The first is that the jammer's polarisation has to be precisely orthogonal to that of the radar [1]. The slightest deviation from this will create a component in the same polarisation as the radar, resulting in a more substantial radar return. Therefore, the polarisation of the jamming antenna has to be controllable [1]. Movement by the platform on which the jammer is installed and reflections from parts of the platform can also affect the jammer's polarisation. However, the most significant limitation of cross-polarisation is its vulnerability to multipath – especially the ground. Reflections from the environment can depolarise the jammer signal, which will add to the original radar signal and turn the jammer into a beacon [8].

The last consideration of cross-polarisation jamming is the angular error that it induces. As stated, the error is created by an offset that equates to half of the FNBW. This angular error is constant and independent of the range of the platform. This means that as a missile with monopulse homing approaches the target platform, the miss-distance will decrease until the jammer is completely ineffective [8].

2.5.4 Cross-eye jamming

Cross-eye jamming is an EA method that artificially recreates the worst case of glint to distort the wavefront of an angular radar and induce angular errors in it [9]–[12]. This is done by creating two repeater paths, moving in opposite paths, between two spaced-apart antennas. Amplitude and phase control are applied to each so that both have the same amplitude, while there is a phase difference of 180° between them. This is demonstrated in Figure 2.13, where for an ideal cross-eye jammer, $a = 1$ and $\phi = 180°$.

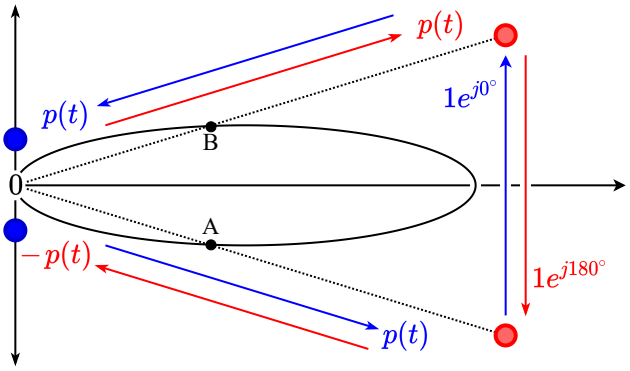

Figure 2.14. An illustration of the transmission of a monopulse radar pulse on the sum-channel, and the resultant effect caused by a cross-eye jammer.

The basic principles of cross-eye jamming can be explained by making the following assumptions. Figure 2.14 shows the transmission of a radar pulse, $p(t)$, in the direction of a cross-eye jammer. The jammer elements are indicated by the red circles, while the blue circles indicate the radar elements. A monopulse radar always transmits on the sum-channel and receives on both the sum- and difference channels [4]. The lobe in Figure 2.14 indicates the sum-channel antenna pattern, which is assumed to be symmetric, so that point A and B are on exact opposite ends of the pattern, where the magnitudes of the pattern are equal. To further simplify this, it is assumed that the magnitude of the pattern at both A and B is unity and that the radar and jammer are exactly on broadside of one another. Finally, it is assumed that each jammer antenna pattern also has unity gain in the direction of the radar.

As the pattern is symmetric with unity gain in the directions of the jammer elements, both the top and bottom jammer antennas will receive an identical version of the transmitted pulse, $p(t)$. The pulse that is received at the bottom antenna is transmitted at the top antenna without undergoing any phase shift. The blue arrows indicate the path that this pulse follows. Similarly, the pulse received at the top jammer antenna is also transmitted at the bottom antenna, with the difference that a 180° phase-shift is now applied to the pulse, transforming it from $p(t)$ to $-p(t)$. The red arrows indicate the path that this pulse follows.

As the points on the sum-channel where the pulses are received have unity gain, the sum-channel return from the top jammer antenna is equal to $p(t)$, while that of the bottom is $-p(t)$. When the two values are superimposed to form the effective sum-channel return, it can be seen that the values cancel and that the effective sum-channel return is 0. By considering that a monopulse ratio is formed by

dividing the difference- by the sum-channel return, it is apparent that the monopulse ratio, in this case, will be infinite if the magnitude of the difference-channel return is more than 0. This will be the case because the cross-eye jammer causes the difference-channel to add, rather than cancel, as opposed to the sum-channel. It should be noted that the cancelling property of the cross-eye jammer causes the jammer to be immune to multipath, as long as the same phase-centres are used for reception and transmission at each end of the jammer.

Lastly, it should be noted that, opposed to cross-polarisation jamming, cross-eye jamming does not induce a fixed angular error on the radar, but rather a fixed linear offset [8], [29]. This is due to cross-eye jamming recreating glint, where the apparent target can be seen as the balancing point [9], [29]. The miss distance from a missile will remain constant, regardless of its range, which means that a cross-eye jammer will remain effective against missile threats [8]. An extensive analysis of retrodirective cross-eye jamming, with fewer assumptions, is given in Chapter 3.

2.5.4.1 Retrodirectivity

A retrodirective reflector is a system that reflects or repeats EM energy back into the direction that it came from [9], [24]. In other words, if a signal is sent towards a retrodirective reflector, the reflected wavefront will be parallel to the incident wavefront, as can be seen in Figure 2.15 [30]. This is important in cross-eye jamming as two spaced antennas are used [9]. If the jammer is not retrodirective, it will only be functional if the effective wavefront of the jammer is perpendicular to broadside of the radar. In other words, an aircraft using a cross-eye jammer with antennas on its wingtips will have to fly directly towards the radar to be effective [9]. However, if the jammer is retrodirective, an aircraft can have any orientation without significant reduction in cross-eye jammer performance [9].

A Van Atta array is a retrodirective array with interconnected paths between each opposing antenna pair, as shown in Figure 2.15 [24], [30], [31]. It should be noted that all of these paths should have the same phase delay, and the antennas on both sides of the centre of the array should be symmetric [31].

For simplicity, consider just the two outer antennas in Figure 2.15, antennas A and D. If a signal is incident from an angle that is not on broadside of the effective array pattern, the wavefront will reach the one antenna first before reaching the other. In Figure 2.15, the incident wavefront will reach antenna D before it reaches A. Therefore, there is a phase delay that can be calculated as $\Delta\Psi_i = 4\psi - \psi = 3\psi$. If the signal at antenna A is repeated at antenna D, and the signal at antenna D is repeated at antenna

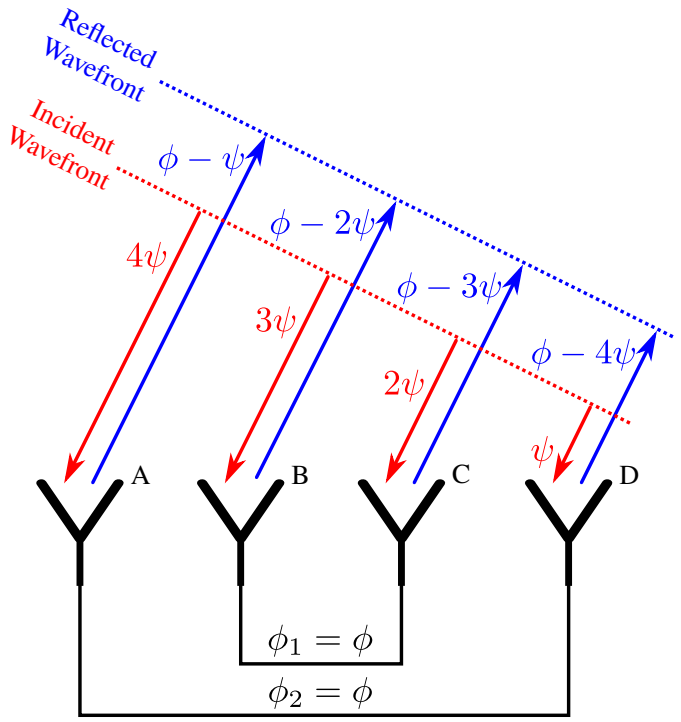

Figure 2.15. A four-element Van Atta array. Adapted from [30], © 2013 IEEE.

A, the phase delay of the signal between antenna A and D on transmission can be shown to be equal to that on reception. This phase delay can be calculated as $\Delta\Psi_r = (\phi - \psi) - (\phi - 4\psi) = 3\psi$, where ϕ is the phase delay through the interconnected path. As the phase difference on transmission equals that on reception, the wavefront of the reflected signal propagates in exactly the opposite direction as the incident wavefront. This proves that antenna A and D forms a retrodirective array when used separate from the larger array [24].

The same phenomenon also occurs when considering only antennas B and C. If the two retrodirective pairs (A–D and B–C) have an equal phase delay through the connecting paths, they form a larger Van Atta array. A Van Atta array can be implemented by using an even number of antenna elements in an antenna array, granted that they are symmetric around the centre of the array and that all the paths have the same phase delay [9], [24], [31].

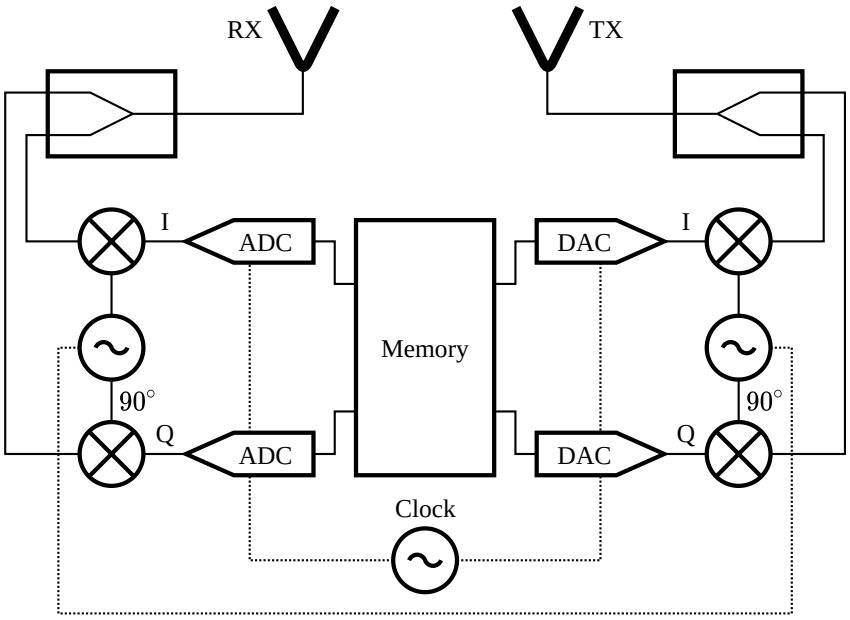

Figure 2.16. An illustration of a DRFM system. All synchronous devices are connected by dotted lines.

2.6 HARDWARE

2.6.1 Digital radio frequency memory

A digital radio-frequency memory (DRFM) device is an RF device that is used to capture, alter and repeat signals coherently. DRFMs are used on EW platforms to create multiple false targets in an attempt to deceive adversary radars. In addition to this, DRFMs are also commonly used to implement RGPO and VGPO, as they are coherent and allow for exact control over the created false targets. DRFMs are also known for their little latency [1].

A DRFM device works by receiving a signal using a superheterodyne receiver. The signal is mixed down to its baseband form. This signal is then converted to a digital format and stored in a memory device, where it is altered as needed [1]. After this, the signal is converted back to analogue, sent to a superheterodyne transmitter, where it is mixed up to its RF form and transmitted [1].

Figure 2.16 is an illustration of a DRFM system that uses quadrature sampling [1]. Note that some RF components were omitted in the diagram. To ensure coherency, all analogue-to-digital converters (ADCs) and digital-to-analogue converters (DACs) in a DRFM device use the same sampling clock, while the same carrier oscillator is used for the mixing of the signals in all RF receivers and trans-

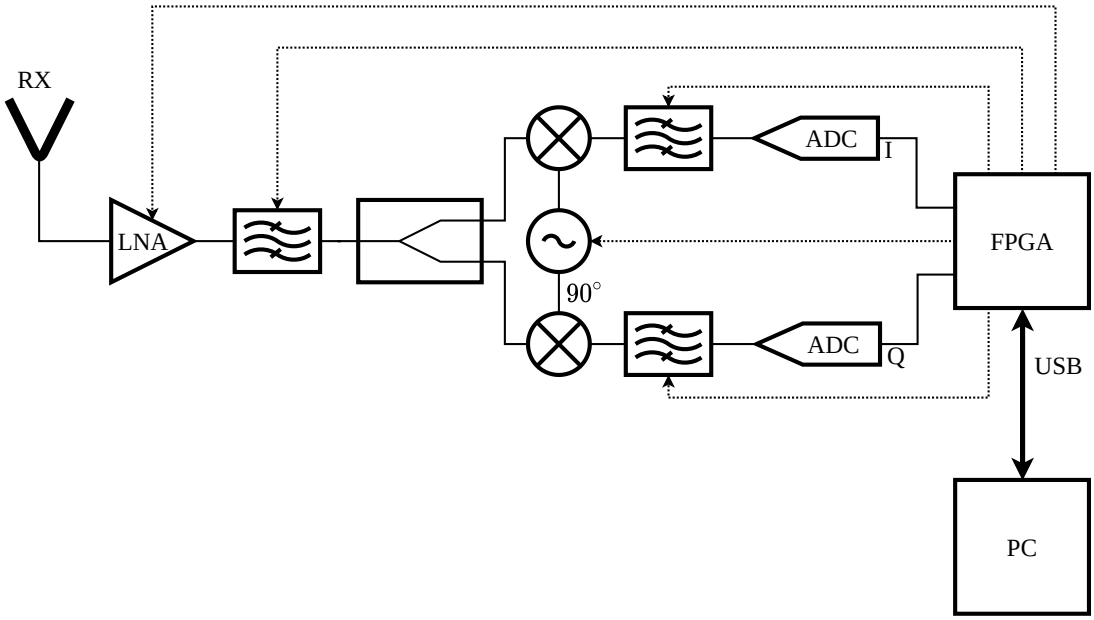

Figure 2.17. An example of an SDR. The dotted lines indicate that the PC controls the parameters of the specific components by using the FPGA.

mitters [1]. DRFM devices can have multiple channels, which can be considered as a collection of single-channel DRFM devices, such as in Figure 2.16, but where all the devices are synchronised to ensure coherency.

2.6.2 Software-defined radio

An SDR is a device with one or more superheterodyne RF receiver and transmitter. The significance of an SDR is that all of the RF hardware parameters, such as oscillator frequency and filter cut-off frequencies, are controlled using a personal computer [1], [32]. The data that is received by an SDR is also converted to a digital form and sent to the computer either via USB or network cable, where the data is manipulated and processed as needed. An SDR can also transmit data. This is done by creating the desired signal digitally on the computer and sending it to the SDR. The data is then converted from a digital to an analogue form before being sent to the transmitter [1]. The path that data follows to and from a computer is the cause of significant latency when using SDRs. This is one of the reasons why SDRs are undesirable for signal repeating purposes. Most SDRs either have microprocessors, digital signal processors (DSPs) or field-programmable gate arrays (FPGAs) embedded in their hardware to control the flow of data on the device and communicate with a computer [1]. Figure 2.17 shows an example of a basic SDR with only reception capabilities. The device uses a computer to control the RF

components through an FPGA. Modern SDRs have multiple receivers and transmitters, with numerous amplifiers and filters in each [32].

2.7 CHAPTER SUMMARY

The reader was introduced to radar, and EW, as the concepts of each forms the foundation that is built on in the development of a retrodirective cross-eye jammer. As part of this introduction, cross-eye jamming was compared to other methods of angular deception, with emphasis on cross-polarisation jamming, as one author considers it most comparable [8]. One significant advantage of cross-eye jamming over cross-polarisation jamming is that the former creates a constant offset in displacement of the apparent target from the actual target, where the latter creates a constant angular error. This suggests that cross-eye jamming may be more successful in the deception of radar-guided missiles.

CHAPTER 3 AN ANALYSIS OF CROSS-EYE JAMMING

3.1 CHAPTER OVERVIEW

Understanding phase-comparison monopulse radar is imperative when investigating cross-eye jamming. It is not only one of the more robust angular radar systems but also the foundation on which most cross-eye jamming analyses are based [9], [13]. In addition to this, a thorough comprehension of cross-eye jamming is needed to implement and test practical cross-eye jammers. In this chapter, the various previous cross-eye jamming analyses are considered and recreated to give the reader a stronger fundamental understanding of this angular radar countermeasure. Aspects of cross-eye jamming, such as linearity and cross-eye gain, are also investigated.

3.2 PHASE-COMPARISON MONOPULSE ANALYSIS

Phase-comparison monopulse radar is often used as the homing system on radar-guided missiles. It is usually more compact than amplitude-comparison monopulse, requiring a parabolic reflector to ensure that there is just one phase centre [4]. Because of its compact size, it is assumed that a cross-eye jammer would have to contend with this type of radar processing when deceiving approaching missiles. Rhodes defined three postulates for an angular radar to be considered as monopulse [28], [33]. These postulates can be summarised as:

1. The monopulse error should be in the form of a ratio.
2. The monopulse error for a positive angle should have the same magnitude and opposite sign as a negative angle of the same magnitude.
3. The monopulse error function should be real, odd and a function of the AoA.

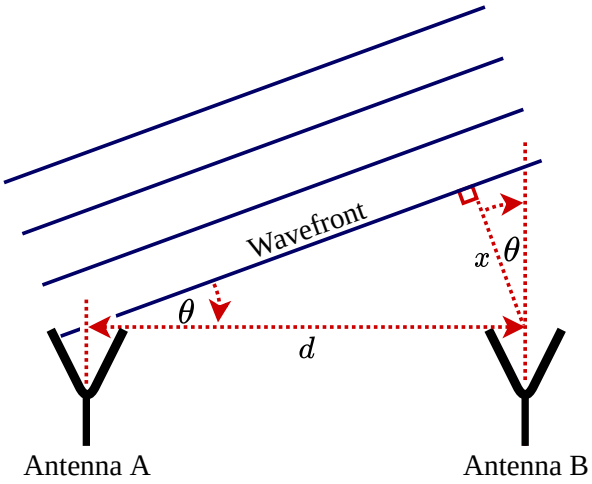

Figure 3.1. An illustration of how an incoming signal's planar wavefront interacts with two antennas with different phase centres.

The first postulate is essential because when a ratio is used to describe the monopulse error, the signal is normalised, leading to the angular information independent of the received radar signal's power. Note that a received signal with a low SNR will still lead to errors due to noise. The second and third postulates are essential, as the exact angular resolution at both sides of the radar's broadside is desired. An odd function is needed to determine from which side of broadside the signal is from.

For a phase-comparison monopulse radar, two or more antenna elements, all with different phase centres, are needed [4]. This is because a phase-comparison monopulse radar uses the difference in phase of a received signal to determine its AoA while still adhering to Rhodes's postulates. To obtain different phase centres, one can either use multiple antenna elements and space them a certain distance apart or use multiple adjacent parabolic reflector antennas [4]. In both cases, the net effect is an array of antenna elements. For simplicity and the avoidance of redundancy, only a monopulse radar working in azimuth will be considered.

Figure 3.1 shows two antennas that are being brushed by the wavefront of an approaching radar signal. It is assumed that target platforms will almost exclusively be in the far field of radars. This assumption simplifies the system and allows us to use basic geometry due to the wavefront's planar nature.

When considering the geometry in Figure 3.1, where the antenna spacing is given as d m, the wavefront will have to move x m further to reach Antenna B, after Antenna A was reached. As stated before, the

velocity that an EM wave propagates at is approximately 2.998×10^8 m/s [25]. This creates a time delay, which can be calculated as

$$T_d = \frac{x}{c}\,, \tag{3.1}$$

with x being the distance shown in Figure 3.1 and c being the propagation velocity of an EM wave in a vacuum. By using elementary trigonometry, it can be shown that $x = d\sin\theta$, where θ is the AoA of the planar wave, measured from broadside of the radar. If the incoming wave's exact frequency is known, the time delay can be used to calculate the phase difference of the wavefront between Antenna A and B. This phase difference is given by

$$\Delta\phi = \beta d\sin(\theta)\,, \tag{3.2}$$

where the propagation constant is given by

$$\beta = \frac{2\pi f}{c}\,, \tag{3.3}$$

and f is the frequency of the received signal.

Using this phase difference in conjunction with Rhodes's postulates, the monopulse error function of a phase-comparison monopulse radar can be derived. Assume that Antenna A and B have the same antenna element pattern $P(\theta)$. This pattern can either be that of a single element or a subarray of elements. If a signal is received at Antenna A, the sensed signal will be the original signal, multiplied by the net antenna pattern of Antenna A, given by $P(\theta)$. The same will happen at Antenna B, but with the addition of the phase difference. Therefore, the sensed signal at Antenna B will be multiplied by the net antenna pattern of Antenna B, which is given by $e^{j\beta d\sin(\theta)}P(\theta)$.

Rhodes's postulates require the monopulse error function to be an odd ratio. For a phase-comparison monopulse radar, this ratio must be created by using the net antenna patterns at Antenna A and Antenna B. It is known that to obtain an odd function after dividing two functions, the one function has to be odd and the other has to be even. If the net antenna patterns as Antenna A and B are summed they form an even function. This is called the sum-channel antenna pattern, which can be calculated as

$$\begin{aligned} S(\theta) &= e^{j\beta d\sin(\theta)}P(\theta) + P(\theta) && (3.4)\\ &= \left[e^{j\beta d\sin(\theta)} + 1\right]P(\theta) && (3.5)\\ &= e^{j\frac{\beta d}{2}\sin(\theta)}\left[e^{j\frac{\beta d}{2}\sin(\theta)} + e^{-j\frac{\beta d}{2}\sin(\theta)}\right]P(\theta) && (3.6)\\ &= 2\cos\left[\frac{\beta d}{2}\sin(\theta)\right]e^{j\frac{\beta d}{2}\sin(\theta)}P(\theta)\,. && (3.7) \end{aligned}$$

Similarly, it can be shown that the difference between the net antenna patterns at Antenna A and B results in an odd function. This is called the difference-channel antenna pattern is calculated as

$$D(\theta) = e^{j\beta d\sin(\theta)}P(\theta) - P(\theta) \tag{3.8}$$

$$= (e^{j\beta d\sin(\theta)} + 1)P(\theta) \tag{3.9}$$

$$= e^{j\frac{\beta d}{2}\sin(\theta)}(e^{j\frac{\beta d}{2}\sin(\theta)} - e^{-j\frac{\beta d}{2}\sin(\theta)})P(\theta) \tag{3.10}$$

$$= 2j\sin\left[\frac{\beta d}{2}\sin(\theta)\right]e^{j\frac{\beta d}{2}\sin(\theta)}P(\theta)\,. \tag{3.11}$$

In both the sum- and difference-channel antenna pattern calculations, there is an extra phase component. This component can be neglected as it will sum with the random phase of the incoming radar signal. The final sum-channel antenna pattern is therefore given by

$$S(\theta) = 2\cos\left[\frac{\beta d}{2}\sin(\theta)\right]P(\theta)\,, \tag{3.12}$$

while the difference-channel antenna pattern is given by

$$D(\theta) = 2j\sin\left[\frac{\beta d}{2}\sin(\theta)\right]P(\theta)\,. \tag{3.13}$$

The derived equations, (3.12) and (3.13) correspond to that in previous analyses [9]. From the two functions, a monopulse error function should be created. This can be done by either dividing the sum- by the difference-channel antenna pattern or vice versa, as both would result in an odd function. It would be problematic to divide the sum- by the difference-channel antenna pattern, as a target near broadside will result in a difference-channel return of almost zero and an immense monopulse error value, making processing impossible. The solution would be to divide the difference- by the-sum-channel pattern. In this case, a target at broadside will result in a monopulse error of zero, while a target has to be at an angle of 180° to create a phase difference that will make the denominator zero. Therefore, the monopulse error function can be calculated as

$$M(\theta) = j\tan\left[\frac{\beta d}{2}\sin(\theta)\right]\,. \tag{3.14}$$

To adhere to Rhodes's third postulate, which does not only need the monopulse function to be even but real as well, the imaginary part has to be taken, resulting in

$$M(\theta) = \tan\left[\frac{\beta d}{2}\sin(\theta)\right]\,. \tag{3.15}$$

As stated before, it can be seen that the monopulse ratio is not dependant on the element antenna patterns, assuming that the patterns are identical and not distorted differently by the mounting platform [9].

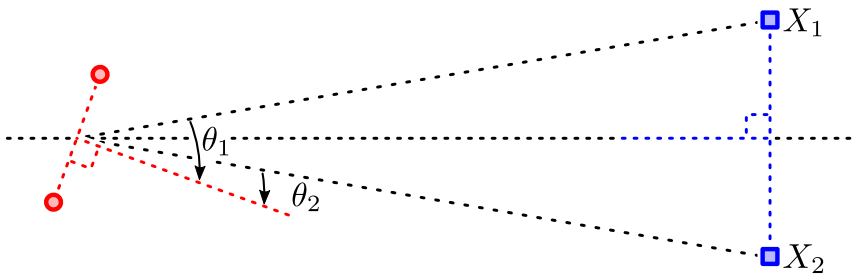

Figure 3.2. Geometry of the interaction between a general monopulse radar and two point-scatterers. The two point-scatterers (X_1 and X_2) are indicated by the blue squares, while the radar elements are given by red circles. Adapted from [20], © 2015 IEEE.

3.3 LINEAR-FIT ANALYSIS

The linear-fit analysis considers a cross-eye jammer as a platform with only two scatterers spaced a certain distance apart. These scatterers are assumed to have a constant phase difference and amplitude scaling factor between them. The analysis is done by considering the effect of the scatterers on a monopulse radar as a glint error, which can be expressed as a linear function [11], [12], [29], [34]. Furthermore, the antennas were approximated by using linear fits to them [34]. Other variations of this analysis used linear fits to express the sum- and difference channel antenna pattern.

The monopulse ratio of an exact monopulse processor can be described as

$$M = k\theta_i \,, \tag{3.16}$$

where k is a system-specific constant and θ_i is the angle of the target as measured from broadside of the radar [4], [33]. By considering that the monopulse ratio is formed by dividing the difference- by the sum-channel return, the monopulse ratio in (3.16) can be expanded as

$$\frac{d}{s} = k\theta_i \,, \tag{3.17}$$

where the sum- and difference-channel return are given by s and d, respectively. The equation in (3.17) can be written in terms of the difference-channel return as

$$d = k\theta_i s \,. \tag{3.18}$$

If a target platform has two point-scatterers, as shown in Figure 3.2, the effective sum- and difference-channel returns have to be calculated by superimposing the effect of each scatterer [11], [34]. The

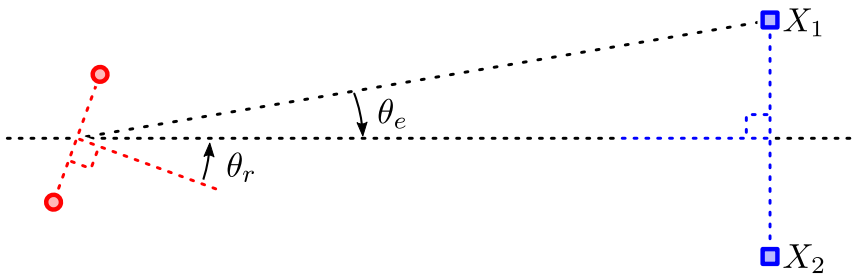

Figure 3.3. Geometry of the interaction between a general monopulse radar and two point-scatterers. The two point-scatterers (X_1 and X_2) are indicated by the blue squares, while the radar elements are given by red circles. Adapted from [20], © 2015 IEEE.

scatterers in Figure 3.2, given by X_1 and X_2, can be expressed in terms of their amplitudes and phases as $a_1 e^{j\phi_1}$ and $a_2 e^{j\phi_2}$. The effective sum-channel return can be calculated by summing the two components to yield

$$s_e = a_1 e^{j\phi_1} + a_2 e^{j\phi_2} \,, \tag{3.19}$$

where a_1 and a_2 are the amplitudes of scatterer 1 and 2, respectively, while ϕ_1 and ϕ_2 are the phases of each [11]. The effective difference-channel return can be expressed as

$$d_e = k\theta_1 a_1 e^{j\phi_1} + k\theta_2 a_2 e^{j\phi_2} \,, \tag{3.20}$$

where θ_1 and θ_2 are the angles of the scatterers as measured from broadside of the radar. The effective monopulse ratio can be obtained by dividing (3.20) by (3.19), giving

$$M_e = \frac{k\theta_1 a_1 e^{j\phi_1} + k\theta_2 a_2 e^{j\phi_2}}{a_1 e^{j\phi_1} + a_2 e^{j\phi_2}} \,. \tag{3.21}$$

The effective monopulse ratio in (3.21) can be used to express the effective indicated angle as

$$\theta_i = \Re\left\{ \frac{\theta_1 a_1 e^{j\phi_1} + \theta_2 a_2 e^{j\phi_2}}{a_1 e^{j\phi_1} + a_2 e^{j\phi_2}} \right\} \,. \tag{3.22}$$

For simplicity, θ_1 and θ_2 can be written in terms of the rotation of the radar, given by θ_r, and half the angular separation of the distance between the scatterers, given by θ_e. The definitions of θ_r and θ_e can also be seen in Figure 3.3, which is an adapted version of Figure 3.2. The angles can now be written as

$$\theta_1 = \theta_r + \theta_e \,, \tag{3.23}$$

and

$$\theta_2 = \theta_r - \theta_e \,. \tag{3.24}$$

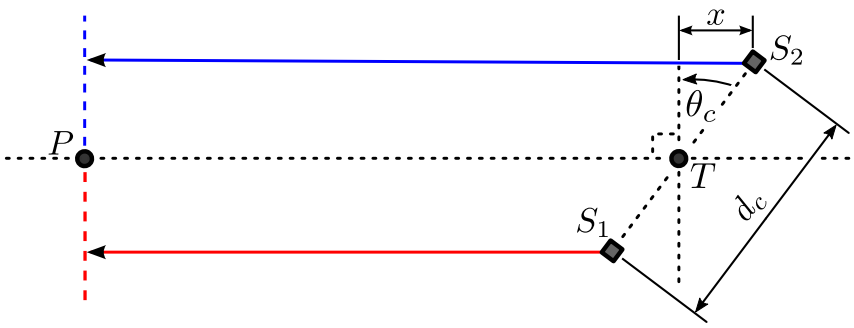

Figure 3.4. An illustration of two spaced-apart sources as observed from a point, P, that is very far from the sources.

By using the first scatterer, X_1, as a zero-reference, the amplitude and phase become $a_1 = 1$ and $\phi_1 = 0°$, respectively. Relative to this reference point, the amplitude and phase of X_2 can now be expressed as $a_2 = a$ and $\phi_2 = \phi$. By substituting these new values, in conjunction with (3.23) and (3.24) into (3.22), the indicated angle can be written as

$$\theta_i = \Re\left\{\frac{\theta_r + \theta_e + ae^{j\phi}(\theta_r - \theta_e)}{1 + ae^{j\phi}}\right\}, \tag{3.25}$$

which can be simplified to

$$\theta_i = \Re\left\{\theta_r + \theta_e\left(\frac{1 - a^{j\phi}}{1 + a^{j\phi}}\right)\right\}. \tag{3.26}$$

Finally, by considering only the real part of the equation, the indicated angle is given as

$$\theta_i = \theta_r + \theta_e\left[\frac{1 - a^2}{1 + a^2 + 2a\cos(\phi)}\right]. \tag{3.27}$$

3.4 PHASE-FRONT ANALYSIS

The phase-front analysis is done by considering the wavefronts of two spaced-apart sources that are transmitting the same signal at a point very far away from the sources [10]. The analysis shows that by adding an amplitude scale and phase offset, the wavefront at the observation point becomes distorted [10], [11], [35].

This can be seen in Figure 3.4, where the two sources are indicated by S_1 and S_2, respectively, and P is the observation point. The distance from the observation point and the point in the centre of the sources (indicated by T) is much larger than the spacing of the two sources (denoted by d_c).

Firstly, it can be seen that the signal that is transmitted at S_1 has to propagate $2x$ m less than the signal at S_2. Relative to the centre point, T, the signal at S_1 has to propagate x m less, where the signal at S_2 has to propagate x meters more [10]. By considering the geometry in Figure 3.4, the value of x can be expressed as

$$x = \frac{d_c}{2}\sin(\theta_c) \ . \tag{3.28}$$

Consider a case where there is an added phase offset, given by ϕ, and an amplitude scaling factor, given by a, between the sources. The angle of the wavefront at the observation point can be expressed by considering the effective horizontal and vertical components that were caused by the sources, and calculating the tangent thereof [10]. This can be done as

$$\delta(\theta_c) = \frac{A\sin[\phi + \frac{\beta dc}{2}\sin(\theta_c)] + aA\sin[-\frac{\beta dc}{2}\sin(\theta_c)]}{A\cos[\phi + \frac{\beta dc}{2}\sin(\theta_c)] + aA\cos[-\frac{\beta dc}{2}\sin(\theta_c)]} \ , \tag{3.29}$$

where A is the amplitude of the signal that was transmitted by the second source, and β is the propagation constant. The slope of this resulting wavefront, relative to the wavefront that a single source at T would have produced, can be calculated by differentiating (3.29) in terms of the angle [10]. This yields

$$\delta'(\theta_c) = \left[\frac{\beta d_c \cos(\theta_c)}{2}\right]\left[\frac{1-a^2}{1+a^2+2a\cos[\phi+\beta d_c\sin(\theta_c)]}\right] \ , \tag{3.30}$$

which can be reduced by considering a case of no rotation ($\theta_c = 0$) so that

$$\delta'(0) = \left[\frac{d_c}{2}\right]\left[\frac{1-a^2}{1+a^2+2a\cos(\phi)}\right] \ . \tag{3.31}$$

As the observation point, P, is far away from the sources, it is assumed that the incident wavefront is planar. This means that the angle of the wavefront should remain constant. Equivalently, the value of $\delta'(0)$ should be zero, and any deviation from this is regarded as an error [10], [35]. To extend this analysis to radar, two spaced-apart repeating devices installed on a platform under protection can be considered two sources. If the repeaters have a phase difference of ϕ and a relative amplitude scale of a, the wavefront of the radar signal will be distorted. If the radar uses phase information to do angular processing, errors will be experienced.

The biggest limitation of the phase-front analysis is the approximation that the radar is infinitely far from the jammer, meaning that both radar elements are at the same point in space. In reality, the radar is a finite distance from the jammer, with two spaced-apart antennas that each receives the signals from both sources [9]. The signals from the two sources (or repeaters) add at that one point, where the phase distortion occurs [10].

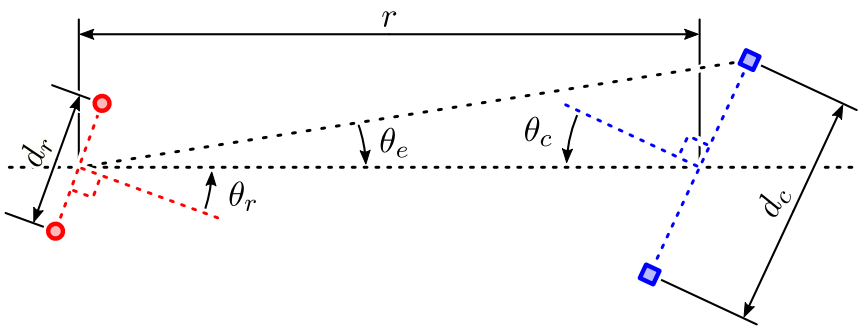

Figure 3.5. Geometry of the interaction between a phase-comparison monopulse radar and cross-eye jammer. Adapted from [20], © 2015 IEEE.

Although there is a difference in the initial approach, the phase-front analysis can be seen as equivalent to the linear-fit analysis, as it is suggested in the literature that all glint analyses are inherently the same [9]–[11], [36]–[38]. It should be noted that neither analyses consider retrodirectivity. In a non-retrodirective repeater-based jammer, the performance of the jammer will reduce significantly if its orientation relative to the radar is changed [9].

3.5 EXTENDED ANALYSIS

The extended analysis improves on all previous analyses by considering the radar's non-linear sum- and difference channel antenna patterns, with the radar being a finite distance from the jammer. The effect of the new radar return from both jammer elements is considered on both the sum- and difference-channel patterns [9], [13].

It should be duly noted that the analysis in this section is a recreation of the original extended analysis and was done by using the extended analysis as a close guideline [9].

Figure 3.5 shows the geometry of the interaction between a phase-comparison monopulse radar and retrodirective cross-eye jammer [9]. In this figure, the phase centres of the radar are indicated with circles while the jammer antennas are indicated with squares. The rotation of the radar is denoted by θ_r, while its antenna spacing is indicated by d_r. At the jammer, d_c indicates the antenna separation, while θ_c indicates the rotation of the jammer. The jammer is located at a distance of r meters from the radar and θ_e indicates half the angular separation of the jammer elements from the centre of the radar [9].

The analysis can be started by considering the jammer antennas as individual point scatterers and obtaining the sum- and difference-channel equations in the direction of each scatterer. This can be done by adjusting (3.12) and (3.13) for targets at specific angles. Figure 3.5 shows that the angle between broadside of the radar and the top jammer element is given by $\theta_r + \theta_e$, where the angle between broadside of the radar and the bottom jammer element is given by $\theta_r - \theta_e$. By using these angles, the sum- and difference-channel antenna pattern equations for the top element can be expressed as

$$S_t(\theta) = \cos\left[\frac{\beta d}{2}\sin(\theta_r + \theta_e)\right] P_r(\theta_r + \theta_e)\,, \tag{3.32}$$

and

$$D_t(\theta) = j\sin\left[\frac{\beta d}{2}\sin(\theta_r + \theta_e)\right] P_r(\theta_r + \theta_e)\,, \tag{3.33}$$

respectively. In (3.32) and (3.33), the element antenna patterns are assumed to be equal. The element antenna pattern is given by P_r.

Similarly, the sum- and difference-channel antenna pattern equations for the bottom element can be expressed as

$$S_b(\theta) = \cos\left[\frac{\beta d}{2}\sin(\theta_r - \theta_e)\right] P_r(\theta_r - \theta_e)\,, \tag{3.34}$$

and

$$D_b(\theta) = j\sin\left[\frac{\beta d}{2}\sin(\theta_r - \theta_e)\right] P_r(\theta_r - \theta_e)\,. \tag{3.35}$$

Before continuing the extended analysis, consider Figure 3.5 again. A practical cross-eye jammer would have to operate at a distance that is much larger than the span between the jammer elements so that $r >> d_c$ [22]. This distance, r, can be orders of magnitude larger than the span of the jammer elements. By considering these parameters, the value of θ_e may seem negligibly small. However, if the assumption is made that $\theta_e = 0°$, there is no longer a distinction between the top and bottom jammer elements, and the jammer will turn into a beacon. Therefore, it should be emphasised that the angle, θ_e, is critical in analysing a cross-eye jammer.

To continue the analysis, all sum- and difference-channel antenna patterns should be expanded mathematically. This can be done by considering the terms inside the sum- and difference-channel equations separately and using the identity (A.1), given in Addendum A. The term inside the patterns for the top

element can be expanded as

$$\frac{\beta d_r}{2}\sin(\theta_r+\theta_e) = \frac{\beta d}{2}\left[\sin(\theta_r)\cos(\theta_e)+\cos(\theta_r)\sin(\theta_e)\right] \tag{3.36}$$

$$= k + k_c \,, \tag{3.37}$$

while that of the bottom element can be expanded as

$$\frac{\beta d_r}{2}\sin(\theta_r-\theta_e) = \frac{\beta d}{2}\left[\sin(\theta_r)\cos(\theta_e)-\cos(\theta_r)\sin(\theta_e)\right] \tag{3.38}$$

$$= k - k_c \,. \tag{3.39}$$

In these expansions,

$$k = \frac{\beta d_r}{2}\sin(\theta_r)\cos(\theta_e) \,, \tag{3.40}$$

and

$$k_c = \frac{\beta d_r}{2}\cos(\theta_r)\sin(\theta_e) \,. \tag{3.41}$$

The sum- and difference-channel antenna equations for the top element can now be simplified by substituting (3.37) into (3.32) and (3.33). This is done as

$$S_t(\theta) = \cos(k+k_c)P_r(\theta_r+\theta_e), \tag{3.42}$$

for the sum-channel pattern, and

$$D_t(\theta) = j\sin(k+k_c)P_r(\theta_r+\theta_e) \,, \tag{3.43}$$

for the difference-channel pattern. The same can be done for the patterns of the bottom element by substituting (3.39) into (3.34) and (3.35). The resulting sum- and difference-channel equations for this element are given by

$$S_b(\theta) = \cos(k-k_c)P_r(\theta_r-\theta_e) \,, \tag{3.44}$$

and

$$D_b(\theta) = j\sin(k-k_c)P_r(\theta_r-\theta_e) \,, \tag{3.45}$$

respectively.

For the ease of calculation, the product of the radar's antenna element patterns in the direction of the top and bottom jammer element can be expressed as

$$P_1(\theta_r,\theta_e) = P_r(\theta_r+\theta_e)P_r(\theta_r-\theta_e) \,. \tag{3.46}$$

Similarly, the products of the element patterns of the jammer, from both the top and bottom element in the direction of the radar, can be expressed as

$$P_2(\theta_c, \theta_e) = P_c(\theta_r + \theta_e)P_c(\theta_r - \theta_e)\ . \tag{3.47}$$

To model the effect of the cross-eye jammer on the monopulse ratio of the radar, the effective sum- and difference-channel patterns of the radar in the presence of the jammer should be obtained, where the effects of each element pattern and the internal jammer paths on the radar signal should be considered. It should be noted that monopulse radars always transmit on the sum-channel and receive on both the sum- and difference-channels. It should also be noted that this analysis is for a retrodirective cross-eye jammer, meaning that there are two internal jammer paths in a Van Atta configuration. To obtain the effective sum-channel pattern caused by the jammer, the sum-channel patterns of the radar for both paths should be obtained separately and summed together. For this system, it is chosen that the phase difference (ϕ) and amplitude scaling factor (a) is applied when the jammer receives at the bottom element and transmits at the top element. The effective sum-channel can be calculated and simplified as

$$\begin{aligned} S_j &= S_t P_c(\theta_c + \theta_e)P_c(\theta_c - \theta_e)S_b + ae^{j\phi} S_b P_c(\theta_c + \theta_e)P_c(\theta_c - \theta_e)S_t && (3.48)\\ &= P_2(\theta_c, \theta_e)S_t S_b \left(1 + ae^{j\phi}\right) && (3.49)\\ &= P_2(\theta_c, \theta_e)\cos(k + k_c)P(\theta_r + \theta_e)2\cos(k - k_c)P(\theta_r - \theta_e)\left(1 + ae^{j\phi}\right) && (3.50)\\ &= P_1(\theta_r, \theta_e)P_2(\theta_c, \theta_e)\cos(k + k_c)\cos(k - k_c)\left(1 + ae^{j\phi}\right)\ . && (3.51) \end{aligned}$$

In (3.51), the radar transmits a signal on the sum-channel. Part of this signal propagates in the direction of the top jammer element and is subjected to the radar's element pattern in the direction of this element. This signal is received at the jammer's top element and is subjected to the antenna pattern of the top element in the direction of the radar.

The signal is then repeated at the bottom element, where it is subjected to the pattern of the bottom element in the direction of the radar. Finally, the signal is received on the sum-channel of the radar and is subjected to the element pattern of the radar in the direction to the bottom jammer element. While this happened, the same process happened in the opposite path. The signal also propagates in the direction of the bottom element, received there and transmitted at the top element. This happens with the addition that the signal is scaled in amplitude and phase-shifted before being repeated. The

signal repeated at the top jammer element is then also received on the sum-channel of the radar while being subjected to the radar's element pattern in the direction of the top radar element.

The sum-channel pattern in (3.51) can be further simplified by using (A.10), and is shown in Addendum A. This yields a final effective sum-channel antenna pattern of

$$S_j = \frac{P_1(\theta_r,\theta_e)P_2(\theta_c,\theta_e)}{2}\left[\cos(2k)+\cos(2k_c)\right]\left(1+ae^{j\phi}\right) . \tag{3.52}$$

The effective difference-channel antenna pattern in the presence of the same cross-eye jammer can be simplified by following the same process as for the sum-channel, but by now receiving on the difference-channel of the radar. This is done as

$$\begin{aligned} D_j &= S_t P_c(\theta_c+\theta_e)P_c(\theta_c-\theta_e)D_b + ae^{j\phi}S_b P_c(\theta_c+\theta_e)P_c(\theta_c-\theta_e)D_t && (3.53)\\ &= P_2(\theta_c,\theta_e)(S_t D_b + ae^{j\phi}S_b D_t) && (3.54)\\ &= P_2(\theta_c,\theta_e)\big[\cos(k+k_c)P_r(\theta_r+\theta_e))\,j\sin(k-k_c)P_r(\theta_r-\theta_e)\\ &\quad + ae^{j\phi}\cos(k-k_c)P_r(\theta_r-\theta_e)\,j\sin(k+k_c)P_r(\theta_r+\theta_e)\big] && (3.55)\\ &= jP_1(\theta_r,\theta_e)P_2(\theta_c,\theta_e)\left[\cos(k+k_c)\sin(k-k_c)+ae^{j\phi}\cos(k-k_c)\sin(k+k_c)\right] . && (3.56) \end{aligned}$$

By substituting the results of the derivations, given in (A.15) and (A.20), into (3.56), the final effective difference-channel antenna pattern, in the presence of a cross-eye jammer, can be calculated as

$$\begin{aligned} D_j &= jP_1(\theta_r,\theta_e)P_2(\theta_c,\theta_e)\left\{\frac{1}{2}\left[\sin(2k)-\sin(2k_c)\right]\right.\\ &\quad \left. + ae^{j\phi}\frac{1}{2}\left[\sin(2k)+\sin(2k_c)\right]\right\} && (3.57)\\ &= j\frac{P_1(\theta_r,\theta_e)P_2(\theta_c,\theta_e)}{2}\left\{\left(1+ae^{j\phi}\right)\sin(2k)-\left(1-ae^{j\phi}\right)\sin(2k_c)\right\} . && (3.58) \end{aligned}$$

The last part of the analysis is to calculate the monopulse ratio of the radar in the presence of a jammer. This is done by dividing the effective difference-channel by the effective sum-channel pattern, and

only considering the imaginary part of the result. This is done as

$$M_j = \Im\left\{\frac{D_j}{S_j}\right\} \tag{3.59}$$

$$= \Im\left\{j\frac{\left[\left(1+ae^{j\phi}\right)\sin(2k)-\left(1-ae^{j\phi}\right)\sin(2k_c)\right]}{\left[\cos(2k)+\cos(2k_c)\right]\left(1+ae^{j\phi}\right)}\right\} \tag{3.60}$$

$$= \Im\left\{j\frac{\left(1+ae^{j\phi}\right)\sin(2k)}{\left[\cos(2k)+\cos(2k_c)\right]\left(1+ae^{j\phi}\right)} - j\frac{\left(1-ae^{j\phi}\right)\sin(2k_c)}{\left[\cos(2k)+\cos(2k_c)\right]\left(1+ae^{j\phi}\right)}\right\} \tag{3.61}$$

$$= \frac{\sin(2k)}{\cos(2k)+\cos(2k_c)} - \Im\left\{j\frac{\sin(2k_c)\left(1-ae^{j\phi}\right)}{\left[\cos(2k)+\cos(2k_c)\right]\left(1+ae^{j\phi}\right)}\right\}. \tag{3.62}$$

The division of the terms containing the amplitude scale and phase difference can be simplified as

$$\frac{1-ae^{j\phi}}{1+ae^{j\phi}} = \frac{\left(1-ae^{j\phi}\right)\left(1+ae^{-j\phi}\right)}{\left(1+ae^{j\phi}\right)\left(1+ae^{-j\phi}\right)} \tag{3.63}$$

$$= \frac{1-ae^{j\phi}+ae^{-j\phi}-a^2}{1+ae^{j\phi}+ae^{-j\phi}+a^2}. \tag{3.64}$$

By using Euler's identity, given by (A.4) in Addendum A, this can be simplified even further as

$$\frac{1-ae^{j(\phi)}}{1+ae^{j(\phi)}} = \frac{1-a\cos(\phi)-aj\sin(\phi)+a\cos(\phi)-aj\sin(\phi)-a^2}{1+a\cos(\phi)+aj\sin(\phi)+a\cos(\phi)-aj\sin(\phi)+a^2} \tag{3.65}$$

$$= \frac{1-2aj\sin(\phi)-a^2}{1+2a\cos(\phi)+2aj\sin(\phi)+a^2}. \tag{3.66}$$

By substituting (3.66) back into (3.62), the final monopulse ratio for a radar in the presence of a retrodirective cross-eye jammer can be expressed as

$$M_j = \frac{\sin(2k)}{\cos(2k)+\cos(2k_c)} - \Im\left\{j\frac{\sin(2k_c)\left[1-2aj\sin(\phi)-a^2\right]}{\left[\cos(2k)+\cos(2k_c)\right]\left[1+2a\cos(\phi)+2aj\sin(\phi)+a^2\right]}\right\} \tag{3.67}$$

$$= \frac{1}{\cos(2k)+\cos(2k_c)}\left\{\sin(2k)-\sin(2k_c)\frac{1-a^2}{\left[1+a^2+2a\cos(\phi)\right]}\right\} \tag{3.68}$$

$$= \frac{1}{\cos(2k)+\cos(2k_c)}\left[\sin(2k)-\sin(2k_c)G_c\right], \tag{3.69}$$

where

$$G_c(a,\phi) = \frac{1-a^2}{1+a^2+2a\cos(\phi)}. \tag{3.70}$$

3.6 CROSS-EYE GAIN

The cross-eye gain, given by (3.70), is a metric that is used to quantify the amount of deception that is induced by a cross-eye jammer on a monopulse radar [9], [11]–[13]. By considering the monopulse

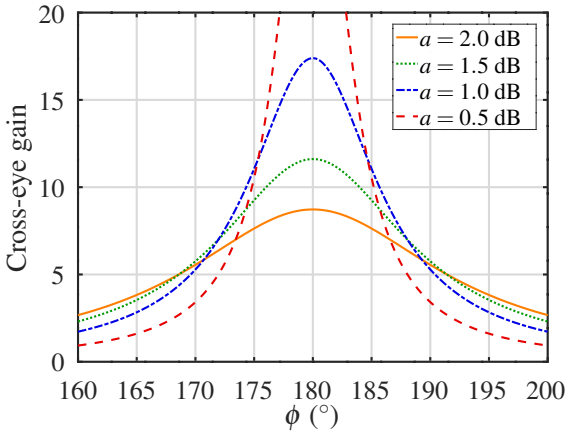

Figure 3.6. Cross-eye gain values for different jammer parameters.

ratio in (3.69), it is apparent that a considerable value of G_c will result in a monopulse ratio, M_j, that is substantial in magnitude. This will result in the radar incorrectly sensing the target platform at an angle with a large offset from the true angle of the target platform. Therefore, it is desired to maximise the value of the cross-eye gain for the best jammer performance.

By inspection, it can be seen that the denominator of (3.70) can be made zero by using $a = 1$ and $\phi = 180^\circ$, and this suggests that these parameters might result in large values of cross-eye gain. However, these parameters also make the numerator zero. To evaluate (3.70) for the parameters above, L'Hôspital's well-known rule can be used. In this function, the rule is applied for the case of $0/0$. Firstly, the chosen value of ϕ can be substituted into (3.70), yielding

$$G_c(a, 180^\circ) = \frac{1-a^2}{1+a^2-2a} \,. \tag{3.71}$$

The function given by (3.71) can now be evaluated for $a = 1$ as

$$G_c(1, 180^\circ) = \lim_{x \to 1} \left[\frac{\frac{d}{dx}(1-x^2)}{\frac{d}{dx}(1+x^2-2x)} \right] \tag{3.72}$$

$$= \lim_{x \to 1} \frac{-2x}{2x-2} \tag{3.73}$$

$$= \infty \,. \tag{3.74}$$

This result suggests that a substantial monopulse ratio can be obtained if the two paths of the jammer are near-equal in amplitude ($a \approx 1$) and almost exactly out of phase ($\phi \approx 180^\circ$). Figure 3.6 shows the cross-eye gain as a function of ϕ for multiple values of a. Note that the values of a are in logarithmic form to ease the interpretation of the figure.

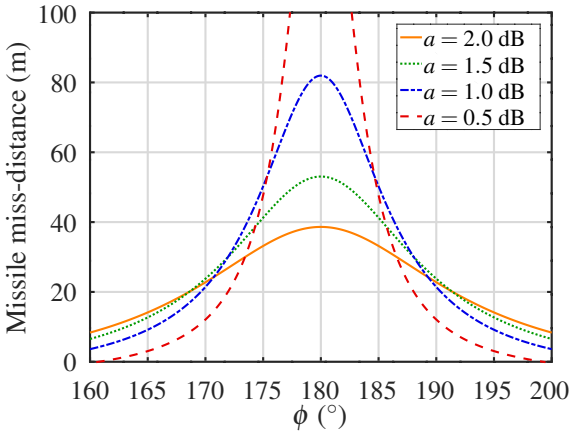

Figure 3.7. Missile miss-distances for different jammer parameters.

In Figure 3.6 it can be seen that by using a cross-eye jammer with $a = 2$ dB, a cross-eye gain of 5 is obtainable if the phase difference between the paths is within 10° of the ideal 180°. However, for this value of amplitude, the maximum cross-eye gain is less than 10. Similarly, a jammer with $a = 0.5$ dB has a maximum cross-eye gain of more than 20, but a cross-eye gain that is much less than 5 if the phase is 10° or more from the ideal. This emphasises that very good amplitude matching between the jammer paths must be accompanied by very accurate phase control to realise a cross-eye jammer with ideal performance. This is true regardless of whether the phase-front or extended analysis is considered.

It is stated in [22] that the distance of an apparent target from the centre of the jammer can be expressed as a function of the cross-eye gain and jammer orientation if the distance between the radar and jammer is sufficient. This relationship is given by

$$|d_o| = G_c \frac{d_c}{2} \cos(\theta_c) \,, \tag{3.75}$$

where the variables, d_c and θ_c, are shown in Figure 3.5.

Without context, the cross-eye gain values in Figure 3.6 are meaningless. Therefore, by using (3.75), assuming no jammer rotation ($\theta_c = 0°$) and subtracting $d_c/2$, the cross-eye gain functions in Figure 3.6 were translated into functions of the missile miss-distance for a cross-eye jammer with an element separation (d_c) of 10 m. The result can be seen in Figure 3.7. Note that the subtraction of $d_c/2$ was done to shift the reference point from the centre of the platform to one of the jammer elements.

In Figure 3.6, it can be seen that by using a cross-eye jammer with $a \leq 1$ dB and a phase difference between jammer paths that are within 5° of the ideal, a cross-eye gain of at least ten can be achieved. By using the same jammer parameters when considering Figure 3.7, this cross-eye gain translates to a minimum missile miss-distance of 45 m.

3.7 LINEARITY

When considering the phase-front analysis, it is suggested that the error that is induced by a cross-eye jammer is in the form of a constant angular offset. This is because the phase-front analysis considers the induced angular error as a linear glint error, which disregards certain aspects of the radar, such as the monopulse patterns [9]–[12]. From (3.27), it can be seen that this angular error is given by $\theta_e G_c$. By considering the monopulse ratio of a phase-comparison monopulse radar (given by (3.15) it can be deduced that the angular error does not change the form of the monopulse ratio function but rather shifts the monopulse function to create a null at a non-zero radar rotation. In contrast to this, the extended analysis suggests that a non-linear error is induced on the monopulse ratio of the radar, as can be seen in (3.69). This error is not constant and varies non-linearly as a function of radar rotation. The reason for the non-linearity is that the analysis considers the monopulse antenna patterns and the effect of the sum-channel beamwidth, which is dependent on the spacing of the radar phase centres and the frequency of the radar [9]. It was shown in [22] that the indicated angle for the case of the extended analysis converges to that of the phase-front analysis if the sum-channel beamwidth is much larger than the angular error. However, practical monopulse radars use very narrow sum-channel lobes, resulting in non-linear behaviour when in the presence of a cross-eye jammer [1], [4].

3.8 CROSS-EYE JAMMING SIMULATIONS

The effect of cross-eye jamming on the sum- and difference-channel antenna patterns of a monopulse radar and the effect on the indicated angle of the radar were investigated using simulation. Note that the indicated angle refers to the angle at which the radar perceives the target to be, regardless of its actual angular position [9]. Where the simulations in [9] used parameters for a theoretical implementation on a real-world platform in the field, the parameters used for the simulations in this section were chosen based on what is reasonable for a test setup in a laboratory, where space is limited. The parameters are summarised below.

1. Radar antenna separation of 0.15 m ($d_r = 0.15$ m).
2. Jammer antenna separation of 0.30 m ($d_c = 0.30$ m).

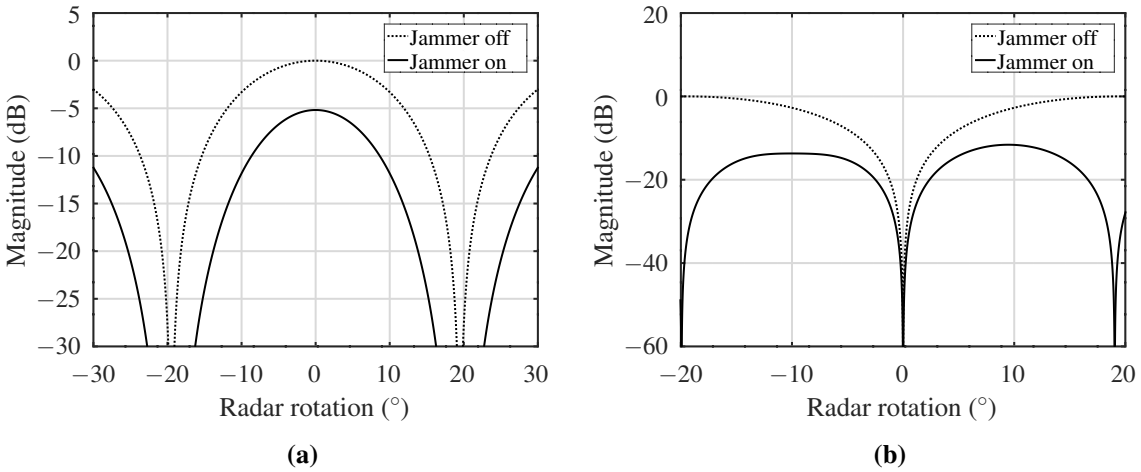

Figure 3.8. A simulation of (a) the sum-channel antenna pattern and (b) the difference-channel antenna pattern for $a = 2.0$ dB and $\phi = 175°$.

3. Distance between radar and jammer of 10 m ($r = 10$ m).
4. Jammer rotation of 0° ($\theta_c = 0°$).
5. Wavelength of 0.1 m ($\lambda = 0.1$ m).

3.8.1 Effect on monopulse antenna patterns

In these simulations, the effects of a cross-eye jammer on the monopulse patterns were considered by using the derived effective pattern equations, given by (3.58) and (3.52), from the extended analysis. The extended analysis was the only analysis where the monopulse patterns were considered. Figure 3.8 shows the sum- and difference channel patterns for the case when a monopulse radar is in the presence of a jammer with the parameters $a = 2$ dB and $\phi = 175°$. As expected, even though the amplitude scaling factor and phase difference are both large, it can be seen that the sum-channel return is cancelled significantly, with the magnitude being 5 dB lower than the theoretical value for when the jammer is inactive. It can be seen that the difference-channel pattern is also attenuated significantly. In addition to the attenuation, it can also be seen that the difference-channel lobes no longer appear symmetric around the null. Figure 3.9 shows the monopulse patterns for the case where a jammer with the parameters, $a = 1$ dB and $\phi = 180°$, were used. It can be seen that both the sum- and difference-channel antenna patterns are attenuated even more, and the distortion of the difference-channel pattern is more evident.

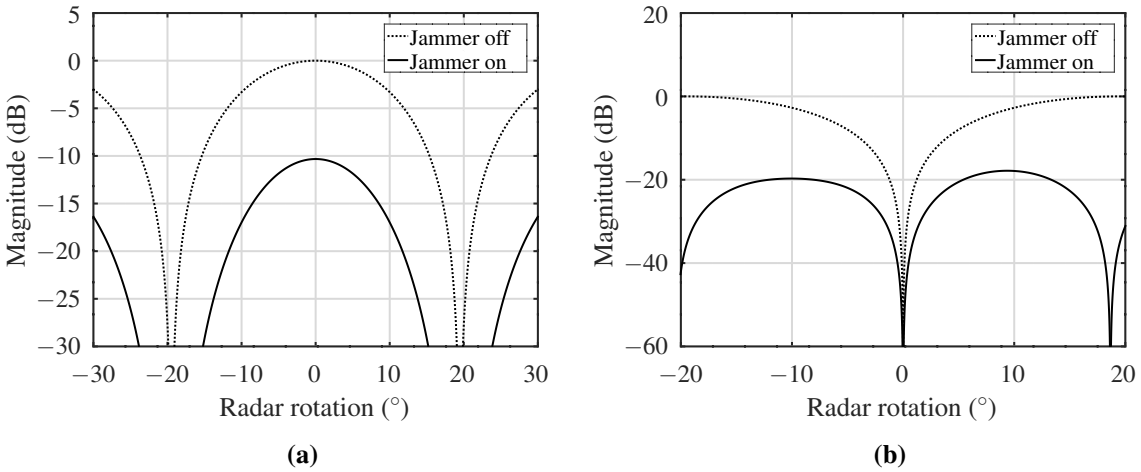

Figure 3.9. A simulation of (a) the sum-channel antenna pattern and (b) the difference-channel antenna pattern for $a = 1.0$ dB and $\phi = 175°$.

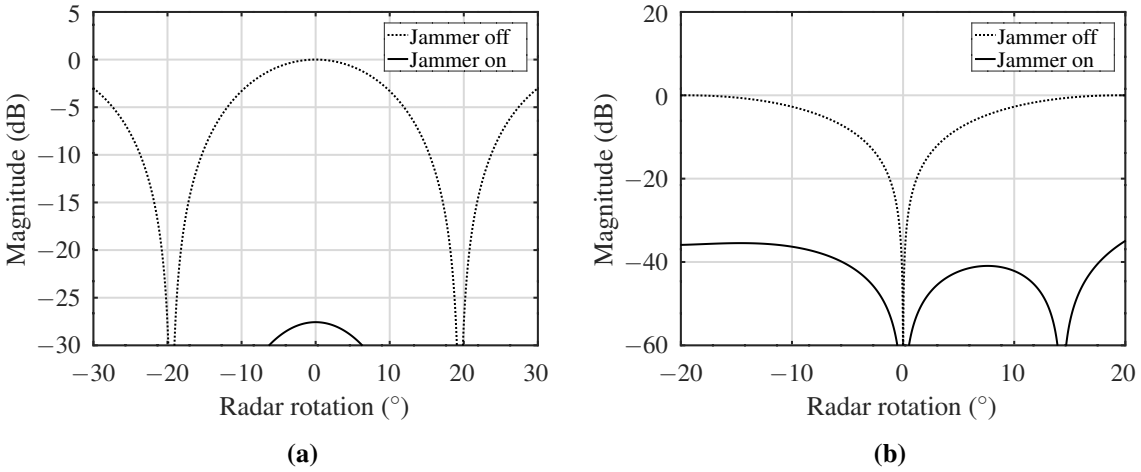

Figure 3.10. A simulation of (a) the sum-channel antenna pattern and (b) the difference-channel antenna pattern for $a = 0.1$ dB and $\phi = 179°$.

To simulate a case where the cross-eye jamming performance is closer to the ideal, the parameters were changed to $a = 0.1$ dB and $\phi = 180°$, and the results can be seen in Figure 3.10. It is clear that the sum-channel magnitude is so low that it would be non-existent in a practical system with noise. The difference-channel is entirely distorted. To the left of the null is a broad lobe, where to the right there is a very narrow lobe, with a third lobe starting to form at around 13°.

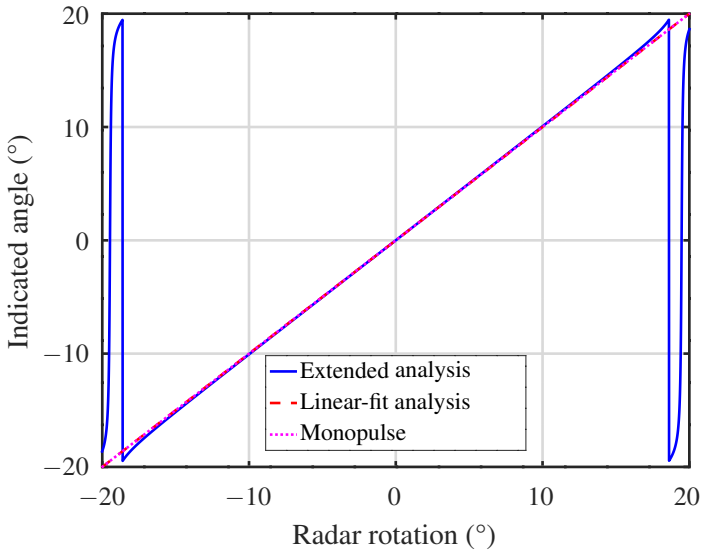

Figure 3.11. The effect of a cross-eye jammer on the indicated angle of a monopulse radar for $a = 0$ dB and $\phi = 0°$.

3.8.2 Effect on the indicated angle of a monopulse radar

The theoretical effect of a cross-eye jammer on the indicated angle of a monopulse radar for both the traditional phase-front analysis and extended analysis were investigated by using simulation. Figure 3.11 shows the effect for a case where the jammer paths are equal in amplitude and phase. It can be seen that the cross-eye jammer acts as a beacon for both analyses, and this result is to serve as a control for the simulation results to follow. Note that the dotted line indicates the monopulse ratio for the target platform when no cross-eye jammer is operational.

It can be seen in Figure 3.12 that, when the parameters are changed to $a = 1$ dB and $\phi = 170°$, an angular error is present. For radar rotations near 0°, the angular error for the extended analyses is very close to that of the phase-front analysis, and both are linear. However, as the radar is significantly rotated in either a negative or positive direction, the indicated angle of the extended analysis deviates from linear behaviour. In contrast, that of the phase-front analysis remains linear. It should also be noted that both analyses show instances where the indicated angle is 0°, which suggests that a tracking radar would lock onto and track a non-existing apparent target platform.

Figure 3.13 shows the indicated angle of the radar for a case where the jammer parameters are $a = 1$ dB and $\phi = 175°$. It can be seen that the indicated angle of the phase-front analysis has a constant angular

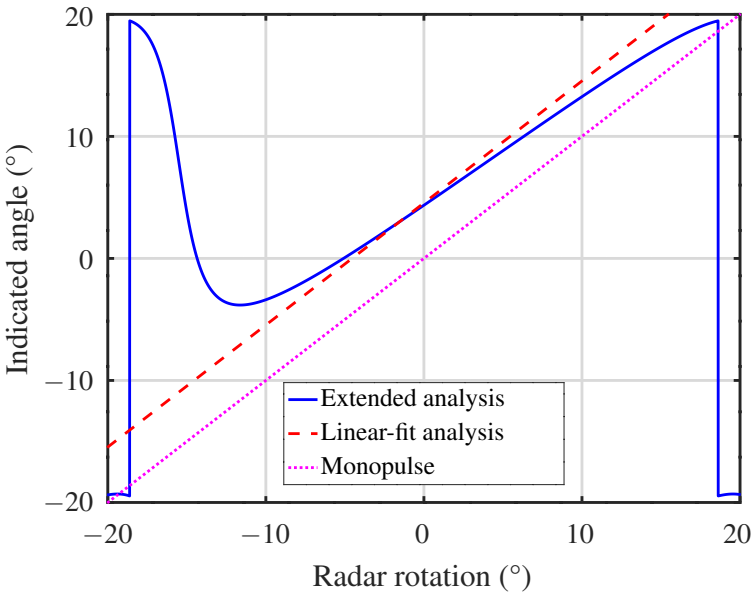

Figure 3.12. The effect of a cross-eye jammer on the indicated angle of a monopulse radar for $a = 1$ dB and $\phi = 170°$.

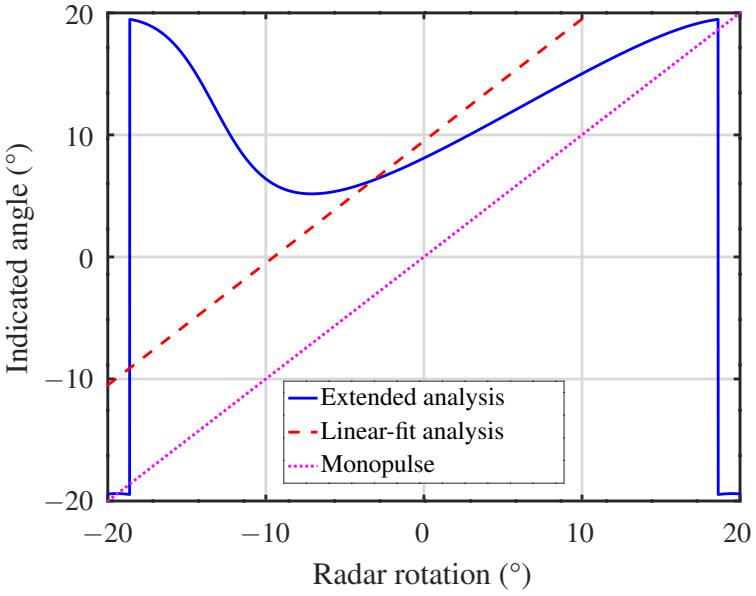

Figure 3.13. The effect of a cross-eye jammer on the indicated angle of a monopulse radar for $a = 1$ dB and $\phi = 175°$.

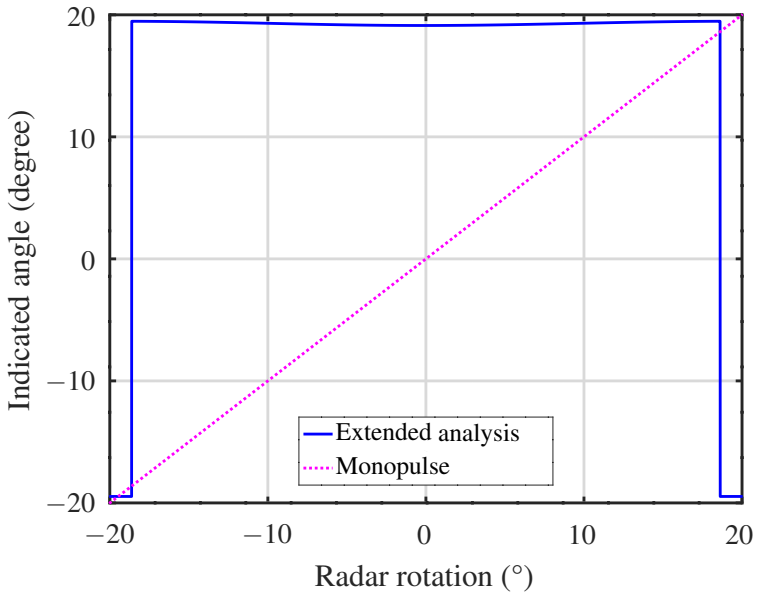

Figure 3.14. The effect of a cross-eye jammer on the indicated angle of a monopulse radar for $a = 0.01$ dB and $\phi = 180°$.

error, while that of the extended analysis is strongly non-linear. This results in enormous angular errors for negative radar rotations but smaller errors for positive rotations when considering the extended analysis. However, unlike the result of the phase-front analysis, the extended analysis shows that the indicated angle will never become zero for the specific parameters. This suggests that a tracking radar will never be able to lock onto any target, and a radar-guided missile will likely cancel its pursuit of the target platform [1], [4].

Figure 3.14 shows the indicated angle of just the extended analysis for a case where the parameters of the jammer are $a = 0.01$ dB and $\phi = 179.9°$, which is extremely close to the ideal parameters. It can be seen that the indicated angle converges to a constant value of almost 20° as the cross-eye gain converges to infinity. This is due to how a monopulse processor calculates the indicated angle. The calculation is done by using (3.15) for a certain value of M and solving for θ. In the case where $M \to \infty$, the inverse tangent from (3.15) converges to $\pi/2$. For the parameters in the simulation, this

can be calculated as

$$\theta_i = \lim_{M\to\infty}\left\{\sin^{-1}\left[\frac{2}{\beta d_r}\tan^{-1}(M)\right]\right\} \tag{3.76}$$

$$= \lim_{M\to\infty}\left\{\sin^{-1}\left[\frac{2}{(20\pi)(0.15)}\tan^{-1}(M)\right]\right\} \tag{3.77}$$

$$= 19.04^\circ\,. \tag{3.78}$$

The significance of the simulated result in (3.78) is that a cross-eye jammer with ideal parameters ($a = 1$ and $\phi = 180^\circ$) will result in a cross-eye gain of infinity. This would result in the monopulse ratio also becoming infinitely large. When considering the traditional analyses, a cross-eye gain of infinity would result in an infinite angular error. However, when considering the extended analysis, an infinite cross-eye gain results in the convergence of the indicated angle of the radar to a finite value that is dependent on the spacing of the radar antennas and carrier frequency. Although this suggests that the angular error from a cross-eye jammer will be much smaller than initially thought, it also suggests that the indicated angle will never become zero, regardless of the radar rotation. This would result in tracking radars losing their locks on target platforms [22].

Finally, it should be noted that the results in Figure 3.12 and Figure 3.13 show the same trends as the simulation results that were presented in [9] and [13]. This suggests that a comparable cross-eye effect can be recreated in a laboratory environment on a much smaller scale.

3.9 CHAPTER SUMMARY

A brief analysis of phase-comparison monopulse radar was provided, as it is the platform to be deceived by the jammer. The linear-fit, phase-front and extended analyses of cross-eye jamming were also recreated. It was determined that the linear-fit and phase-front analyses are based on glint analyses, where linear fits to the sum- and difference-channel patterns are made. In these analyses, the resultant angular error is constant and independent of the rotation of the radar. The extended analysis proved the first two analyses to be limited. It showed that by using the true monopulse antenna patterns, the angular error is not constant or linear and varies for different radar rotations. Unlike the linear-fit and phase-front analysis, the extended analysis also considers true retrodirectivity, resulting in a more suitable model for real-world applications. Finally, the extended model was simulated using arbitrary parameters chosen to represent measurements in a laboratory with confined space. The simulation concluded that the cross-eye effect in a small environment is comparable to that in the field. This

chapter provided the foundation on which the implementation of a retrodirective cross-eye jammer can be built.

CHAPTER 4 THE IMPLEMENTATION OF A RETRODIRECTIVE CROSS-EYE JAMMER

4.1 CHAPTER OVERVIEW

Various analyses of cross-eye jamming exist, and it was shown in Chapter 3 that the earlier analyses were limited by making assumptions that were not correct for the conditions of a practical jammer [9], [11], [18]. The limitations were only later found to exist when the extended analysis was done. Although this analysis made less assumptions and were believed to be accurate based on simulation, an uncertainty still exists of whether there might be detrimental real-world effects that could not have been predicted by the extended analysis when implementing a truly-retrodirective cross-eye jammer [9], [13], [14], [17]. To address this problem, it was needed to develop a truly-retrodirective cross-eye jammer. As part of the development, a platform was needed to test the jammer. This chapter presents the full design and implementation of a retrodirective cross-eye jammer by using an SDR, and the development of a one-dimensional phase-comparison monopulse radar to test and calibrate it with.

4.2 ACQUISITION OF AN ANGULAR RADAR FOR JAMMER TESTING

As the primary objective of this study was to implement a retrodirective cross-eye jammer on an SDR to validate previous analyses, the approach was to develop a cross-eye jammer on an SDR and use a monopulse radar to calibrate it in an anechoic environment. The problem with this was the lack of availability of commercial monopulse radars. Firstly, it was not feasible to purchase or hire such a system. Secondly, radar developers are secretive about the operation of their systems due to the high competitiveness in the industry.

It was decided to use a second SDR to implement a one-dimensional monopulse radar. The radar would then be calibrated and characterised, after which it would be used to calibrate and test a cross-eye jammer, all in an anechoic environment. The radar would then compete against the jammer in a series of experiments.

4.3 MONOPULSE RADAR

4.3.1 Angular processing

It was decided to design a one-dimensional phase-comparison monopulse radar. This was due to the robustness of the exact monopulse processor and the fact that the most extensive previous analyses of cross-eye jamming were based on this type of angular radar [4], [9], [28]. The choice of using a one-dimensional system was based on the fact that a cross-eye jammer can only operate in one dimension, which is sufficient as significant angular errors are only needed in one dimension for angular deception [9]. It should be added that although cross-eye jammers are one-dimensional, they can create errors in both azimuth and elevation if components from both are received at the jammer [9].

4.3.2 RF hardware platform

It was decided to do the implementation by using a Nuand bladeRF 2.0 SDR, as this was an SDR that was available in the academic environment that also had two receive channels [32]. Monopulse radars need two or more receive channels as the return signals at two or more antennas have to be sensed simultaneously [4], [5].

Another reason for the choice of this SDR was that it uses an AD9361 RF transceiver. This RF IC has a relatively-high sampling rate of 61.44 MSps, and a vast frequency operating range, which is from 47 MHz to 6 GHz on the transmitter, and 60 MHz to 6 GHz on the receiver [39].

Although the transceiver only has a maximum transmission power of 8 dBm (during continuous transmission), it was still sufficient for the implementation of a radar operating at very short ranges [39]. As the cross-eye jammer testing was to happen in a confined laboratory environment, the small operating range of the radar would not affect the outcome, and it was not even needed to use external power amplifiers. Although power amplifiers might have been beneficial in increasing the SNR of the radar return, such amplifiers were unavailable, and the cost of acquisition outweighed the benefit of the SNR increase.

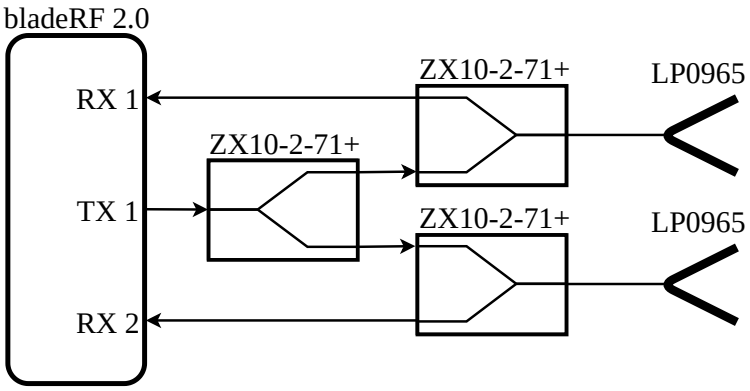

Figure 4.1. The connection between the SDR and antennas of the radar. Adapted from [23], © 2021 IEEE.

4.3.3 Antenna selection

It was decided to use two log-periodic antennas, manufactured by Ettus Research, as the radar antennas [40]. The antennas were chosen as they had a wide band of operation (from 850 MHz to 6.5 GHz) due to the nature of the antenna type [40]. Each antenna also had a sufficiently-high gain of about 6 dBi, although this varied slightly at different operating frequencies [40].

4.3.4 Connection between the antennas and SDR

It was chosen to use one transmit channel and connect the SDR to the log-periodic antennas by using three power dividers, as can be seen in Figure 4.1. It was also decided to use the ZX10-2-71+ power divider from Mini-Circuits. The component was cost-effective and well within the operating frequency band of the SDR and antennas. At 3 GHz, the component has an insertion loss of about 3.5 dB and isolation between ports 1 and 2 of about 11.5 dB [41]. The high isolation made it possible to transmit and receive simultaneously, without the transmit signal saturating or damaging the RF receivers of the SDR.

4.3.5 Waveform synthesis

It was decided to transmit only a single pulse, as opposed to a burst of pulses. This was done to reduce the processing time added if Doppler processing were to be used. The trade-off for this was a lower SNR as Doppler processing would result in extra processing gain. Doppler processing was not needed to distinguish a target from the environmental clutter as the radar had the sole purpose of operating in

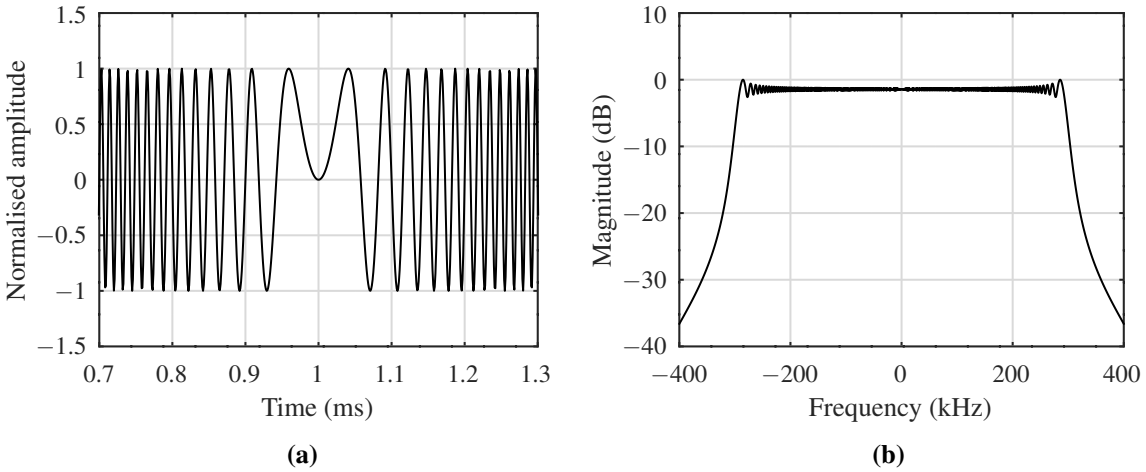

Figure 4.2. An illustration of the (a) time domain and (b) frequency domain response of the synthesised LFM pulse.

an anechoic environment for jammer testing. Due to the short-range anechoic environment, the added processing gain that would be achieved using a pulse-Doppler radar was not needed.

It was decided to use an LFM waveform as this can generally accommodate high bandwidths and has good time SLL performance when used for pulse compression [5]. It was decided to create the LFM pulse with a frequency around 0 Hz in baseband, or equivalently, around the carrier frequency in RF. This was to avoid the introduction of phase shifts into the pulses.

Given that the pulse is causal and centred around 0 Hz in the baseband, it can be expressed as

$$p(t) = \text{rect}\left(\frac{t}{\tau} - \frac{1}{2}\right) e^{j\pi[(\frac{B}{\tau})t^2 - Bt]}, \tag{4.1}$$

where B is the bandwidth of the pulse and τ is the pulsewidth. The rectangular function with the shift of $\frac{1}{2}$ just indicates that the LFM pulse has an amplitude of 1 for $0 \leq t \leq \tau$, and 0 for all other values. The real part of the LFM pulse in time is shown in Figure. 4.2(a), while its frequency domain response can be seen in Figure. 4.2(b). Note that the LFM pulse is only partially shown in the time domain as higher frequency components cannot be distinguished from one another. The true span of the LFM pulse is from 0 ms to 2 ms.

The sampling rate of the system, f_s, was selected to be 1 MSps as this rate is well below the maximum sampling rate per RF channel if the SDR is operated in full multiple-input and multiple-output (MIMO)

mode [32]. This also ensured no bottleneck of samples through the USB 3.0 channel when operating the SDR in this mode. The bandwidth of the pulse was selected to be 60% of the sampling rate, which is 600 kHz. This was chosen to allow for some oversampling to ensure that aliasing is not significant [26]. Note that the internal anti-aliasing filter of the SDR (also referred to as the baseband filter) was set to be equal to the bandwidth of the signal, and the oversampling allowed for the filter to achieve significant attenuation at the sampling frequency.

The width of the pulse, and inherently the integration time, was chosen to be 2 ms. This equated to a minimum range of 300 km. Even though this range is not feasible for a practical system, it was feasible for the use of a radar against a repeater with a latency greater than 2 ms [5]. Given that a cross-eye jammer is a repeater-based system, the large pulsewidth of the radar was not expected to adversely affect the system and the longer integration time compensated for the processing gain that was potentially lost by choosing not to use Doppler processing.

4.3.6 Radar software development

The monopulse radar was implemented with GNU Octave 5.2, which was an effective platform for doing radar processing, as it did not have to be done in real-time. Octave also provided the functionality of accessing the Linux system directly, enabling the use of the bladeRF command line interface (CLI) through the Octave environment. A functional flow diagram of the monopulse radar is given in Figure 4.3.

The first functional block, FU 1.1, was the initialisation of the system, where parameters specific to the radar itself were chosen. This included the carrier frequency, channel bandwidth and sampling rate. In FU 2.1 and FU 2.2, the chosen parameters were applied to the SDR by using the system command in Octave to set the hardware parameters in the CLI. The third functional block, FU 3.1, was the synthesis of the LFM radar pulse, as described in the previous section.

The complex LFM pulse had to be interleaved to be transmitted by the device, as indicated by FU 4.1. The interleaving is best described mathematically as

$$\left[I + jQ, \quad I + jQ\right] = \left[I, \quad Q, \quad I, \quad Q\right], \tag{4.2}$$

with I and Q indicating the in-phase and quadrature components of the signal, respectively.

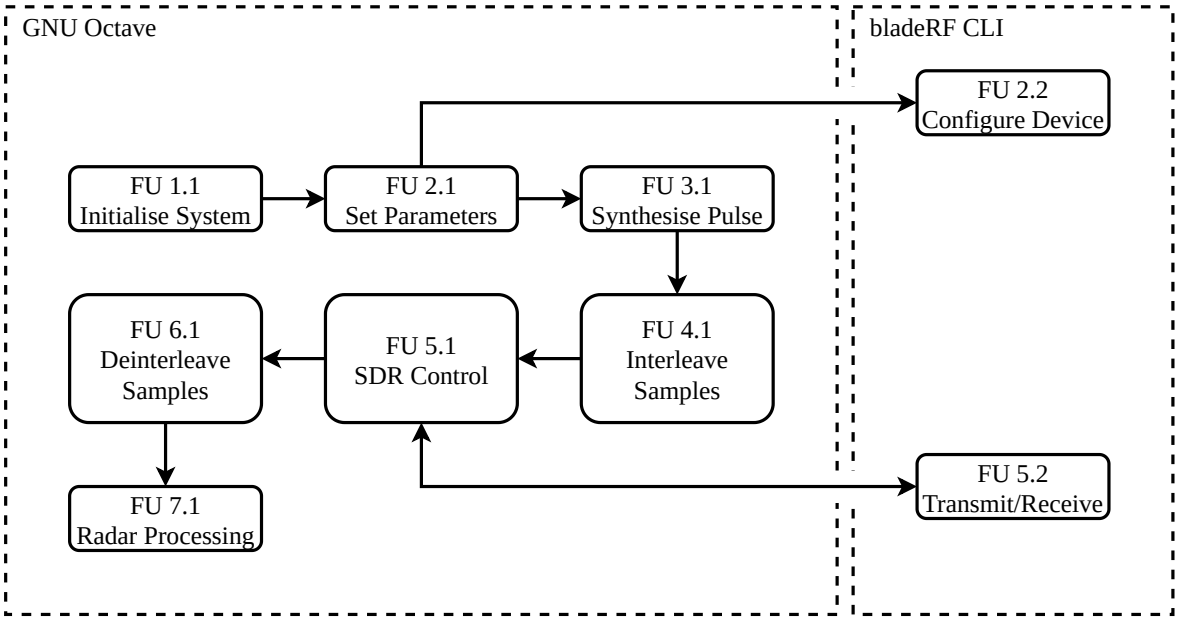

Figure 4.3. Functional flow diagram of the monopulse radar.

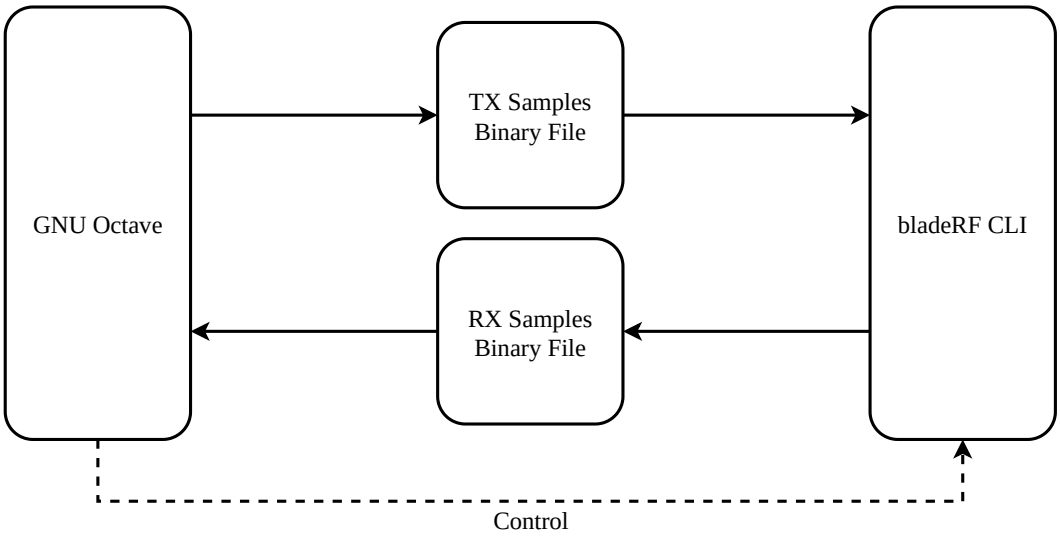

Figure 4.4. Flow diagram of the SDR control.

The transmit and receive operations of the radar was implemented by using Octave to control the CLI while using file input/output streams to move samples between the CLI and Octave, as shown in Figure 4.4. The interleaved samples were first saved to a binary file, after which Octave was used to set the file as an input to the CLI. The samples in the file were then transmitted. As the transmission occurred, the reception was started, and the received samples were stored in a second binary file, which was then read by Octave.

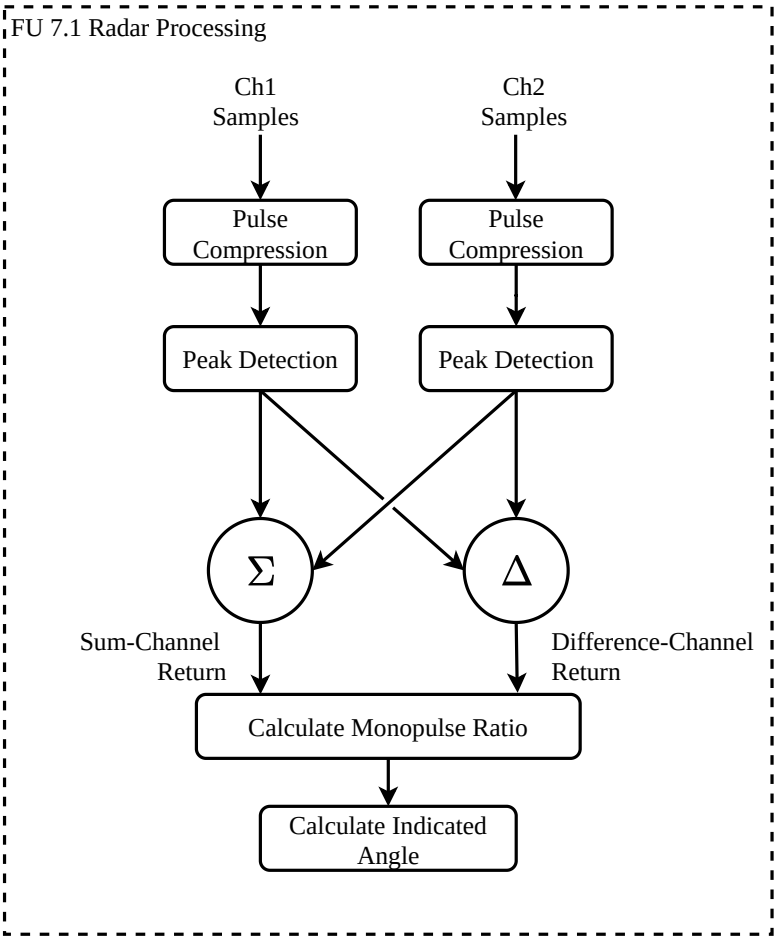

Figure 4.5. Flow diagram of the implementation of the radar processing.

As indicated in FU 6.1, the received samples had to be deinterleaved. This was more complicated than with the interleaving, as the reception was done on two channels. The process of deinterleaving can be expressed as

$$\begin{bmatrix} I_1, & Q_1, & I_2, & Q_2 \end{bmatrix} = \begin{bmatrix} I_1 + Q_1 j & I_2 + Q_2 j \end{bmatrix} , \tag{4.3}$$

where I_1 and Q_1 are the in-phase and quadrature samples of the first channel, respectively, while I_2 and Q_2 are the in-phase and quadrature samples of the second channel. The format of the interleaved and deinterleaved signals can also be seen in (4.3).

Finally, radar processing was done, which is demonstrated in the flow diagram in Figure 4.5. The deinterleaved samples of the two channels were used as the input to the radar processing. Pulse-compression was applied to the samples by convolving them with the time-reversed complex conjugate of the synthesised pulse. This was done by using linear fast convolution, where the fast Fourier

transform (FFT) of both the received samples and the time-reversed complex conjugate of the pulse, padded with zeros, were taken and multiplied. The inverse fast Fourier transform (IFFT) was then used to convert the resultant signal back to the time domain. Peak detection was applied to the pulse compression output of each channel by iterating through the magnitude responses of the signals and searching for a localised maximum value that is larger than a set threshold. The two complex samples corresponding to the detected peaks on both channels were then returned.

Monopulse processing was applied by subtracting the resultant sample of the first channel from that of the second to form the difference-channel return. Similarly, the two samples were also added to form the sum-channel return. The monopulse ratio was then obtained by dividing the difference-channel return by the sum-channel return and only keeping the imaginary part. Finally, the indicated angle was calculated by using (3.15) and solving for θ, which can be expressed as

$$\theta_i = \sin^{-1}\left[\frac{2}{\beta d}\tan^{-1}(M)\right], \tag{4.4}$$

where θ_i is the indicated angle, β is the phase-propagation constant, d is the spacing between the antennas and M is the monopulse ratio.

4.4 CROSS-EYE JAMMER

4.4.1 RF platform selection

As with the radar, it was decided to use a Nuand bladeRF 2.0 to implement the cross-eye jammer. Firstly, it was needed to use an SDR as this was a fundamental requirement of this study. The SDR enabled rapid RF prototyping at a relatively low cost. The bladeRF 2.0 was selected as it was available, has two transmit and two receive channels, and has a wide band of operation (between 47 MHz and 6 GHz on the transmitter, and between 70 MHz and 6 GHz on the receiver) [32].

The bladeRF 2.0 also has two channels for transmission and two for reception. The carrier frequencies of the two receivers and the two transmitters are synchronised per default [32]. This was extremely important as coherency was needed to ensure that the jammer paths were continuously retrodirective [9].

4.4.2 Retrodirective connection

The jammer SDR was connected to two Ettus LP0965 log-periodic antennas by using two ZNPD2-63-S+ power dividers. As with the radar, these antennas were chosen based on the wide frequency

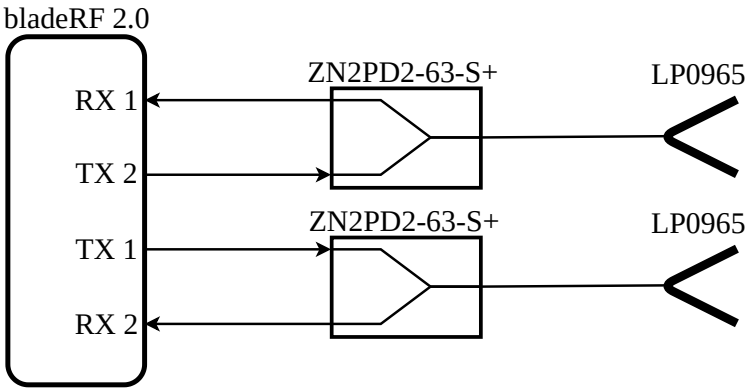

Figure 4.6. The connection between the SDR and antennas of the jammer. Adapted from [23], © 2021 IEEE.

band of log-periodic antennas and the known parameters that were characterised by Ettus [40]. The choice of power dividers was not only due to the availability of the device and the fact that it had an operating band within the bands of the SDR and antennas, but also because of the high isolation of 30 dB between port 1 and port 2 at an operating frequency of 3 GHz.

The connection between the SDR and antennas, which is illustrated in Figure 4.6, was in the form of a Van Atta array, corresponding to the layout shown in Figure 2.13. It can be seen that the first receive and second transmit channels of the SDR were connected to an antenna, while the second receive and first transmit channels were connected to the other antenna to form a connection similar to that in Figure 2.13. It should be noted that this hardware configuration is only a part of the Van Atta implementation and that two repeater paths with no phase difference between them are needed to achieve retrodirectivity.

Figure 4.7 is an adapted version of Figure 2.13 and illustrates the retrodirective paths. The blue dashed line shows the path that the signal that undergoes the amplitude and phase shift travels, while the red line shows the path that the unchanged signal travels. The circulators from Figure 2.13 are replaced by power dividers, and the SDR is indicated by a black dashed line box. It can be seen that the solid black lines between the power dividers and antennas are the common parts of the two paths. This means that the phase length of these connections do not matter, as the signal will cancel it through the opposite path. Therefore, the ideal jammer parameters ($a = 1$ and $\phi = 180°$) are only needed between the blue and red retrodirective paths.

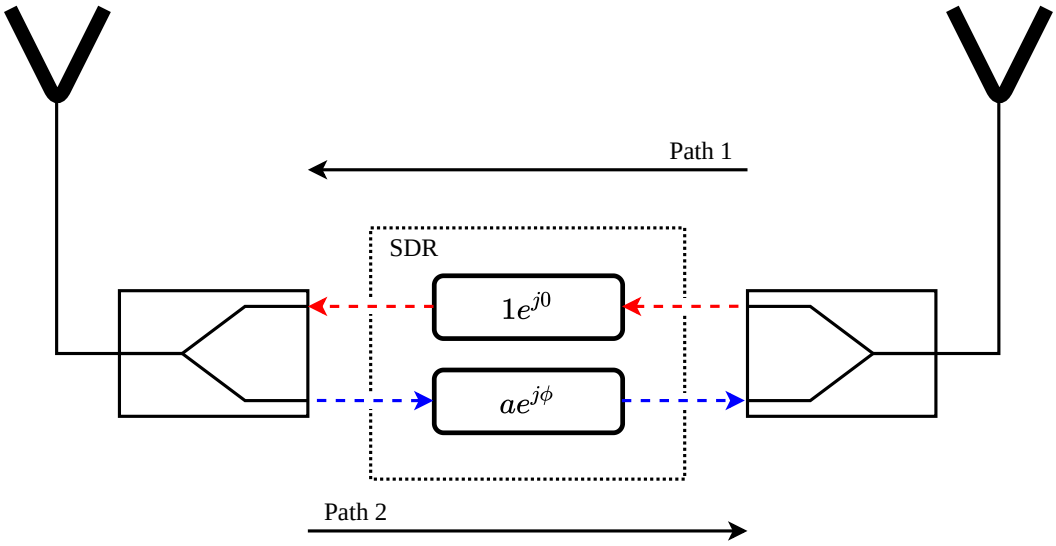

Figure 4.7. An illustration of the retrodirective paths of the jammer.

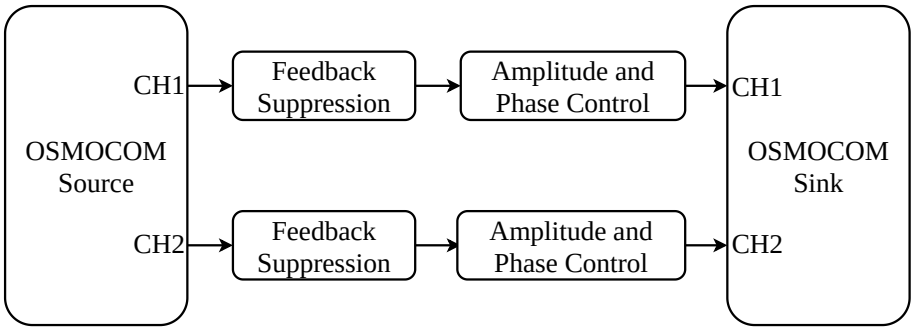

Figure 4.8. Overview of the system that was implemented in GNU Radio.

4.4.3 Cross-eye software design

The bladeRF 2.0 that was used for the jammer was controlled by using a flow diagram implementation in GNU Radio Companion 3.8.1, as illustrated in Figure 4.8. The osmocom source and sink blocks from the gr-osmosdr package in GNU Radio were used to control the reception and transmission of both channels of the SDR. The signal received on each channel underwent feedback suppression and amplitude and phase control before being re-transmitted on the corresponding transmit channel.

The system parameters, including the transmitter's total gain, the threshold values for feedback suppression, the amplitudes of the paths, and the phase-difference between the paths, were all controlled while the GNU Radio flow diagram was busy executed. The parameters were adjusted by using sliders in a Qt GUI, while the in-phase and quadrature components of the signal in each path, just before

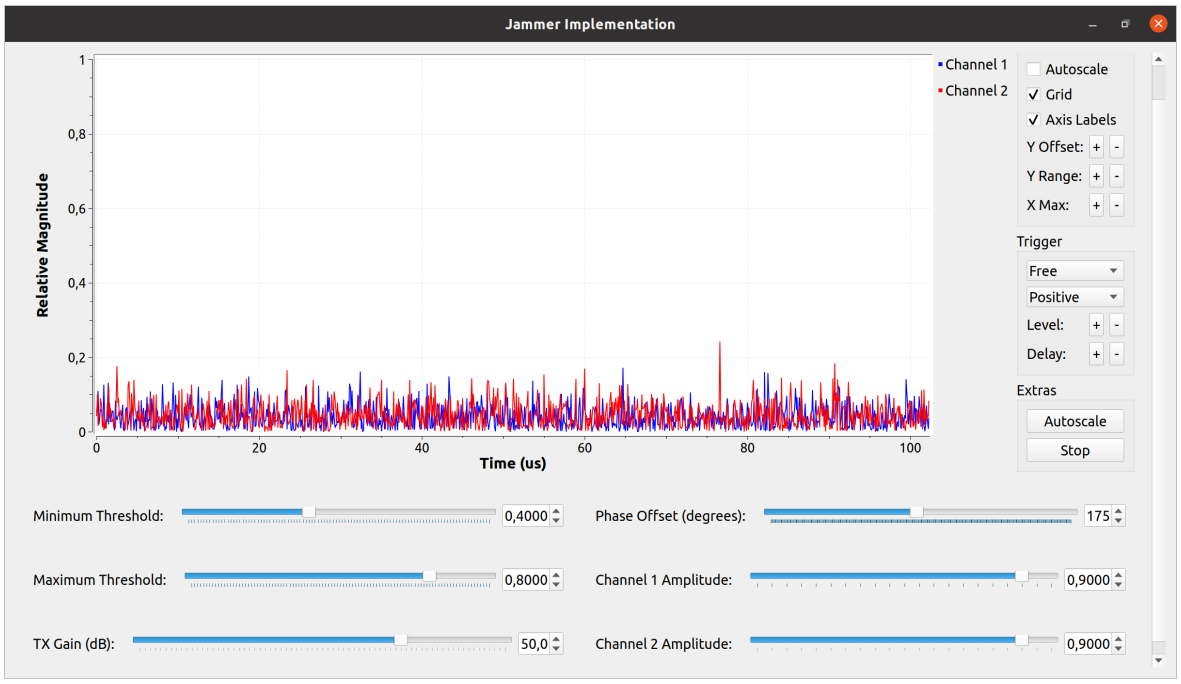

Figure 4.9. Screen capture of the graphical user interface (GUI) that was used to implement the jammer on GNU Radio.

transmission, were displayed using Qt time sinks. A screen capture of the GUI can be seen in Figure 4.9. The display of each path before the transmission was done to ensure that the transmitter gain and feedback suppression thresholds were set up correctly and to verify that no feedback was experienced when transmitting the radar pulse towards the jammer.

The amplitude scaling was applied to each channel by multiplying the channel by the amplitude value set in the GUI. The amplitude control was done on both channels to allow for overall amplitude reduction to counteract feedback. The phase control was done similarly, but a phase offset was only applied to one channel. The offset was applied by using a custom Python code block to multiply the channel by $e^{-j\psi}$, where ψ was the desired phase offset in radians. For ease of use, the value from the slider in the GUI was in degrees, and the values had to be converted to radians for the phase adjustment.

A feedback suppression algorithm also implemented in GNU Radio was applied to the channels before transmission. The algorithm, which is illustrated in the flow diagram in Figure 4.10, worked by multiplying the transmitted signal by zero if a maximum magnitude threshold is reached, leading to nothing being transmitted and counteracting the feedback that caused the magnitude to spike. The

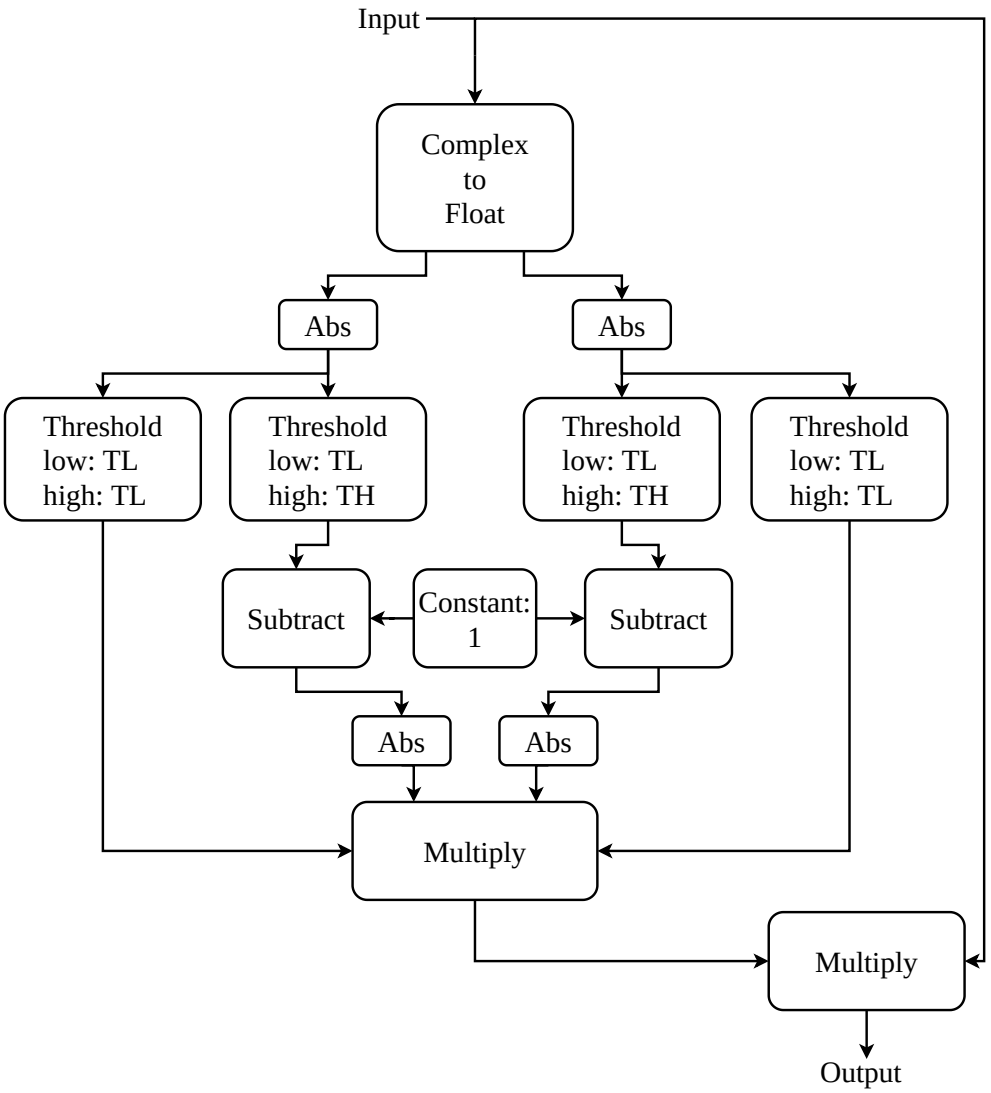

Figure 4.10. Flow diagram of the feedback suppression algorithm that was implemented in GNU Radio.

multiplication with zeros is only removed after the signal to be transmitted dropped below a certain magnitude, indicating that no feedback is present anymore. Furthermore, the algorithm also multiplied the signal by zero when the threshold was below a certain minimum threshold. The threshold was slightly higher than the magnitude of the noise floor, which led to the prevention of the transmission of a noise-only signal. Both the minimum and maximum thresholds were controllable in the GUI during the execution of the GNU Radio flow diagram.

A simulation of the feedback suppression algorithm is demonstrated in Figure 4.11, where the algorithm is applied to an arbitrary signal, shown in Figure 4.11(a). Here, the minimum magnitude threshold is

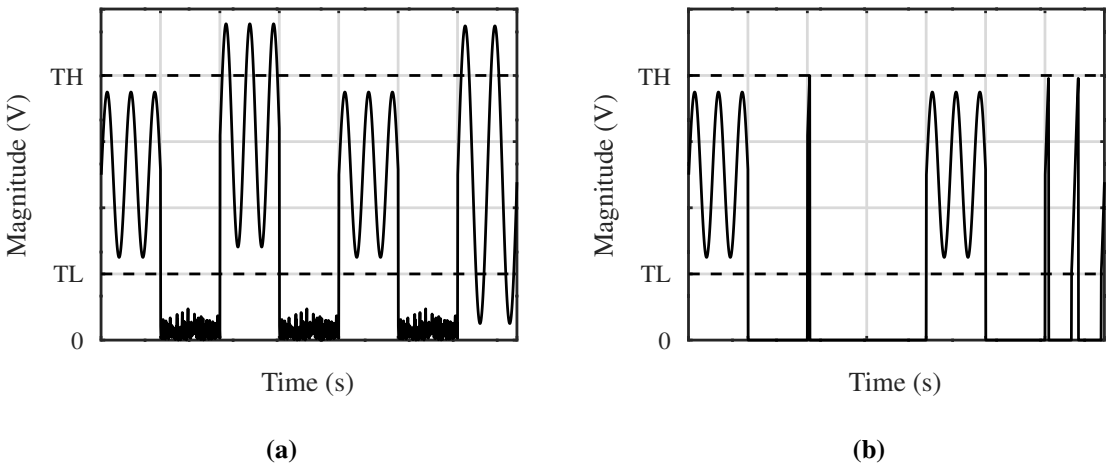

Figure 4.11. An example of (a) an input signal and (b) the corresponding output signal when applying the feedback suppression algorithm.

denoted by TL, and the maximum magnitude threshold is denoted by TH. The output of the algorithm is demonstrated in Figure 4.11(b). By comparing the input to the output, it can be seen that a signal with a magnitude between the minimum and maximum thresholds passes through normally. However, when the signal crosses a maximum magnitude threshold, the signal is multiplied by zero, hence blocked from reaching the output. Only when the input signal attenuates to the minimum threshold, the signal continues to pass through normally. When the signal comprises of pure noise below the minimum threshold, the signal is again multiplied by zero and does not pass through to the output.

4.5 CHAPTER SUMMARY

The chapter commenced with a discussion of the approach. To address the research problem, a retrodirective cross-eye jammer had to be implemented by using SDR. An angular radar system was needed to test the jammer. It was not feasible to purchase an angular radar due to the high cost. It was also not possible to obtain an angular radar from a local radar developer due to the secretive and competitive nature of the industry. Therefore, it was decided to implement a one-dimensional phase-comparison monopulse radar. The choice of the radar was due to its use in previous cross-eye analyses. The radar was implemented by using a second SDR. The device of choice was a bladeRF 2.0, as it was readily available and had two receive and two transmit channels. The SDR was connected to two antennas that were spaced apart to ensure two phase centres. The operation of the radar was started by the transmission of single LFM pulse and recording data with the two receive channels of

the SDR. Pulse compression was used to improve the SNR of recorded data, and basic peak detection was used to determine whether a radar return signal was present. Monopulse processing was then used to obtain the angular information that was conveyed by the return signal. A two-channel repeater was then implemented by connecting the first SDR, which was also chosen to be a bladeRF 2.0, to two log-periodic antennas in a Van Atta configuration by using available power dividers. The internal operation of the repeater was implemented in GNU Radio, and a GUI was created to allow for the real-time adjustment of the magnitudes and phases of the two paths of the repeater. This was needed for the calibration of the retrodirective beacon and retrodirective cross-eye jammer. Finally, a feedback reduction technique was also implemented in GNU Radio to mitigate the possible effects of insufficient isolation between the repeater paths. The method worked by transmitting only zeros instead of repeating the incoming signal if the incoming signal crossed a certain maximum threshold. In addition, a lower threshold was also set to counter the transmission of noise-only signals.

CHAPTER 5 MEASUREMENT AND CALIBRATION

5.1 CHAPTER OVERVIEW

The implementations of a retrodirective cross-eye jammer and phase-comparison monopulse radar were given in Chapter 4. However, the implemented systems still required calibration to operate correctly. Additionally, well-designed experiments were needed to test both systems and provide results with integrity.

This chapter introduces the calibration procedures for the monopulse radar to ensure that the difference-channel antenna pattern has a null at broadside of the radar. Furthermore, a new method of calibrating a cross-eye jammer to obtain the ideal magnitude factor and phase difference between the retrodirective paths is also presented. Experimental setups and procedures are given to test the functionality of the radar and jammer. Finally, a method of calibrating the measured results for possible deviations in the setup is presented.

Important Note: The cross-eye jammer in this study can be considered to be a special case of a retrodirective repeater, where the magnitudes of the paths are equal, but where the phase difference between the phase are precisely 180° out of phase. Therefore, references to the jammer and to the repeaters refer to the same system but with different configurations. As an extension to this, the terms *repeater antennas* and *jammer antennas* refer to the same antenna array and may be used interchangeably.

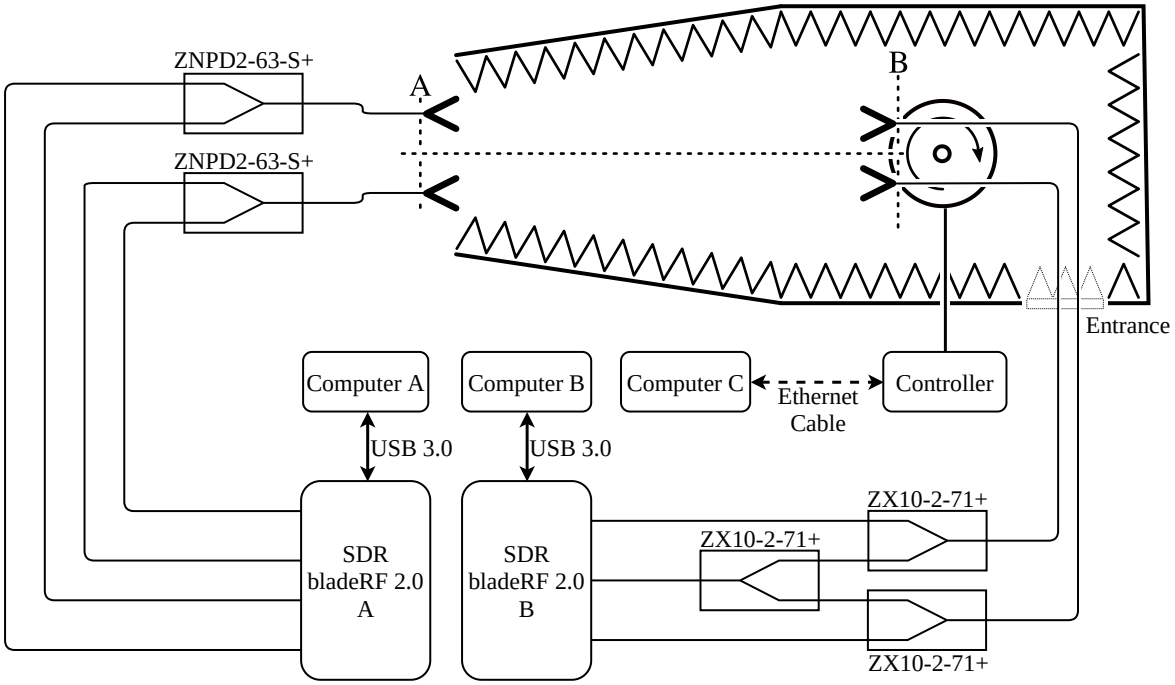

Figure 5.1. Experimental setup for radar rotation measurements.

5.2 EXPERIMENTAL SETUP

Two experimental setups were used, and are shown in Figure 5.1 and Figure 5.2, respectively. The first experimental setup was for the case where the two radar antennas were placed on the positioner while the two repeater antennas were placed on a tripod at the opening of the tapered anechoic chamber. The setup is demonstrated in Figure 5.1, where the antennas at A were that of the repeater, while the antennas at B were that of the radar. Photographs of the radar antennas on the positioner can be seen in Figure 5.3 and Figure 5.4. The roughly measured distance between the positioner and the opening of the tapered anechoic chamber was about 5 m. In addition, the spacing between the radar antennas were about 0.134 m, as that is the width of the bases of the log-periodic antennas that were used [40].

The positioner itself was connected to a controller with cables underneath the anechoic foam. The controller was interfaced with a computer using the TCP/IP standard through an Ethernet cable to allow for the control of the positioner through a simple GUI on the computer (indicated as Computer C in Figure 5.1).

The radar antennas were mounted on the positioner by attaching them to a wooden block and attaching the block to an available mounting bracket connected to the positioner's rotating surface. Due to the

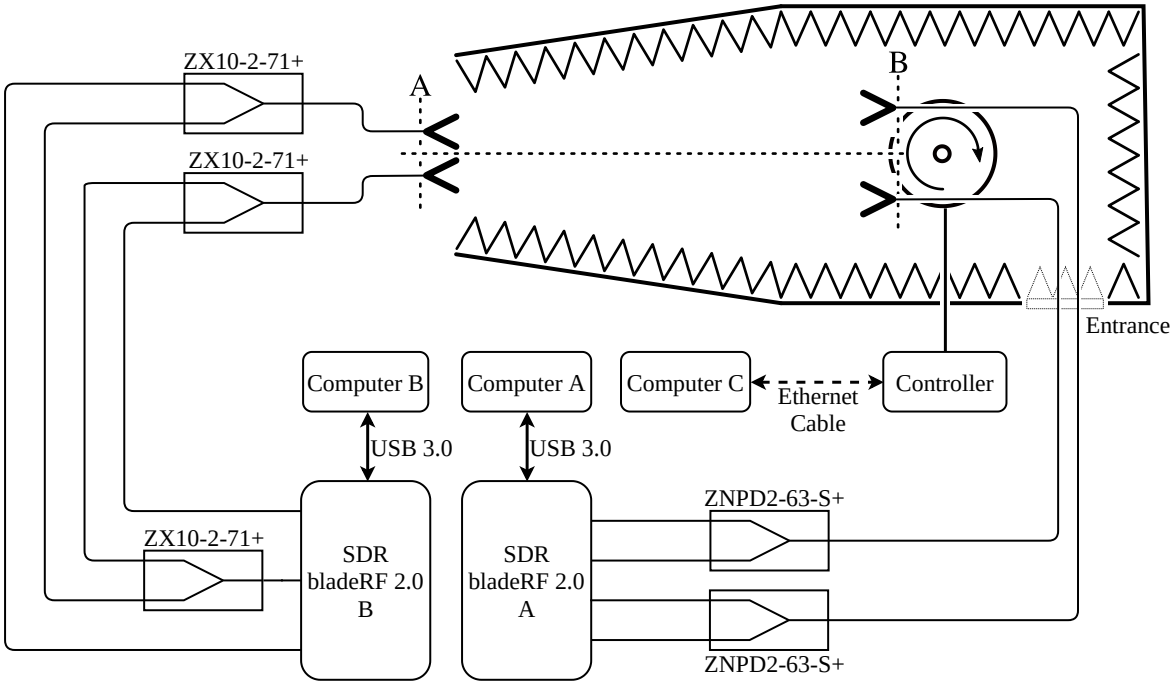

Figure 5.2. Experimental setup for jammer rotation measurements.

nature of the mounting bracket, the centre of the antenna array could not be positioned over the centre of the positioner to allow for perfect concentric rotation. It was decided to leave it as is and calibrate for adverse effects after the measurements.

The antennas of both the radar and repeater were connected to power dividers, which in turn were connected to the SDRs, as explained in Section 4. All RF connections were made by using RG-58 coaxial cables that were available. All coaxial connections were relatively short, all under 0.5 m, except for the connections between the repeater antennas and the power dividers, which were about 10 m each. By extrapolating the data in the attenuation versus frequency graph, a 10 m cable would attenuate a signal by around 10 dB, which would usually be significant. However, the effect was negligibly small due to the short distance between the radar and repeater antennas.

For the second experimental setup, the jammer antennas were mounted on the positioner, while the radar antennas were mounted on the tripod at the opening of the anechoic chamber, as illustrated in Figure 5.2. All connections and hardware remained the same, but with the positions being switched around. Finally, it should be reiterated that two separate SDRs and two independent computers were used to operate the repeater and the radar, respectively. A photograph of the repeater antennas that was

Figure 5.3. Photograph of the radar antennas mounted on the positioner in the anechoic chamber. The SDR and computer running the radar code can also be seen. (Photo credit: Prof. W. P. du Plessis)

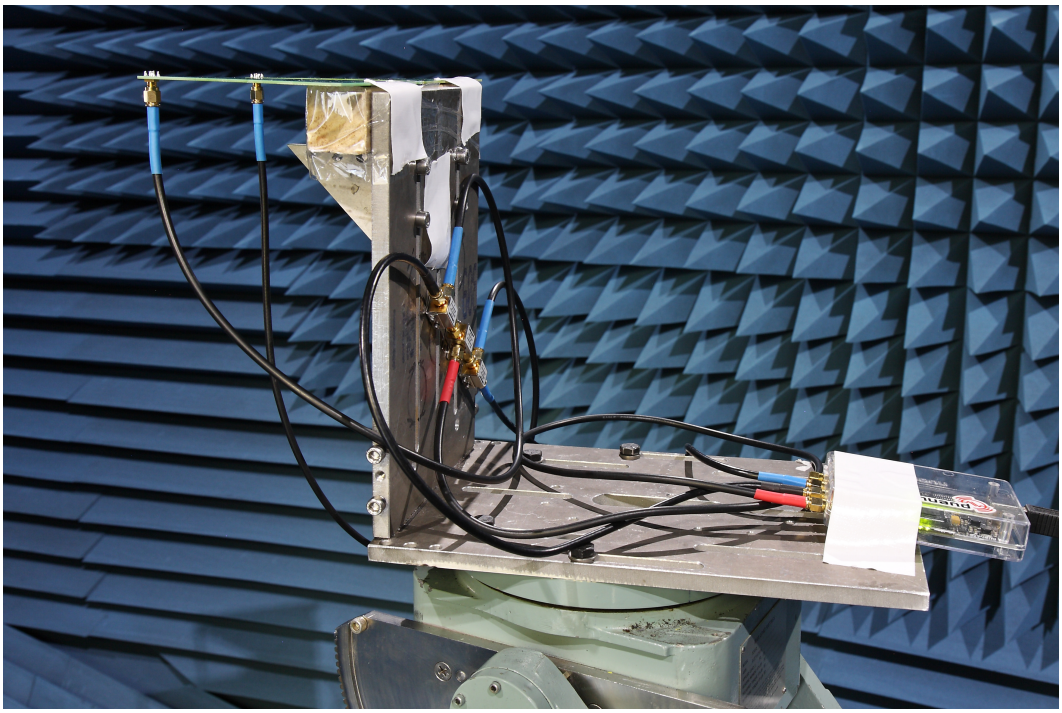

Figure 5.4. A close-up photo of the radar antennas mounted on the positioner. The SDR and power dividers can also be seen. (Photo credit: Prof. W. P. du Plessis)

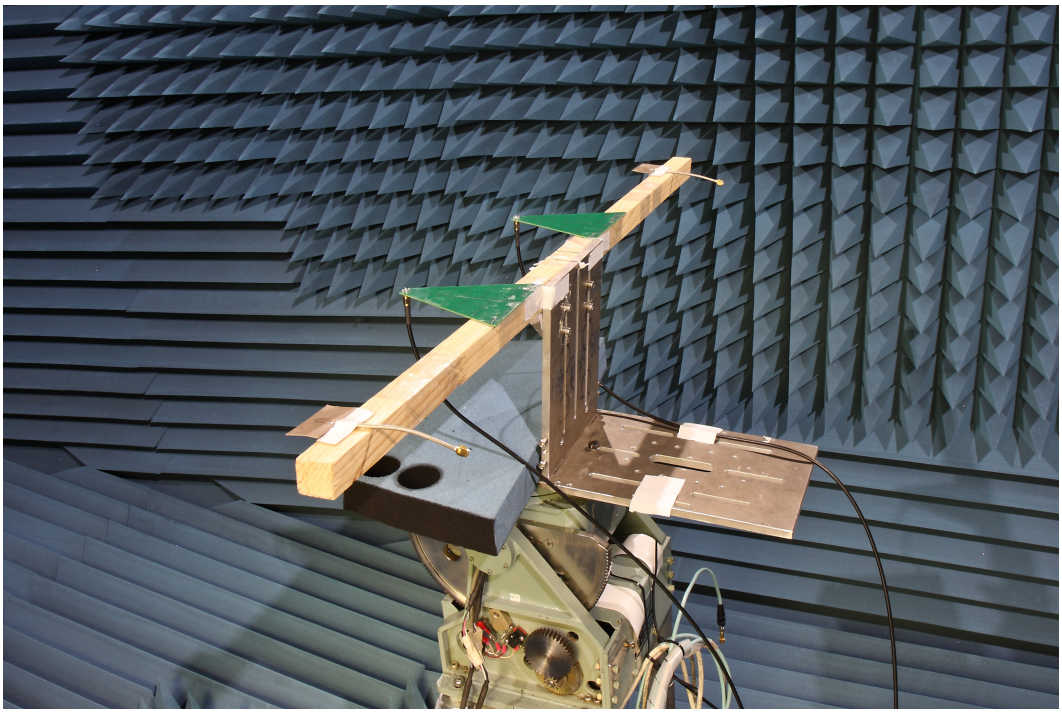

Figure 5.5. Photograph of the repeater antennas mounted on the positioner in the anechoic chamber. (Photo credit: Prof. W. P. du Plessis)

taken from behind is shown in Figure 5.5, while photographs of the same setup, as viewed from the opening of the anechoic chamber's tapered end, are shown in Figure 5.6 and Figure 5.7. A photograph of the radar antennas that were mounted on a tripod at the opening of the chamber is given in Figure 5.8, where the small diameter of the opening can also be seen.

5.3 MAIN CALIBRATION

The first calibration protocol was done with the radar and repeater set up as illustrated in Figure 5.1. Here, the positioner was set to no rotation to allow the radar to be on broadside of the repeater, while the repeater was on broadside of the radar.

The calibration was done before the recording of the measurements and was divided into two tasks. The first was the calibration of the monopulse radar to ensure that the difference-channel return was at a minimum for the case of no rotation, as the repeater was on broadside of the radar. The second task was the calibration of the jammer to achieve the desired phase difference and amplitude factor between the jammer paths. As no practical retrodirective cross-eye jammer implementation was given in the literature, the calibration of the jammer was a research contribution of this study.

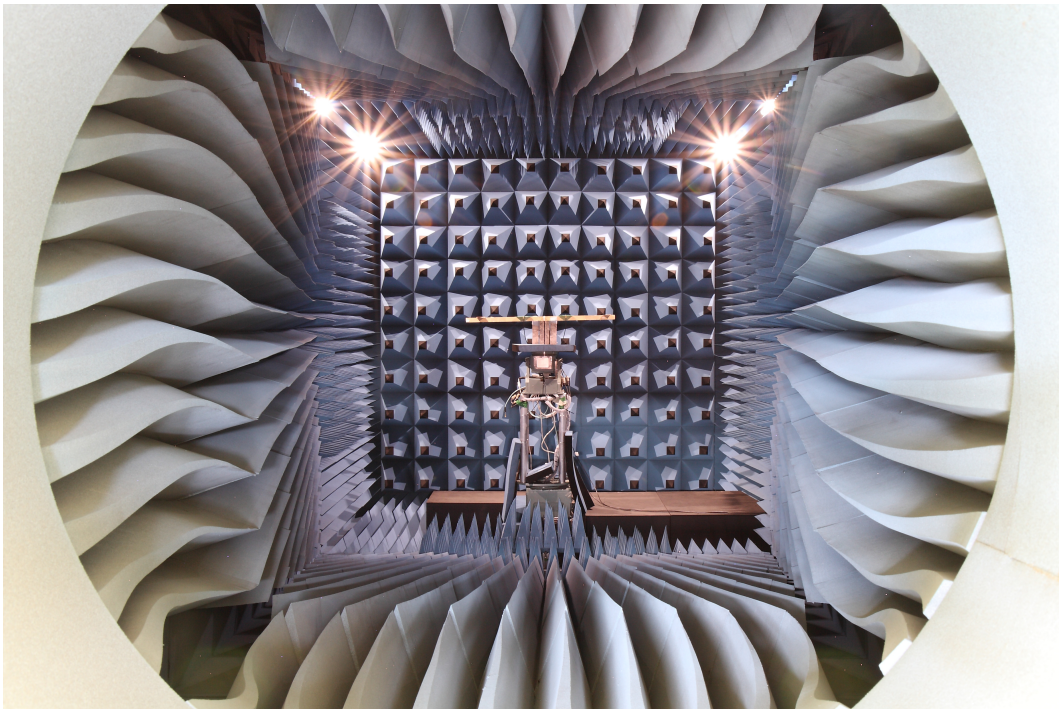

Figure 5.6. Photograph of the repeater antennas mounted on the positioner as seen from the outside of the opening of the tapered end of the chamber. (Photo credit: Prof. W. P. du Plessis)

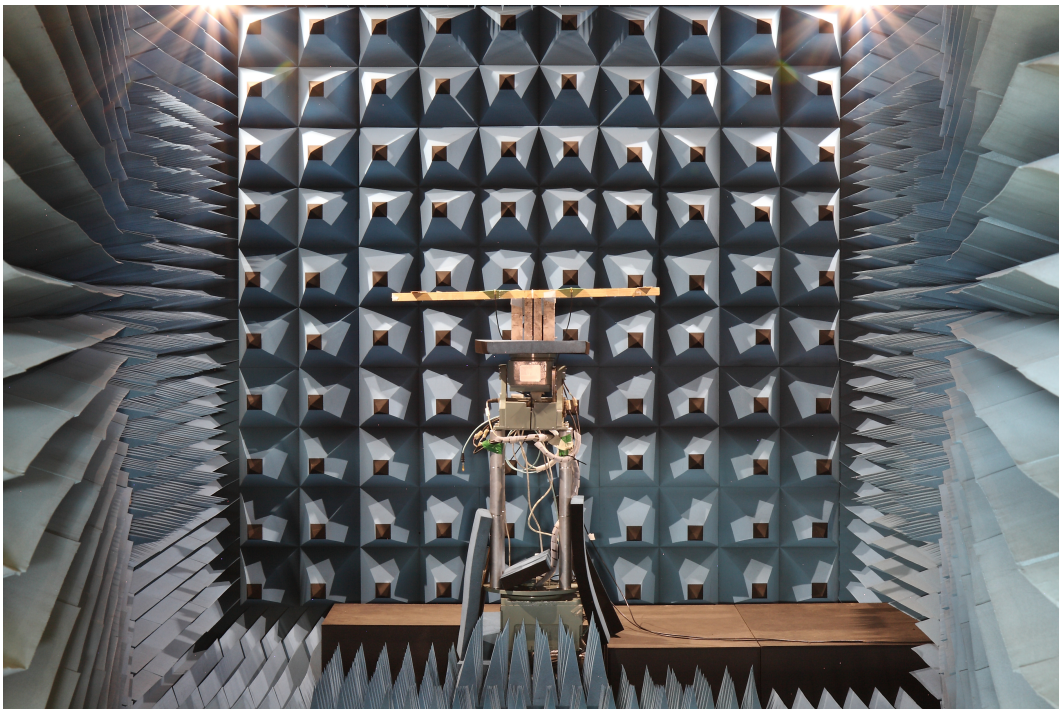

Figure 5.7. A second photograph of the repeater antennas mounted on the positioner as seen from the outside of the opening of the tapered end of the chamber. (Photo credit: Prof. W. P. du Plessis)

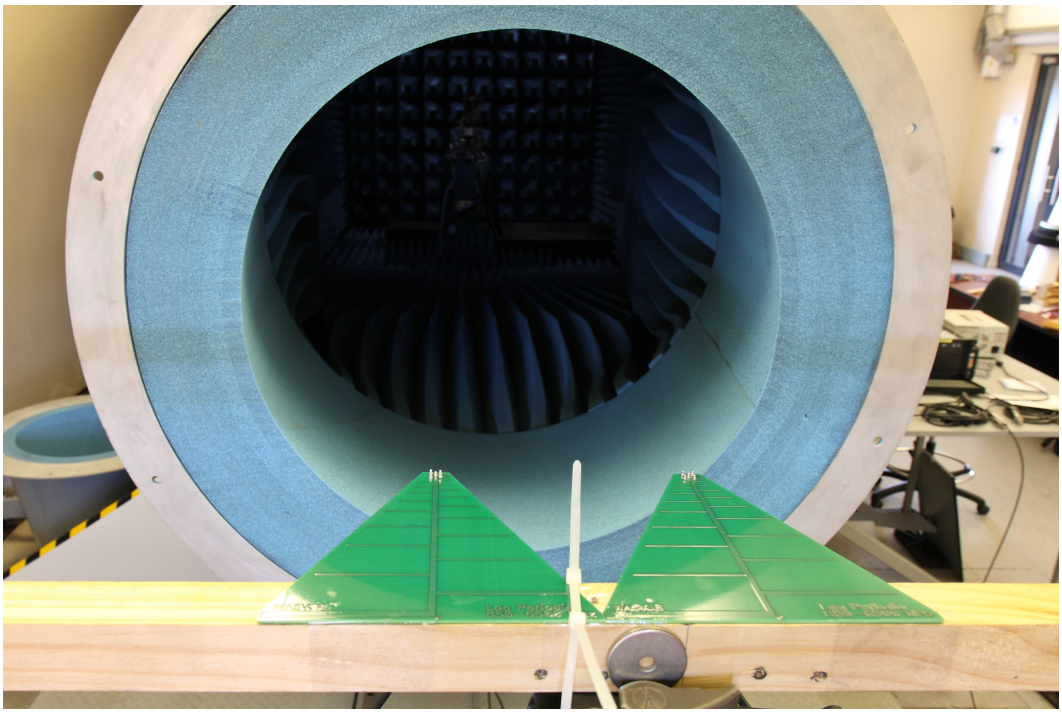

Figure 5.8. Photograph of the radar antennas at the opening of the tapered end of the anechoic chamber. (Photo credit: Prof. W. P. du Plessis)

5.3.1 Monopulse radar

The radar was calibrated by recording the complex samples of each of the two channels for five consecutive measurement iterations. The magnitudes of the samples were calculated and used to determine the mean magnitude factor between the channels. This process was done as

$$A = \frac{1}{N}\sum_{n=1}^{N}\frac{|p_n|}{|q_n|}\,, \tag{5.1}$$

where A was the mean magnitude factor, N was the number of measurement iterations ($N = 5$ in this case), and q_n and p_n were the measured complex samples for channels 1 and 2, respectively. Similarly, the mean phase difference between the channels were calculated as

$$\Psi = \frac{1}{N}\sum_{n=1}^{N}(\beta_n - \alpha_n)\,, \tag{5.2}$$

where N was still the number of measurement iterations, Ψ was the mean phase difference, and β_n and α_n were the measured phase differences for the n^{th} measurement iteration. The mean magnitude factor and phase difference were then used to create a vector where the first element was 1 and the second element was complex number with the mean magnitude factor and phase difference. This vector was

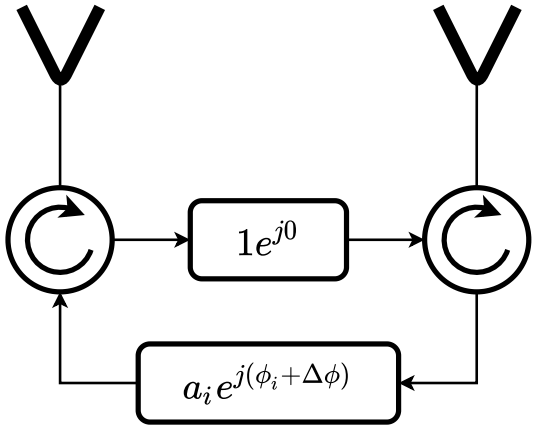

Figure 5.9. An illustration of the repeater paths during the calibration of the phase difference.

used to calibrate the received signals by using element-wise multiplication as

$$\begin{bmatrix} y_1 & y_2 \end{bmatrix} = \begin{bmatrix} x_1 & x_2 \end{bmatrix} \cdot \begin{bmatrix} Ae^{j\Psi} & 1 \end{bmatrix} , \tag{5.3}$$

where y_1 and y_2 represent the output of the calibrated values of channels 1 and 2, respectively, while x_1 and x_2 represent the recorded samples of channel 1 and 2 after pulse compression, respectively.

5.3.2 Cross-eye jammer

The cross-eye jammer was calibrated to achieve values near the ideal values ($a = 1$ and $\phi = 180°$) between the retrodirective paths. This was done by exploiting the fact that a monopulse radar was available and that the effect of the ideal cross-eye parameters on the monopulse antenna patterns was known. As the values of the amplitude factor and phase difference between the cross-eye paths converge to the ideal values, the sum-channel antenna pattern of the monopulse radar minimises due to the cancelling of the received signals [9].

The first part of the calibration was to obtain a phase difference between the jammer paths that converges to 180°. The process that was followed is graphically represented in Figure 5.9. In this figure, a_i and ϕ_i represents the unknown initial magnitude factor and phase difference between the jammer paths, respectively. For simplicity, the top path was used as a reference with a unity magnitude and phase of 0°, while the bottom path presented the parameters relative to that in the top path.

Initially, the radar code was run without applying any changes to the phase and noting the magnitude of the sum-channel return. The code was then run again, but after adding a certain value to the phase

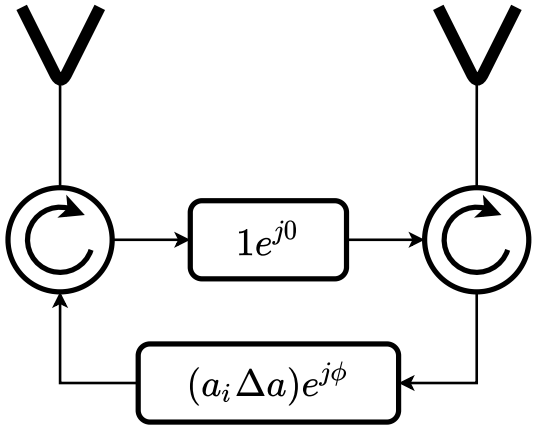

Figure 5.10. An illustration of the repeater paths during the calibration of the amplitude factor.

of the second path, presented as $\Delta\phi$ in Figure 5.9, and noting the magnitude sum-channel return again. This process was done coarsely for different values of $\Delta\phi$ in increments of 10°, until a local minimum was noticed in the sum-channel magnitude. The value of $\Delta\phi$ was then reduced by 10°, and the process was continued, but by changing the value of $\Delta\phi$ in increments of 1° until a new local minimum was perceived. The new phase difference between the jammer paths, given by

$$\phi = \phi_i + \Delta\phi \ , \tag{5.4}$$

was now estimated to be close to the ideal value of 180°.

The second part of the calibration was to calibrate the magnitude factor between the jammer paths so that is near-equal to unity, which is the ideal value for a cross-eye jammer ($a = 1$) [10], [11], [13]. With the desired phase difference obtained, a similar approach was followed to calibrate the magnitude factor. The process that was followed is graphically illustrated in Figure 5.10. The initial amplitude factor, a_i, was adjusted by multiplying it with an adjustment factor, Δa, which was chosen to be 1.5 to start with. This factor was then reduced in increments of 0.1 until a localised minimum value of the magnitude of the sum-channel return was observed. The value was then incremented by 0.1. The process was repeated, but the adjustment was decreased in increments of 0.01 until a localised minimum of the magnitude of the sum-channel return was perceived. The new amplitude factor, given by

$$a = a_i \Delta a \ , \tag{5.5}$$

was now estimated to be close to the ideal amplitude factor of 1.

Table 5.1. Different modes of internal configuration of the repeater.

Mode	Path 1	Path 2	Ideal ϕ	Ideal a
1	Enabled	Enabled	0°	1
2	Enabled	Enabled	180°	1
3	Enabled	Disabled	N/A	N/A
4	Disabled	Enabled	N/A	N/A

However, even with the jammer producing maximum cancellation of the sum-channel, it could not be assumed that the phase difference and amplitude factor was within the ranges $179° < \phi < 181°$ and $0.9 < a < 1.1$, as would be suggested by the increments used in the calibration. The reason was that the SDRs used for both the radar and jammer could not be confirmed to be perfectly coherent and that a minor phase drift between the channels could still occur, as with all practical devices. Another practical limitation could be the presence of noise, which all real-world electronic systems are subject to. It could only be estimated that the phase difference and amplitude factor were close enough to the ideal values to produce a cross-eye effect, and experimental validation was the only way to quantify this effect.

5.4 EXPERIMENTS

The experiments that were conducted can be placed into two categories. The first would be for the case where the jammer was at the opening of the tapered end of the anechoic chamber, with the radar antennas on the positioner, as illustrated in Figure 5.1. The second case would be for the case where the jammer antennas were on the positioner, as illustrated in Figure 5.2. However, even with the two overall experimental layouts that were used, different internal system configurations were used to gather data about different system attributes.

It is important to note that all of the experiments that used the same experimental setup were executed consecutively, without altering the setup in any way – except for resetting the angle of the positioner.

5.4.1 Modes

For measurements after the initial calibration, the internal configuration of the jammer could be divided into four modes. These modes are given in Table 5.1. The first mode is for the case where both jammer

Table 5.2. Definitions of the variables used in the experimental procedure in Figure 5.11.

Variable	Definition
θ_a	The angular position of the positioner at any given time instance.
θ_{start}	The first angular position of the positioner during the experiment.
θ_{stop}	The last angular position of the positioner during the experiment.
$\Delta\theta$	The increment to the positioner angle.
N_m	The number of measurements at each positioner angle.
i	The current measurement iteration for the positioner at a given angle

paths are enabled, and the amplitude factor is 1, while there is no phase difference between the paths. In this configuration, the jammer is effectively a two-channel beacon that is retrodirective due to paths having the same phase delay. Mode 1 can be referred to as the beacon mode.

The second mode is for the retrodirective cross-eye jammer and can be referred to as the jammer mode. Both paths are enabled, and the calibrated parameters are applied to ensure an amplitude factor close to 1 and a phase difference close to 180°. The third and fourth modes are closely related to one another. One path is disabled (multiplied by zero) in each case, while the other is enabled. The difference between the two modes was in which repeater path was enabled and which path was disabled. Modes 3 and 4 can be referred to as the isolated path modes.

5.4.2 General experimental procedure

A single experimental procedure was used for all experiments in the study, and the experiments differed by using multiple variations of internal repeater configurations and experimental setups. The procedure is demonstrated as a flow diagram in Figure 5.11, due to its repetitive nature. The definitions of the variables that were used are summarised in Table 5.2.

The procedure was commenced by setting the parameters for the experiment. As it was decided to rotate the positioner from $-15°$ to 15°, while making measurements at each 1°, the variables were set as $\theta_{\text{start}} = -15°$, $\theta_{\text{stop}} = 15°$, and $\Delta\theta = 1°$. It was also decided to record five measurements at each positioner angle, therefore $N_m = 5$.

The procedures continued by rotating the positioner to the starting position. The radar script is then run

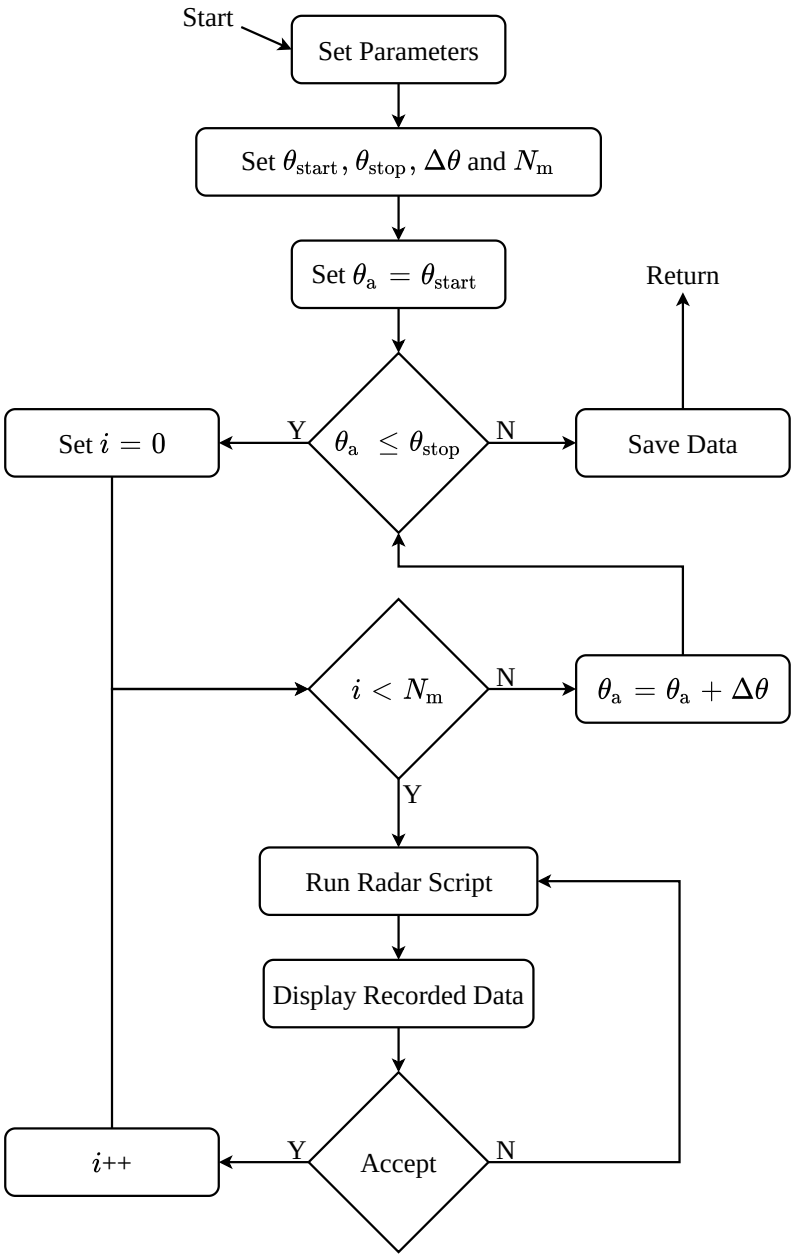

Figure 5.11. A flow diagram demonstrating the experimental procedure that was used in all of the experiments.

multiple times while the recorded data is viewed after each measurement to ensure that no unexpected feedback or errors caused by the device were present. If any measurement was compromised, it was retaken. This process was repeated until five valid measurements were taken.

The positioner was then rotated by incrementing its angle by 1°, after which the same measurement procedure was followed. This was repeated for all positioner angles until the last measurements were made at the stop angle of 15°. The data was then stored to be processed later.

5.4.3 Radar rotation

Experiment 1

Goal: The purpose of the experiment was to test and characterise the monopulse radar for multiple radar rotations by using isolated repeater paths. The data obtained could be used to validate the results from the two-repeater radar experiment to follow and provide extra data to calibrate the results for deviations of the true experimental setup from the ideal.

Setup: The setup used for this experiment was that of the radar rotation setup, given in Figure 5.1. The internal configuration of the repeater device was first set to Mode 3, in Table 5.1, after which it was changed to Mode 4, in the same table.

Procedure: The procedure, given in Figure 5.11 was first followed for the repeater on Mode 3, after which the repeater configuration was changed to Mode 4, before following the same procedure again. Effectively, the procedure was followed separately for the two respective isolated repeater paths. As a result, the output of this experiment comprised of two sets of data.

Experiment 2

Goal: The purpose of this experiment was to test and characterise the monopulse radar for a two-path repeater. The data from this experiment could prove the full functionality of the monopulse radar and calibrate the jammer results for deviations in the setup from the ideal setup. The main outcome of the experiment would be to prove that the monopulse radar operates sufficiently to be used as a testing platform against angular-deception jammers.

Setup: The setup for radar rotation measurements, as shown in Figure 5.1, was used again. The repeater was configured to operate as a beacon with two active repeater paths and no phase difference between the paths. This corresponded to Mode 1 in Table 5.1.

Procedure: With the system set up and configured correctly, the radar antennas were rotated on the positioner, and the measurements were recorded by using the procedure that was illustrated in Figure 5.11.

Experiment 3

Goal: The purpose of this experiment was to execute a working cross-eye jammer and prove that the jammer induces angular errors on the monopulse radar for each rotation of the radar within a given angular range. The results from this experiment could also quantify the effectiveness of the cross-eye jammer and validate previous cross-eye jamming analyses. Lastly, the experiment was also used to determine whether any unexpected anomalies that were not predicted by the theory occur in a practical system.

Setup: As with the first two experiments, the experimental setup was that of the radar antennas being rotated by the positioner, as illustrated in Figure 5.11. The internal configuration of the repeater was that of a cross-eye jammer, with the magnitude factor between the repeater paths being near unity and with the phase difference between the paths converging to 180°. This is indicated as Mode 2 in Table 5.1. Note that the jammer parameters could be changed in this experiment as needed.

Procedure: The radar antennas were rotated to multiple angles by using the positioner, where multiple results of the effect of the jammer on the radar were recorded. As with the other experiments, the general procedure, illustrated in Figure 5.11, was used to take the measurements. The procedure was also repeated for adjusted values of the jammer parameters, a and ϕ.

5.4.4 Jammer rotation

Experiment 4

Goal: The purpose of this experiment was to test and prove the retrodirectivity of the repeater. The experiment was created to prove that the phase delay through the two repeater paths was near-equal

and that the repeater paths were coherent. The data from this experiment could also be used to calibrate the results for the jammer on the positioner.

Setup: The system was set up as illustrated in Figure 5.2, with the jammer antennas being rotated by the positioner. The internal configuration of the repeater was set to Mode 1. Both paths were enabled, with an amplitude factor of unity and no phase difference between the paths, as indicated in Table 5.1.

Procedure: The repeater antennas were rotated, while recording the measurements by using the general procedure, as illustrated in Figure 5.11. Even though the experimental setup changed, the measurements from the radar were still the primary interest, as it could give insight into the functionality of the repeater.

Experiment 5

Goal: The purpose of this experiment was to test whether the cross-eye jammer was, in fact, retrodirective. As a cross-eye jammer can be granted useless if it is not retrodirective, the experiment was to determine whether the jammer performance decays when the orientation of the radar, relative to broadside of the jammer changes. The orientation was changed by keeping the radar static and rotating the jammer.

Setup: The jammer antennas were placed on the positioner, with the radar antennas at the opening of the tapered anechoic chamber, as indicated in Figure 5.2. The repeater was configured to operate in Mode 3 from Table 5.1, where the repeater paths were calibrated and set to have an amplitude factor very close to unity, with a phase difference of almost 180°, which are the ideal parameters for a cross-eye jammer [9].

Procedure: The jammer antennas were rotated, while the results were recorded by using the radar. This was done by using the same experimental procedure as illustrated in Figure 5.11.

Experiment 6

Goal: The experiment was done to obtain monopulse data for the two isolated repeater paths for the case where the repeater antennas were on the positioner. The primary purpose was to gather extra data that could be used to calibrate the jammer-rotation results for deviations of the practical experimental

setup from the ideal setup. Measurements of the individual paths, with the repeater antennas being rotated, could give information on the location of the individual antennas for different positioner angles.

Setup: The repeater antennas were rotated by the positioner by using the setup in Figure 5.2. The repeater was first configured to operate at Mode 3, after which it was configured to operate at Mode 4, with the modes being explained in Table 5.1.

Procedure: The procedure in Figure 5.11 was followed to record data for each of the individual repeater paths, with the repeater antennas being rotated. The output was two sets of data, each for a repeater path.

5.4.5 A summary of measured data sets

It is needed to take account of the data sets produced by the experiments to better understand the post-measurement calibration procedures and keep track when considering the results.

The described experiments were done by using one of two setups. The first setup was with the radar antennas mounted on the positioner as shown in Figure 5.1. The second setup was with the repeater antennas mounted on the positioner as illustrated in Figure 5.2. Three experiments were conducted by using each setup. Given that one experiment from each setup resulted in two data sets, the experiments were done by using each setup resulted in four sets of data as output. The data sets are summarised in Table 5.3.

5.5 POST-MEASUREMENT CALIBRATION

5.5.1 Setup discrepancies

Even though it was desired to use practical setups that match the model from which the extended analysis was derived (as shown in Figure 3.5), practical limitations resulted in deviations from the ideal setup. One example was the brackets that were available for mounting the antennas onto the positioner. An illustration of the actual mounting of the antennas onto the positioner is given in Figure 5.12. This diagram is applicable for both the setup where the radar antennas were placed on the positioner, and the repeater antennas were placed on the positioner. Although the setups differed in antenna spacing, the same deviations occurred in both setups. In Figure 5.12, the antennas are indicated by A and

Table 5.3. A summary of the data sets for each experimental setup.

Setup	Experiment	Data Output
	1	Beacon
Radar	2	Isolated Channel 1
rotation	2	Isolated Channel 2
	3	Jammer
	4	Beacon
Repeater	5	Jammer
rotation	6	Isolated Channel 1
	6	Isolated Channel 2

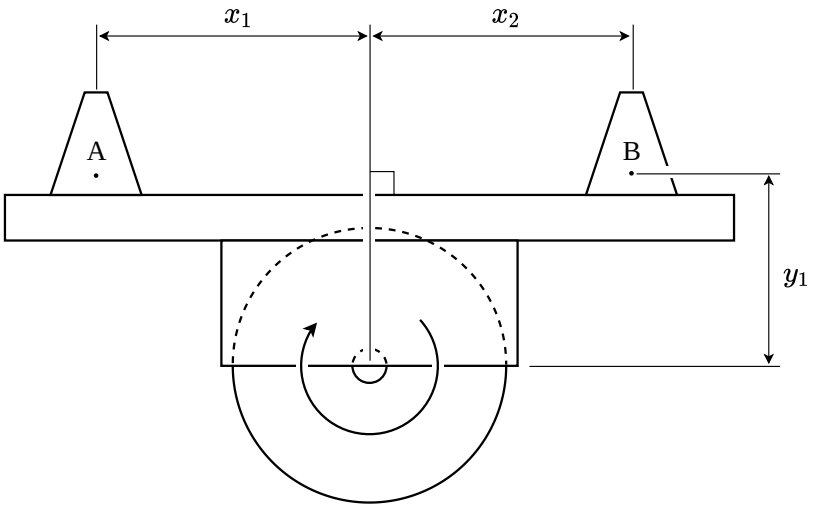

Figure 5.12. An illustration of the practical setup that was used for both the radar and jammer rotation measurements, as seen from the top.

B, with dots indicating the unknown position in the antenna where a 3 GHz signal would resonate. The circle indicates the positioner, and the rectangle overlapping with the positioner indicates the mounting bracket used. Lastly, the longer rectangle indicates a wooden beam that was used to mount the antennas. The beam was attached to the mounting bracket.

By considering Figure 5.12, the ideal case would be that there is no offset between the radiation centres of the antennas and the centre of rotation of the positioner so that $y_1 = 0\ m$. Furthermore, ideally, the antennas would be spaced equally around the rotation centre of the positioner so that $x_1 = x_2$. However,

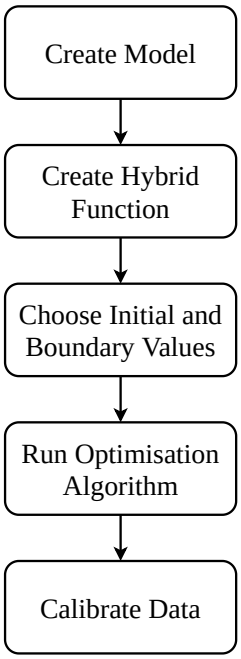

Figure 5.13. A flow diagram of the general post-measurement calibration procedure.

due to the limitation in available mounting equipment and the lack of highly accurate measurement equipment, this was not the case in reality. Even though the deviations were believed to be small, it was still argued that these deviations had to be compensated for in the results.

5.5.2 Calibration approach

The general approach that was used to compensate for the deviations of the practical setup from the theoretical is illustrated in the flow diagram in Figure 5.13. The approach was used for both experimental setups and was implemented in collaboration with the postgraduate supervisor [42].

The first step was to model the practical setup in terms of its deviations from the ideal setup. The deviations were expressed as variables. These variables were used to express the theoretical monopulse ratios and the measured results in terms of the deviations, resulting in adapted monopulse ratio functions of the experimental data. The theoretical and adapted practical monopulse functions were used to create an error function. Initial values and boundary values were chosen for all of the deviation variables, and these values, along with the error function, were used as the input to an optimisation algorithm.

The algorithm was used to determine the actual values of the parameters that resulted in the error function converging to zero. The resultant parameters were then used as the inputs to the error

function. The calculations that were initially used to determine the theoretical monopulse ratios for the optimisation were now used to determine the monopulse ratios for the given optimised parameters. Lastly, with the optimised parameters as inputs, the same error function was used to correct the measured results for the setup deviations and to calculate the new theoretical and practical monopulse ratios for each data set.

It was decided not to implement an optimisation algorithm but rather to use an optimisation function in GNU Octave 6.2.0, as Octave was used to process the data. It was decided to use the sequential quadratic programming (SQP) function, as non-linear data as the input.

5.5.3 Radar rotation calibration model

The practical setup was modelled by considering all the possible deviations that could have occurred during the practical setup for the radar rotation experiments and comparing the deviations to the ideal setup. The result is illustrated in Figure 5.14.

By considering the illustration of the general setup in Figure 5.12, it could be assumed that the centre point of the radar antennas was not the same as that of the positioner and that rotation from the positioner would slightly change the radar centre.

This new radar centre resulted in the line between the radar and repeater centres shifting slightly for each rotation and caused some of the important parameters of the cross-eye model to change. These parameters include the true range between the radar and the jammer (r), the rotation of the radar (θ_r), the rotation of the jammer (θ_c), the distance between the radar antennas (d_r), and half the angular separation of the jammer antennas as viewed from the centre of the radar (θ_e).

As part of the model, specific parameters could not be indicated graphically as they were internal to the system. Two of these parameters include the phase difference and magnitude factor between the radar parameters. Even though the radar channels were calibrated during the measurement process, optimisation could still be used to detect very subtle magnitude and phase differences between the channels that could still be present. The phase difference and magnitude factor between the repeater channels were also included in the model, as they were needed to calculate the theoretical monopulse ratios.

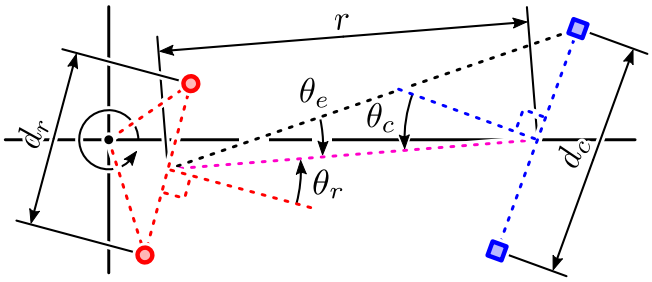

(a)

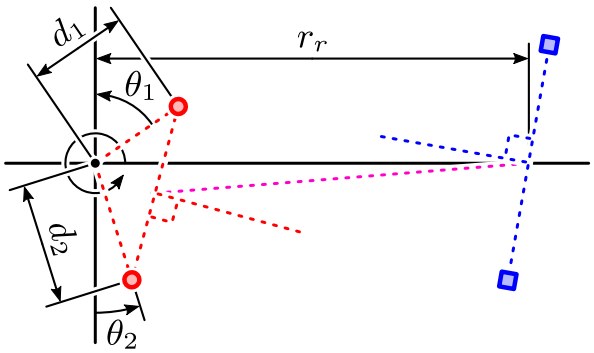

(b)

Figure 5.14. An illustration of the models that were used to calibrate the results for the measurements with the radar antennas on the positioner. Both (a) and (b) indicate different variables for the same model. Adapted from [20], © 2015 IEEE.

The parameters in Figure 5.14 and those inherent to the system that was to be used in the optimisation process are summarised in Table 5.4.

5.5.4 Repeater rotation calibration model

As with the first setup, the results obtained from the experiments where the repeater antennas were rotated also needed calibration due to setup discrepancies. The practical setup for this case was modelled and can be seen in Figure 5.15. From this figure, it is clear that unequal spacing on the positioner could have shifted the centre of the repeater. Therefore, some parameters used in the extended cross-eye jamming analysis, such as the radar and jammer rotations, spacing of the jammer antennas, and distance between the radar and jammer, had to be adjusted.

As with the first setup, some parameters could not be indicated graphically as they were inherent to the system. These parameters included the magnitude factor and phase difference between the radar

Table 5.4. A summary of the parameters that were to be used in the optimisation process for the radar rotation setup, and a definition of each.

Parameter	Definition
d_1	Distance from the positioner's rotation center to the first radar antenna.
d_2	Distance from the positioner's rotation center to the second radar antenna.
θ_1	Angle between the first radar antenna and the line of ideal mounting position for the case of no radar rotation.
θ_2	Angle between the second radar antenna and the line of ideal mounting position for the case of no radar rotation.
r_r	Distance between the rotation center of the positioner and the center of the repeater.
a_r	Amplitude factor between the radar channels.
ϕ_r	Phase difference between the radar channels.
a	Magnitude factor between the repeater channels.
ϕ	Phase difference between the repeater channels.

channels and the magnitude factor and phase difference between the repeater paths. The first two parameters were used in the more refined radar calibration to ensure a deeper null in the difference-channel antenna pattern on broadside. The other two parameters were used to quantify the cross-eye gain when calculating the theoretical monopulse ratios.

All of the parameters that were used to create the error function are defined in Table 5.5. Compared to the list of parameters used in the radar rotation case, the only addition to this table was the base rotation offset of the radar. This was added as it was desired that the centre of the repeater always faced broadside of the radar, and due to the shift in the centre position of the repeater, this was seldom the case. Therefore, corrections had to be made.

5.5.5 Error function

The error function was created by considering all four sets of data for the given setup. For each set of data, the following procedure was followed. Firstly, the theoretical monopulse ratio function was calculated and expressed in terms of the optimisation parameters. The optimisation parameters were then used to adjust the measured data from the two radar channels. The monopulse ratio function for the measured data was then calculated and expressed in terms of the optimisation parameters.

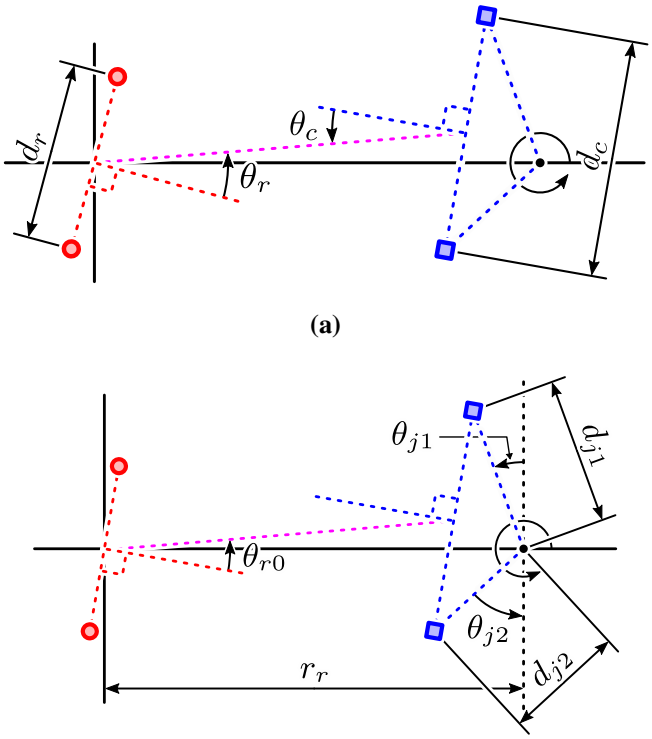

Figure 5.15. An illustration of the models that were used to calibrate the results for the measurements with the repeater antennas on the positioner. Both (a) and (b) indicate different variables for the same model. Adapted from [20], © 2015 IEEE.

An error was formed for each individual set of data by dividing the theoretical monopulse ratio function by the practical monopulse ratio function and subtracting the result from one. The absolute value of this result was then taken to express the errors as positive values. As multiple measurements were made at each positioner angle, the errors were in the form of a two-dimensional matrix. All the values in the matrix were then summed to create a single error value. This process can be described by

$$\varepsilon = \sum_{n=1}^{N} \sum_{m=1}^{M} \left| 1 - \frac{M_{tnm}}{M_{pnm}} \right| \quad , \tag{5.6}$$

where ε was the error function for a given set of measured data, M_{tnm} was the theoretical monopulse ratio for the n^{th} measurement of the m^{th} angle. Similarly, M_{pnm} was the measured monopulse ratio for the n^{th} measurement of the m^{th} angle. The total number of positioner angles and the total number of measurements at each angle are given by M and N, respectively.

Table 5.5. A summary of the parameters that were used in the optimisation process for the radar rotation setup, and a definition of each.

Parameter	Definition
d_{j1}	Distance from the positioner's rotation center to the first repeater antenna.
d_{j2}	Distance from the positioner's rotation center to the second repeater antenna.
θ_{j1}	Angle between the first repeater antenna and the line of ideal mounting position for the case of no repeater rotation.
θ_{j2}	Angle between the second repeater antenna and the line of ideal mounting position for the case of no repeater rotation.
r_r	Distance between the rotation center of the positioner and the center of the radar.
a_r	Amplitude factor between the radar channels.
ϕ_r	Phase difference between the radar channels.
a	Magnitude factor between the repeater channels.
ϕ	Phase difference between the repeater channels.
θ_{ro}	Base rotation of the jammer.

Finally, the output of the error function was the mean of the individual errors for each set of data. This net error can be expressed as

$$\varepsilon_{net} = \frac{1}{4}(\varepsilon_1 + \varepsilon_2 + \varepsilon_3 + \varepsilon_4)\,, \tag{5.7}$$

where ε_1, ε_2, ε_3, and ε_4 were the resulting errors for the four sets of data, and ε_{net} was the final output of the error function.

5.5.6 Calibration

As an extra feature, the error function also returned the monopulse ratio functions when called as a function in Octave, and not used in optimisation. The output of the optimisation function was the values of the parameters that were initially unknown. The adjusted theoretical and practical monopulse ratio functions for each set of data were returned by calling the error function with the optimised parameters. Therefore, the error function was used to optimise the parameters and calibrate the results by using the optimised parameters as inputs.

5.6 CHAPTER SUMMARY

The chapter started with a discussion of the experimental setups used for the radar rotation and repeater rotation experiments. Following this, the whole method used to calibrate the monopulse radar for a null in the difference-channel antenna pattern on broadside was given. This method was applied in the anechoic chamber before the experiments were conducted. The jammer was also calibrated in the anechoic chamber before the experiments. This was done by adjusting the amplitude and phase of one of the jammer paths and considering the sum-channel antenna pattern of the radar. A minimum in the magnitude of the sum-channel suggested that the jammer paths were near-equal in magnitude while having a phase difference of almost 180° between the retrodirective paths. The procedures that were used in the experiments were then described. For both the radar and jammer rotation results, the antennas of the system to be rotated were mounted onto a positioner. The angle of the positioner was then changed to certain values, at which multiple measurements were taken with the radar. The chapter concluded by describing the post-measurement calibration process. Here, SQP was used to find the optimal values of the setup parameters of the system. The parameters were used to correct the experimental setup discrepancies and calculate the theoretical monopulse ratios.

CHAPTER 6 RESULTS AND DISCUSSION

6.1 CHAPTER OVERVIEW

In Chapter 5, the calibration and experimental procedures that were used to obtain the results were discussed. In this chapter, the results from these experiments are presented and discussed in detail. Included are the results for both cases where the radar antennas and the repeater antennas were rotated on a positioner. The anomalies in the results are also identified and discussed.

6.2 MONOPULSE RADAR

The sum-channel antenna pattern for the monopulse radar before the post-measurement calibration process was obtained by adding the radar return from the received channels by using the data from experiment 1. The resultant plot is shown in Figure 6.1, where the five sets indicate the traces that were obtained by taking five measurements at each radar rotation. The median of the five traces is also shown. It was decided to use the median instead of the mean to eliminate outliers in the noisy data. As only five measurements were made at each angle, a small number of measurements that deviated significantly due to measurement errors occurred. By using the median of the five measurements instead of the mean, the effect of such measurements on the overall results were reduced. One example of such a measurement is that of set 3 in Figure 6.1 at a radar rotation of 0°. It can be seen that this measurement differed significantly from the other four measurements at the specific radar rotation. It can be seen that much noise is present in each trace, even though pulse compression was used. This is likely due to the low SNR that was caused by the low transmission power of the radar. However, even with the presence of noise, it can be seen that the data in Figure 6.1 is that of the sum-channel antenna pattern of the radar [4].

The measured difference-channel antenna pattern of the radar, as obtained through experiment 1, is

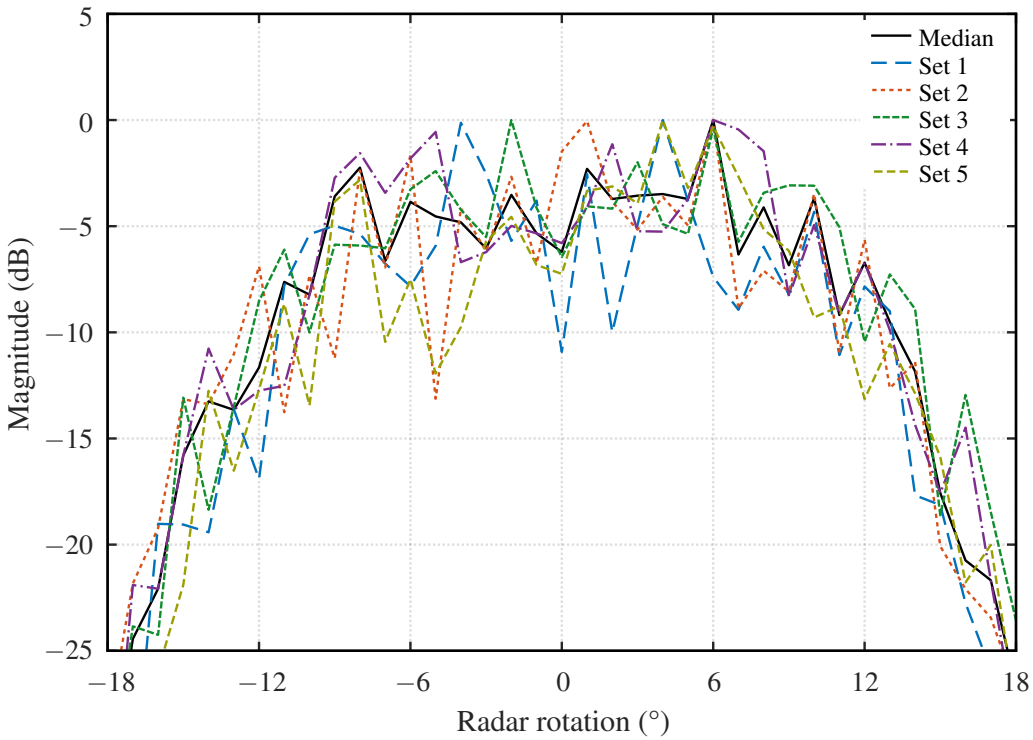

Figure 6.1. Plot of the sum-channel antenna pattern before post-measurement calibration.

given in Figure 6.2. Similarly to the sum-channel antenna pattern, the difference-channel antenna pattern was obtained by subtracting the radar returns in the presence of a beacon. This subtraction was done after pulse compression, but the low transmission power of the radar resulted in a low SNR. The low SNR is what led to the abundance of noise in the pattern. The median of the difference-channel antenna pattern is also shown in Figure 6.2, and shows a null of less than −15 dB at broadside.

The monopulse ratio of the radar is shown in Figure 6.3. The monopulse ratio was plotted by dividing the difference- by the sum-channel returns and taking the imaginary parts of the data. It is surprising to note that the very noisy sum- and difference-channel patterns, as shown in Figure 6.1 and Figure 6.2, resulted in the clean monopulse ratio function. All five data sets converged to a single function and only deviated for radar rotations less than −12° and more than 12°. These deviations are expected, as the sum-channel pattern is more than 15 dB attenuated at these radar rotations. The symmetrical and clean monopulse ratio function, with repeatable data, not only proves that the monopulse radar is a robust platform to test angular deception against but also reinforces the theory that states that a monopulse radar is independent of the power level of the received signal [4], [28].

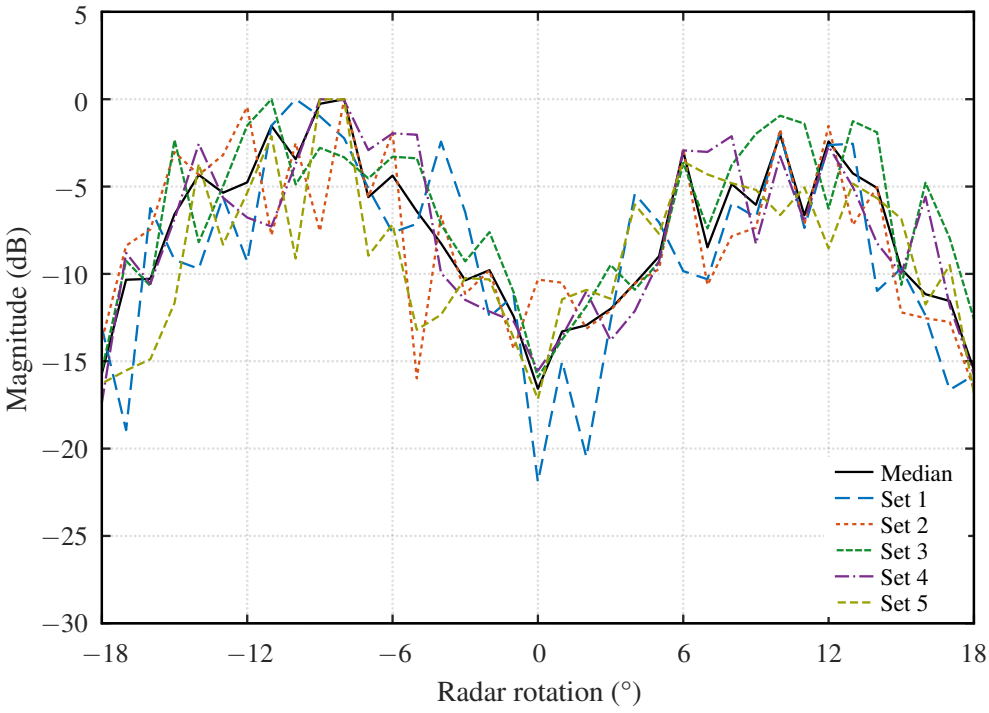

Figure 6.2. Plot of the difference-channel antenna pattern before post-measurement calibration.

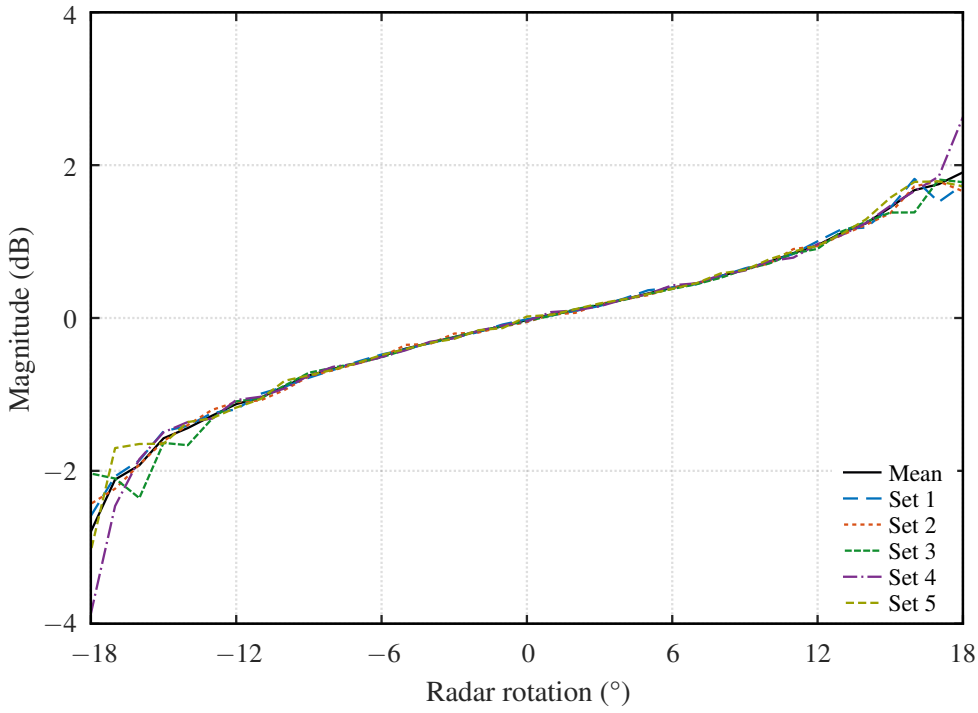

Figure 6.3. Plot of the monopulse ratio before post-measurement calibration. Although it is difficult to distinguish between the plots, this only means that all of the data sets converged to the same function.

Table 6.1. A summary of the parameter output from the optimisation of the radar rotation results.

Parameter	Value
θ_1	32.57°
θ_2	159.63°
d_1	0.053 m
d_2	0.086 m
r_r	6.43 m
d_c	0.324 m
a_r	0.97 dB
ϕ_r	7.25°
a	−1.30 dB
ϕ	175.35°

6.3 RADAR ROTATION EXPERIMENTAL RESULTS

6.3.1 Optimisation parameter output

The parameters that were obtained from the optimisation process, as described in Chapter 5, for the case of the radar antennas being mounted on the positioner, are given in Table 6.1. From this table, it can be seen that the value of the amplitude factor was −1.30 dB (equivalent to $a = 0.861$ on a linear scale), while the phase difference between the repeater paths was 175.35°. Note that these values were only for the repeater in its jammer configuration. The resultant cross-eye gain for these parameters is 10.344, which is a decent cross-eye gain for a practical system [9], [13], [22].

6.3.2 Calibrated results

The results for the monopulse radar against the repeater in a beacon configuration, as set out by experiment 1, can be seen in Figure 6.4. This figure contains the plots for the five measurements of the radar at each radar rotation and the theoretical results. The indicated angle of the radar correlates well with the theoretical, with only some deviation present at radar rotations of more than 7°, but this deviation is less than 2° at worst. The fact that all five data sets are near-equal proves that the radar results are repeatable and that the radar is robust. These results confirm that the monopulse radar was accurate enough to perform as a platform for testing angular deception techniques.

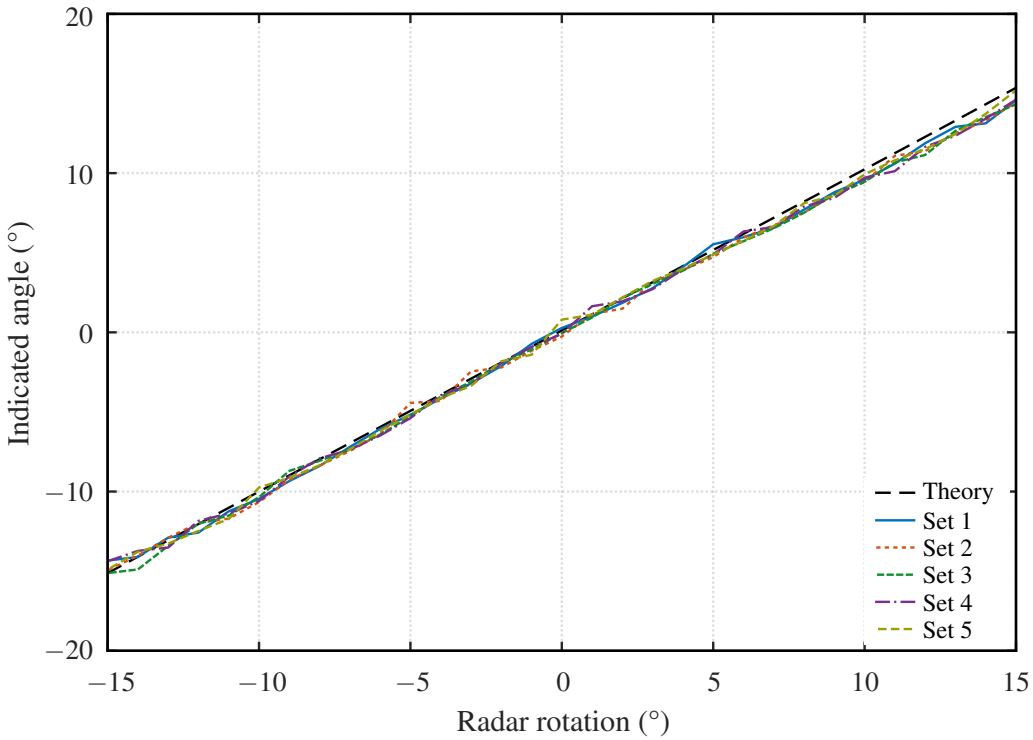

Figure 6.4. Plots of the indicated angle of the radar in the presence of the repeater, configured as a beacon. Although it is difficult to distinguish between the plots, this only means that all of the data sets converged to the same function.

The results for the monopulse radar against the repeater, with the repeater configured for isolated paths, as per experiment 2, are shown in Figure 6.5. The five data sets, corresponding to the results to the five measurements per rotation angle with only the first path of the repeater enabled, can be seen in Figure 6.5(a). In addition, the results for the configuration where only the second path of the repeater was enabled, can be seen in Figure 6.5(b). It is evident that the indicated angle of the radar correlates well with the theoretical results in both cases. In Figure 6.5(a), it can be seen that the indicated angle is slightly more than 0° at broadside. Similarly, the indicated angle is slightly less than 0° at broadside in Figure 6.5(b). This indicates the angular positions of the two repeater antennas, as viewed from the radar relative to the centre of the repeater.

The results for the monopulse radar against the repeater, with the radar antennas on the positioner and the repeater, configured to be a cross-eye jammer, as per experiment 3, are shown in Figure 6.6. Firstly, it can be seen that the radar experienced significant angular errors, especially at negative radar rotations. At broadside of the radar, an angular error of about 10°was experienced, which is reasonably

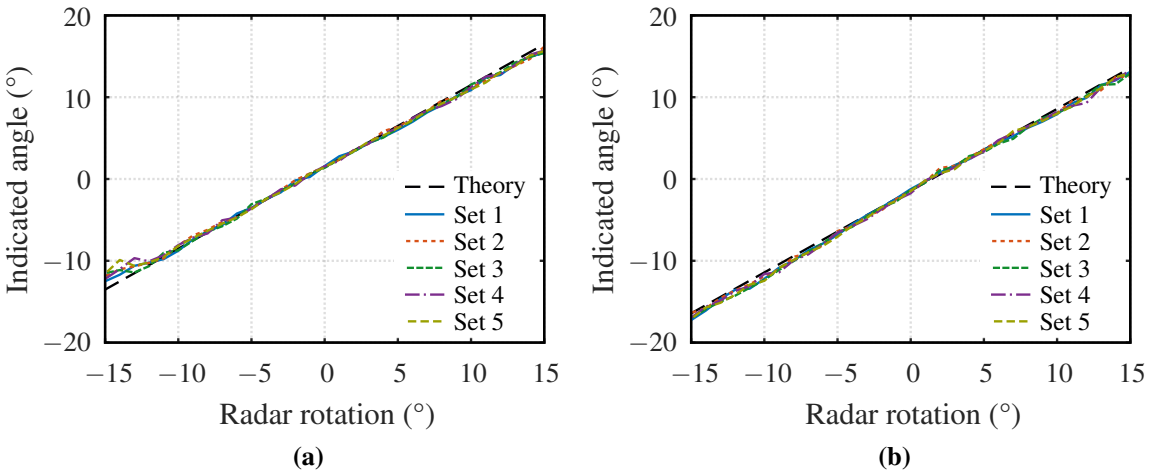

Figure 6.5. Plots of the indicated angle of the monopulse radar against the repeater, with (a) only the first path, and (b) only the second path of the repeater switched on. The indistinguishable plots suggest that all the data sets converge to the theoretical function.

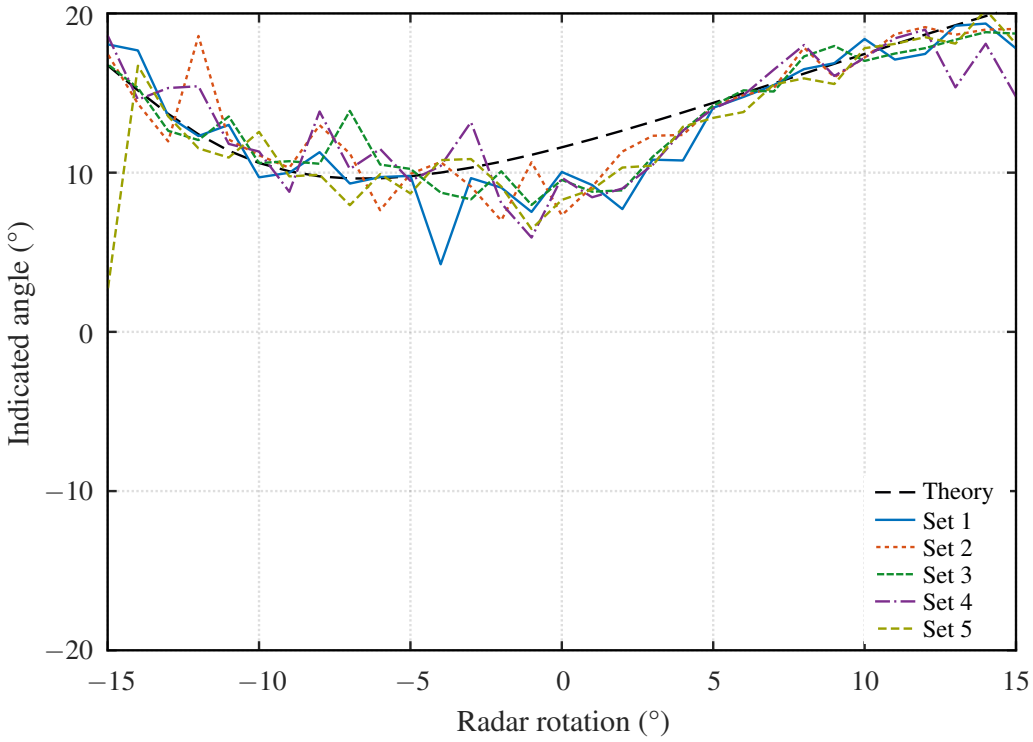

Figure 6.6. Plots of the monopulse radar, with the repeater configured a cross-eye jammer.

large for an angular jammer [9].

The large angular error induced by the jammer suggests that the calibration method, where the known sum-channel magnitude of a monopulse radar was minimised by adjusting the jammer parameters, a and ϕ, until a localised minimum was found, was successful. As the method only calibrates the internal jammer paths, the results suggest that it should be possible to use an available monopulse radar to calibrate a cross-eye jammer, which in return could deceive adversarial radars in angle. The fact that the jammer was implemented by using a bladeRF 2.0 SDR shows that the calibration is possible with cost-effective hardware. The calibration method could also be used to automatically calibrate a cross-eye jammer installed on a platform by installing a cost-effective self-made monopulse radar, as used in this study, alongside it. This could potentially mitigate the risk of the jammer turning into a beacon when the jammer parameters change due to drifting RF hardware [22].

Another noteworthy finding in Figure 6.6 is that the indicated angle of the jammer never becomes 0°, regardless of the radar rotation. By extension, the monopulse ratio is never zero. Considering that a tracking radar tracks a target platform by using the monopulse ratio as the error input to the control system, the results in Figure 6.6 suggest that a tracking radar would break its lock on the target platform [4], [5], [9]. In a real-world scenario, this could mean that a radar-guided missile would never be able to even pursue the target platform [1], [4].

As with the previous results, the five sets of measurements in Figure 6.6 are as a result of the five measurements per radar rotation angle. Even though some of the data seem noisy, all tend to have the same general function. The noise in the data sets can be explained by one of the most fundamental principles of cross-eye jamming – sum-channel cancellation [9]. Because a 180° phase difference is induced between the repeater paths, the return at each radar antenna cancels when calculating the sum-channel. This was certainly the case when considering that this cancellation was used to calibrate the cross-eye jammer for the desired amplitude factor and phase difference between the repeater paths. The monopulse ratio was formed by dividing the difference-channel return by the sum-channel return and taking the imaginary part of the result. If the power level of the sum-channel were low, noise in the radar receiver would have had a substantial effect on the calculated sum-channel and cause noise in the results.

The mean of the jammer results from Figure 6.6, as well as the means of the results from two isolated

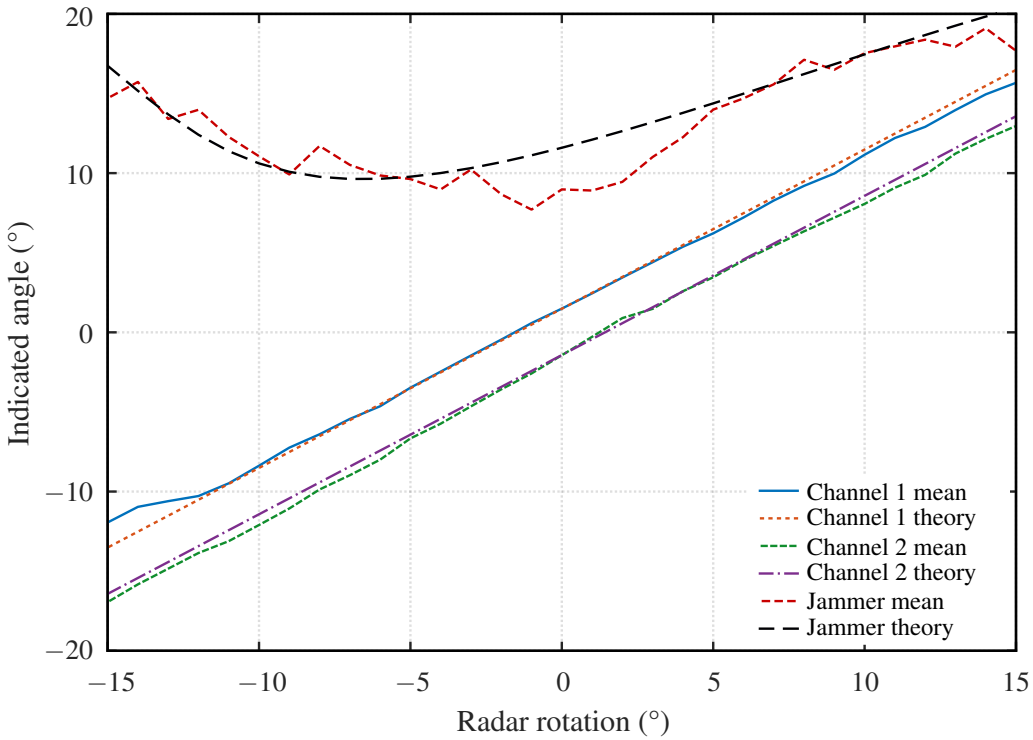

Figure 6.7. Plot of the mean jammer results compared to the results of the isolated repeater paths.

channels, given in Figure 6.5(a) and Figure 6.5(b), are compared in Figure 6.7. As stated before, the radar results against the isolated channels of the repeater indicate the angle to each repeater antenna, as seen from the radar. In a practical cross-eye system on an aircraft, the cross-eye jammer antennas would be installed on the tips of the wings in jammer pods [1], [3]. By comparing the mean of the jammer results to the mean of each of the isolated repeater channel results, it can be seen that the perceived indicated angle, when the jammer is turned on, is much larger than the indicated angle of the first isolated channel, for all rotations of the radar. The indicated angles from the first isolated channel differ less from the jammer than the results from the second channel. This suggests that a false target was created out of the span of the jammer, enforcing the fact that the jammer operated as expected.

It can be seen in Figure 6.6 and Figure 6.7 that there is a significant deviation of the practical jammer results from the theoretical at radar rotations between $-3°$ and $5°$. This anomaly will be discussed later in this chapter.

Table 6.2. A summary of the parameter output from the optimisation of the repeater rotation results.

Parameter	Value
θ_{j1}	20.00°
θ_{j2}	181.25°
d_{j1}	0.308 m
d_{j2}	0.410 m
r_r	5.01 m
d_r	0.135 m
a_r	1.31 dB
ϕ_r	−4.24°
a	−0.28 dB
ϕ	174.02°

6.4 REPEATER ROTATION EXPERIMENTAL RESULTS

6.4.1 Optimisation output

The parameter values that were obtained from the optimisation procedure, for the case of the repeater being rotated on the positioner, are summarised in Table 6.2.

The resultant cross-eye gain from the values, $a = -0.280$ dB and $\phi = 174.02°$, is 5.44, which is almost half of the cross-eye gain for the case of the radar antennas on the positioner. Even though this was the case, the jammer antennas were placed further apart so that half the angular separation of the jammer antennas, θ_e, was much larger, resulting in similar angular errors than in the case with the radar antennas being rotated.

6.4.2 Calibrated results

The results of the radar in the presence of the repeater in the beacon configurations, where the repeater antennas are mounted on the positioner, are shown in Figure 6.8. The five data sets were obtained by rotating the repeater antennas and recording five measurements at each positioner angle. As the repeater centre was a little off broadside due to the experimental setup, the theoretical curve of the indicated angle is a function that is negative for all repeater angles but very close to 0°, as would be expected for results where the radar antennas are stationary. The significance is that the measured

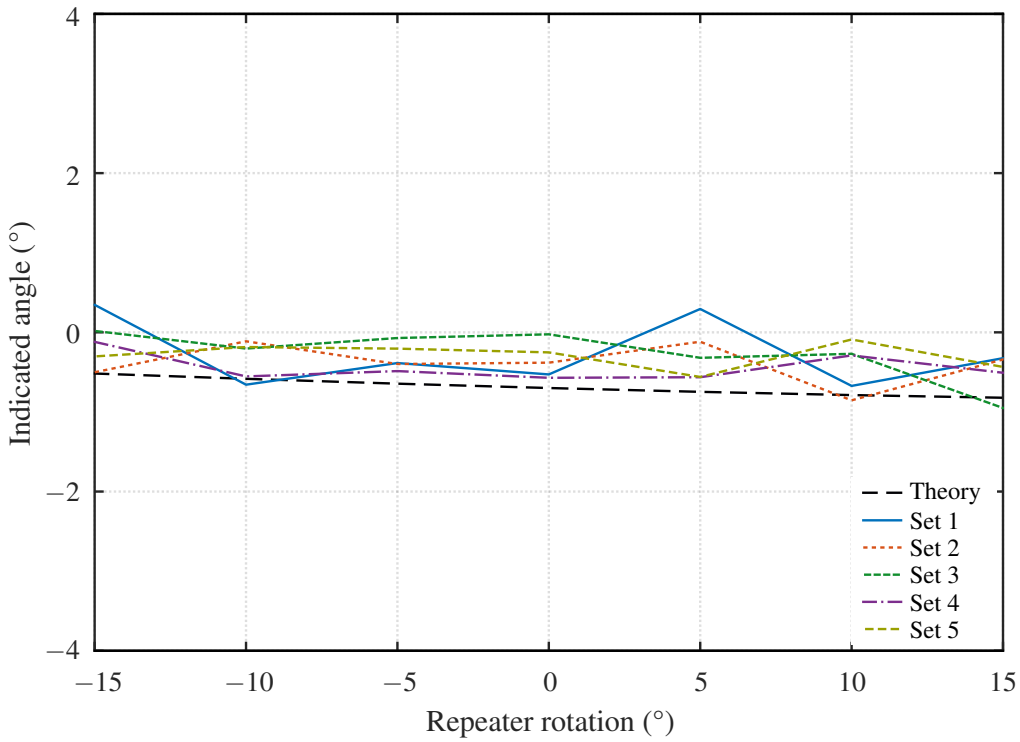

Figure 6.8. Plots of the radar in the presence of a beacon, with the repeater antennas being rotated.

data sets all follow the theoretical function with less than 1° deviation. This means that the radar signal is repeated back to the radar in the direction from which it came, proving that the repeater is retrodirective.

The results where the radar was placed in the presence of the rotating repeater, with only one repeater channel enabled at a time are shown in Figure 6.9(a) and Figure 6.9(b). These results prove the integrity of the results in Figure 6.6, as the indicated angles of the isolated channel results are approximately equally higher and lower than that of the beacon results. This suggests that the indicated angle results in Figure 6.9(a) represent the indicated angle from the centre of the radar to the first repeater antenna, the results in Figure 6.9(b) represent the angle from the centre of the radar to the second repeater antenna, and the results in Figure 6.8 represent the angle from the centre of the radar to the centre of the repeater, all relative to broadside of the radar antennas.

The plots in Figure 6.10 show the indicated angle of the radar in the presence of the repeater. The repeater antennas were placed on the positioner, and the repeater was configured as a cross-eye jammer. As with the results of the jammer with the radar antennas on the positioner, there is noise present in the

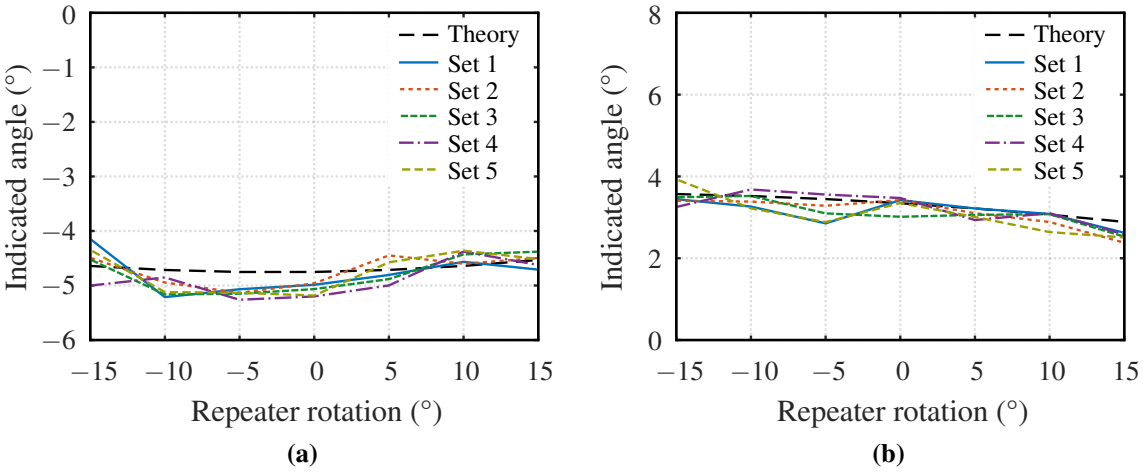

Figure 6.9. Plots of the indicated angle of the monopulse radar against the repeater, with (a) only the first path, and (b) only the second path of the repeater switched on. Here, the repeater antennas were mounted on the positioner.

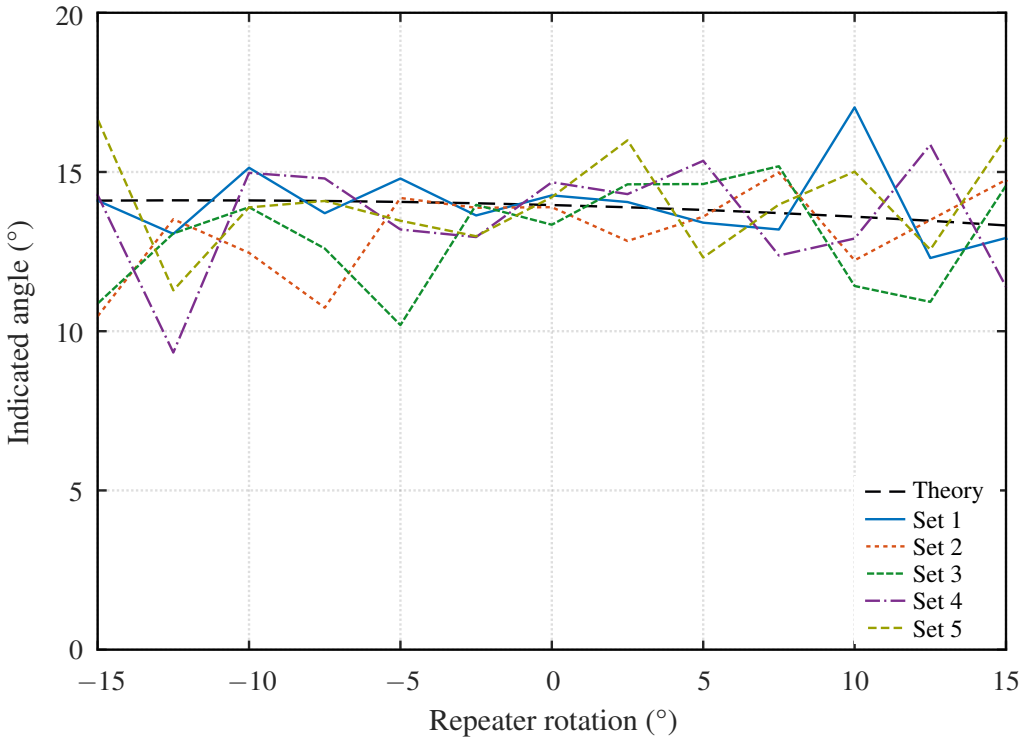

Figure 6.10. Plots of the radar in the presence of the rotating repeater, with the repeater configured as a cross-eye jammer.

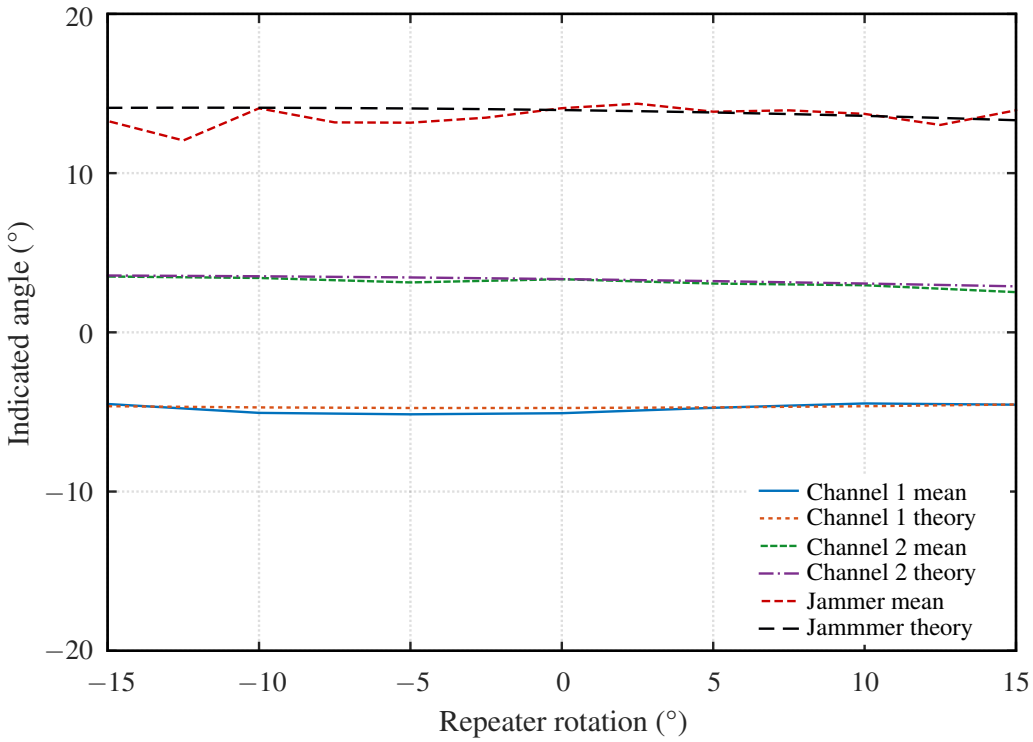

Figure 6.11. Plot of the mean jammer results compared to the isolated channels.

plots. The noise can be explained by the low SNR of the sum-channel return that resulted from the cancelling of the sum-channel returns at the radar. However, all the plots follow the theoretical results, and there are significant angular errors for all rotations of the repeater.

The mean of the results for the cases where only one repeater channel was enabled, as well as the mean of the results for the repeater configured as a jammer, are shown in Figure 6.11. Firstly, it can be seen that the mean of the jammer results are less noisy than the individual plots and has a minor deviation from the theoretical jammer plot. The fact that the jammer induced large angular errors that are very constant at all rotations of the jammer shows that the cross-eye jammer was, in fact, truly-retrodirective. This is a significant result, as no other implementation of cross-eye jamming at the time of this study was truly-retrodirective.

Lastly, as with the case where the radar antennas were placed on the positioner, the two isolated channel results in Figure 6.11 indicate the angle to each of the two jammer antennas relative to broadside of the radar antenna. The antenna closest to the apparent position of the target platform, with the apparent position being induced by the cross-eye jammer, has a mean angular position of less than 5°, where the

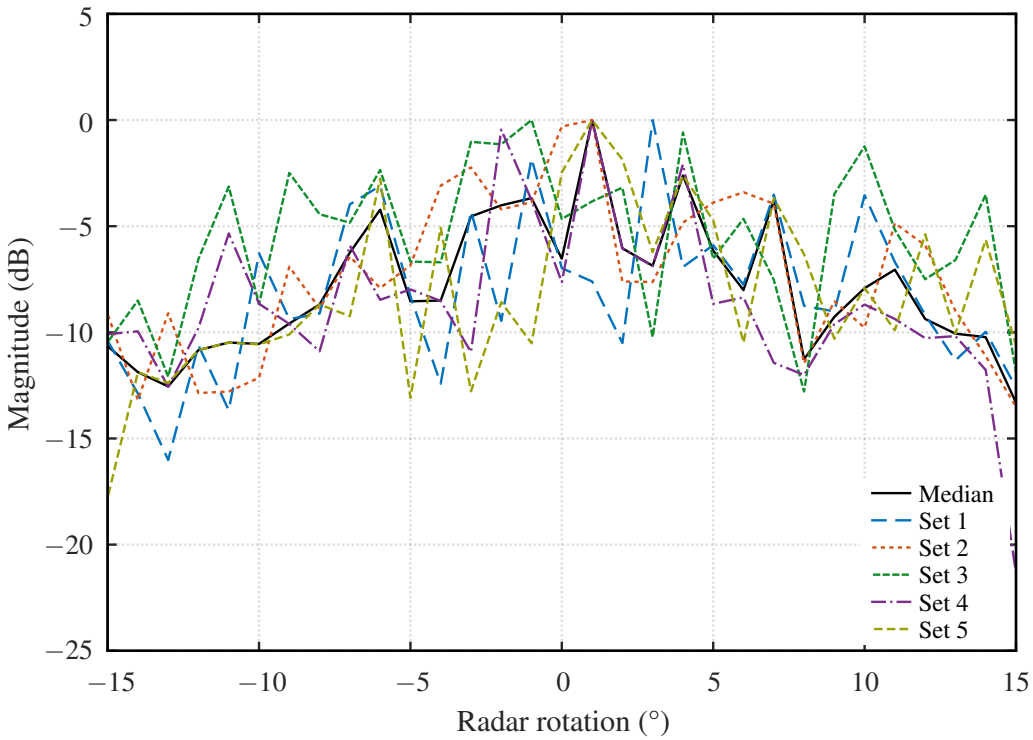

Figure 6.12. Magnitude of the first receive channel of the radar, in the presence of the jammer.

mean apparent angular position of the platform, with the jammer, switched on, is almost 15°. This suggests that the apparent position of the target platform is more than 10° from the closest tip of the jammer, and therefore, far out of the span of the target platform.

6.5 ANOMALIES

There was only one significant deviation in the results. This anomaly could not be corrected, as the experimental setup did not cause it. This anomaly was seen in Figure 6.6, at radar rotations from about −3° to about 5°. It presented itself again in Figure 6.7, and was even more visible here, as the mean of the jammer results removed some of the noise. In both figures, at the given radar rotations, it can be seen that the measured indicated angle for the jammer results is about 3° less than the theoretical indicated angles.

To determine the cause of the anomaly, it was decided to look at the received data of the individual channels of the radar, where the radar was in the presence of the jammer. The data for the first radar receive channel is shown in Figure 6.12, where the data of the second channel is shown in

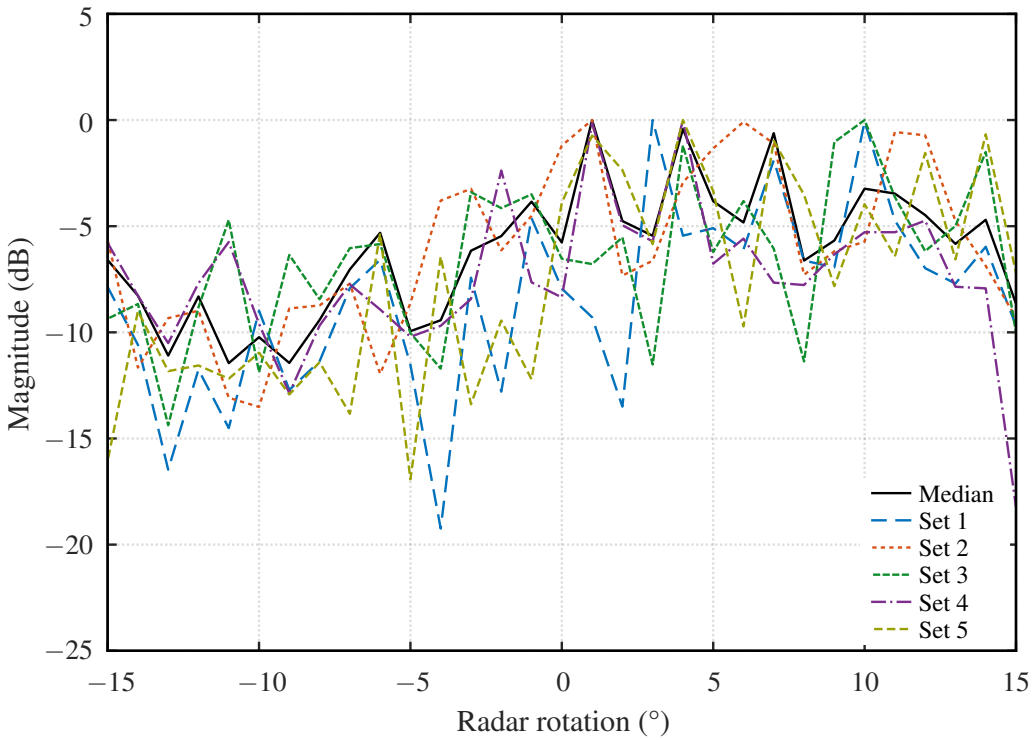

Figure 6.13. Magnitude of the second receive channel of the radar, in the presence of the jammer.

Figure 6.13.

For the first channel, not much could be deduced, as the signal level fluctuated to some extend. The magnitude of the signal was lower for radar rotations less than $-7°$ and more than $7°$, and this could be explained by the tapering off of the antenna patterns. The second channel provided more insight into the problem. It can be seen that the magnitude of the signal was significantly less for rotations between $-15°$and $0°$, than for rotations between $0°$ and $15°$.

To investigate the problem further, the sum-channel antenna pattern for the radar in the presence of the jammer was constructed. The results are shown in Figure 6.14. It can be seen that the pattern is much nosier than the sum-channel antenna pattern for the case of the beacon in Figure 6.1. This was expected as the sum-channel pattern in Figure 6.14 was created by radar returns that cancelled due to the phase difference in the jammer, resulting in a lower SNR. Something to note in Figure 6.14 is that the sum-channel pattern has a peak slightly to the right of radar broadside, and the patterns taper off much faster for positive radar rotations. In other words, the sum-channel pattern is somewhat squinted to the right. This could explain why the largest deviation in indicated angle was slightly to the right of

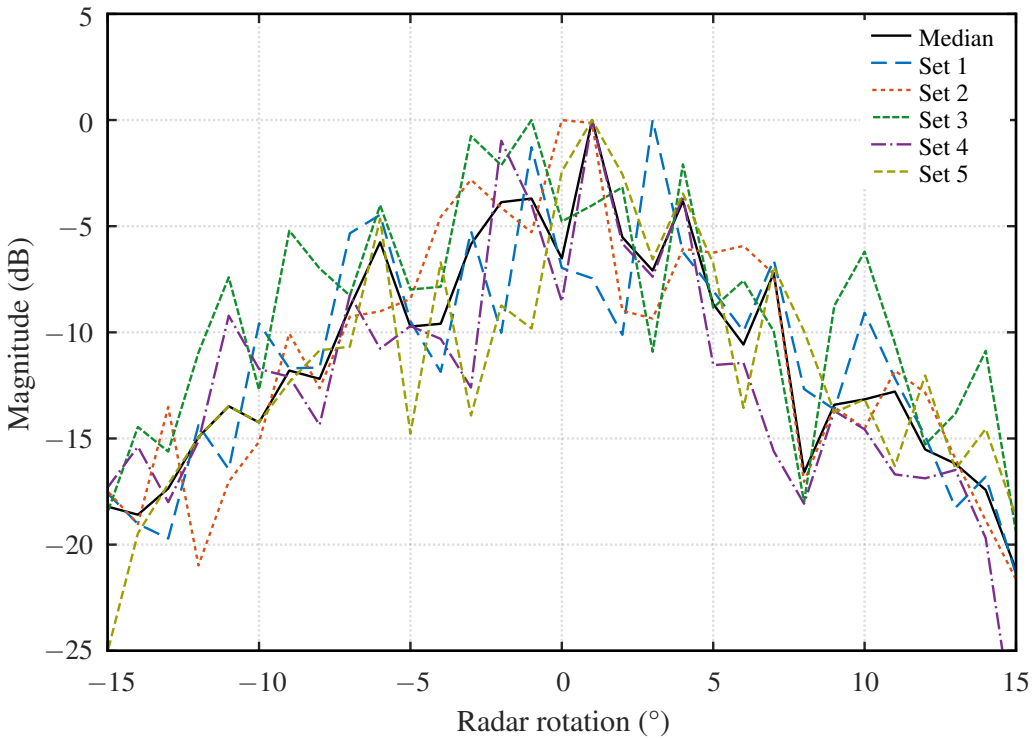

Figure 6.14. Sum-channel antenna pattern of the radar, in the presence of the jammer.

the radar broadside.

A likely explanation for the squint is mutual coupling between the radar antennas, which were placed relatively close to each other [43]. The phenomenon could not be seen in the sum-channel pattern for the case where the radar was tested against the beacon, shown in Figure 6.4. The most likely reason is that the power levels of the received radar returns were much higher for the case of the beacon, where the cancellation of the channel returns due to the enabled jammer resulted in sum-channel returns that had much lower power levels. Therefore, mutual coupling was likely present in all experiments, but the effects were much more visible with the repeater configured as a cross-eye jammer.

Even though mutual coupling did create minor anomalies in the results, the error was on the side of the radar and not the jammer, which performed excellently. Care is taken to either avoid or compensate for mutual coupling between antennas in commercial radar systems [4].

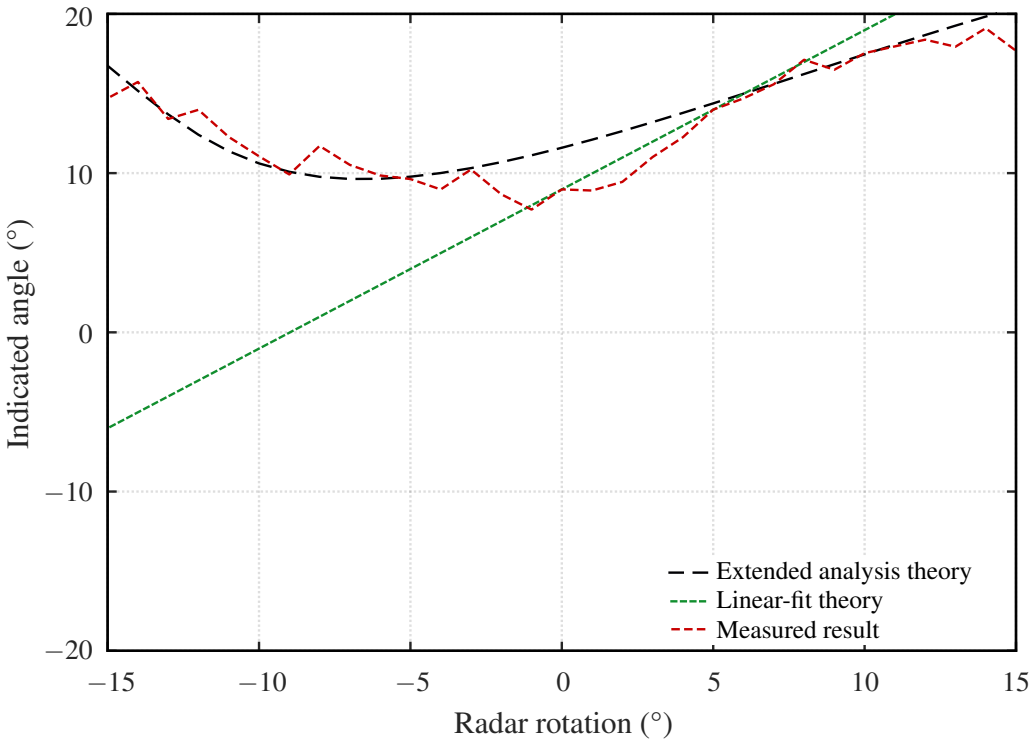

Figure 6.15. A comparison between cross-eye jamming analyses and the measured results.

6.6 CROSS-EYE JAMMING MODELS

An important research contribution of this study was to validate previous cross-eye jamming analyses. Three analyses were identified in Chapter 3, namely the phase-front, linear-fit and extended analysis [9]–[12], [35]. As discussed, the phase-front and linear-fit analyses were considered to be near-identical, as both were glint analyses, and both effectively considered the antenna patterns as linear [10]–[12], [35]. In the extended analysis, linearity was not assumed, and the monopulse antenna patterns were used in their non-linear forms [9], [13]. It was hypothesised that the extended analysis was the best-suited model for a practical cross-eye jammer due to the use of the true monopulse antenna patterns. The extended analysis was also the only analysis in the literature that considered retrodirectivity [9]. A comparison between the extended analysis, linear-fit analysis, and the practical results is shown in Figure 6.15. The linear-fit function was created by using the derived equation of the indicated angle of the linear-fit analysis, given in (3.27) in Chapter 3. The equation can be rewritten as a function of θ_r as

$$\theta_i(\theta_r) = \theta_r + \theta_e G_c \,, \tag{6.1}$$

where θ_i is the indicated angle, θ_r is the rotation of the radar, θ_e is half the angular separation between the jammer antennas, and G_c is the cross-eye gain. From this equation it can be seen that the indicated angle as a function of radar rotation always has a gradient of $1°/1°$. Therefore, the best fit to the results can be obtained by finding the θ_i-intersection of the function, which can be found be setting $\theta_r = 0°$, and solving for the $\theta_e G_c$ term. By using the measured results in Figure 6.7, the value of the indicated angle for no radar rotation was found to be 8.98°, leading to the best fit for the linear-fit cross-eye model to be given by

$$\theta_i(\theta_r) = \theta_r + 8.98° \, . \tag{6.2}$$

The theoretical function of the extended analysis was found by using the optimisation method as described in Chapter 5.

It can be seen in Figure 6.15 that the measured results were in the form of a non-linear function of radar rotation, in contrast to the linear function of the linear-fit analysis. The linear-fit equation does give an acceptable estimation of the results for positive radar rotations, but due to the use of a linear function, it deviates significantly for negative radar rotations. The linear-fit analysis also suggests that the radar will experience an indicated angle of 0°, which is clearly not the case. In contrast to the linear-fit analyses, the extended analyses represent the practical results very well for all rotations of the radar. As discussed, mutual coupling of the radar antennas did cause deviations around broadside, but that was caused by the radar and not the jammer. By considering (3.69), the extended analysis suggests that the angular error induced by a cross-eye jammer is not only a function of the angular separation of the jammer antennas and cross-eye gain but also of the rotation of the radar [9]. This is the case of the measured results, which can be seen to be non-linear.

It is conclusive that neither the linear-fit model nor any other cross-eye jamming model that approximates either the element antenna patterns or the sum- and difference-channel antenna patterns as linear can be used to describe the full effect of a cross-eye jammer on a monopulse radar in practice. In contrast, the practical results suggested that the extended model is a very accurate representation of the effect of a cross-eye jammer.

Finally, the results in Figure 6.10 and Figure 6.11 proved that the practical cross-eye jammer was truly-retrodirective. With the extended model being the only model that considers retrodirectivity, these results enforce the fact the extended model is the best theoretical representation of cross-eye jamming that is available in the literature.

6.7 CHAPTER SUMMARY

The chapter commenced with a section where the monopulse antenna patterns, which were obtained by rotating the radar in the presence of the repeater as a beacon, were presented. It was shown that both the patterns were symmetrical, and although noise was present, both corresponded to the expected sum- and difference-channel patterns. The monopulse ratio functions for the patterns were also shown, and it could be seen that the noise was significantly reduced. It was concluded that the monopulse radar was robust and that it was an excellent platform to test angular deception techniques against.

Following the radar results, the results for the jammer, where the radar antennas were rotated on the positioner, were shown. It could be seen that large angular errors were induced on the radar for all radar rotations. The indicated angle of the radar also never became 0°, resulting in the conclusion that a tracking radar would lose its lock on the platform. It was also concluded that the calibration method of the jammer, where the sum-channel magnitude of an available monopulse radar was minimised by adjusting the jammer parameters, was successful.

The cross-eye gain that was calculated by using the parameters that were estimated by the optimisation algorithm was 10, and suggested that large angular errors could be induced on radar systems by using cost-effective SDRs. The results of the jammer, with the jammer antennas being rotated on the positioner, were also given. It was shown that the repeater was truly-retrodirective in both its beacon and jammer configurations.

Another meaningful result was that the apparent angular position of the platform under protection was always outside of the span of the jammer antennas, and by extension, the true position of the platform – in some cases over 1 m. The practical results followed the theoretical results very well, with the only deviation being present in the results where the radar antennas were rotated in the presence of the jammer. It was found that the most likely cause of the deviation was mutual coupling between the radar antennas and that the deviation was not a reduction in the performance of the jammer itself.

Finally, the results were compared to previous analyses, and it was found that the linear-fit analysis was not a very good model for a practical cross-eye jammer, as it deviated from the measured results at negative radar rotations, where the extended analysis represented the practical cross-eye jamming results well across all angles of rotation. The extended analysis also considered retrodirectivity,

which was an important attribute of a functional cross-eye jammer that was also seen in the practical results.

CHAPTER 7 CONCLUSION

7.1 CONCLUSIONS

Tracking radars pose a grave threat to any military, as it can be used to not only detect a target platform and determine its velocity and range but also lock onto its angular position. Tracking radars are also used as active homing methods in missiles, which in return could cause enormous damage to a target platform and threaten the lives of the crew. Most EA systems can only deceive radar systems in Doppler shift and range, with very few methods that could be used to deceive radar systems in angle.

Cross-eye jamming was identified as one of the most promising active angular deception techniques. Numerous analyses of cross-eye jamming were conducted, with some dating back from the 1950s, but almost all analyses were based on glint analyses. All made the assumption that either the element antenna patterns of a monopulse radar or the sum- and difference-channel antenna patterns were linear – an assumption that is only true on broadside of an angular radar. One analysis did not make linear-fit assumptions but considered the antenna patterns and sum- and difference-channel antenna patterns in their complete forms. The analysis also considered retrodirectivity, which is vital in deception jamming but was omitted by the other analyses. In addition to the analyses, most practical results of cross-eye jamming were either limited to simulation or did not consider retrodirectivity.

A need was identified to produce practical cross-eye jamming results to validate or reject previous analyses. To be complete and consider the entire problem, the practical cross-eye jammer had to be truly-retrodirective. As no retrodirective cross-eye jammer results were available in the literature, a need also existed for a method to implement and calibrate the jammer.

To address the problem, a retrodirective repeater, which was configured as a cross-eye jammer, was

implemented by using a bladeRF 2.0 SDR. The retrodirectivity was achieved by creating two internal jammer paths in the SDR, and connecting the device to two log-periodic antennas in a Van Atta configuration by using off-the-shelf power dividers. The software of the jammer was implemented in GNU Radio, where the parameters of the jammer could be adjusted in real-time on a GUI.

To test the cross-eye jammer, a phase-comparison monopulse radar was implemented by using a bladeRF 2.0 SDR. The monopulse radar operated by transmitting a single LFM pulse and listening for radar return signals on two of the SDR receive channels. The processing of the radar was done by applying pulse compression to the received signal and using peak detection to determine whether radar return signals were present. In the case of a return signal being found, the sum- and difference-channel returns were calculated for the signal. The monopulse ratio was calculated by dividing the difference- by the sum-channel and taking the imaginary part of the result. The indicated angle corresponding to the calculated monopulse ratio was then calculated by using the phase-comparison monopulse ratio equation and solving for the angle.

The cross-eye jammer was tested against the monopulse radar in an anechoic chamber. Before commencing the experiments, the radar was calibrated by using the repeater in its beacon configuration and adjusting the magnitudes and phases of the radar channels to ensure a null in the difference-channel return at broadside.

A new method of calibrating cross-eye jammers was developed and implemented to ensure that the magnitudes of the jammer paths are close to equal in magnitude and that the phase difference between the paths are almost 180°. The calibration was done by minimising the sum-channel antenna pattern by adjusting the magnitude and phase of one of the jammer paths until the optimal values of the amplitude factor and phase difference between repeater paths were achieved.

For the first three experiments, the radar antennas were placed on the positioner in the anechoic chamber while facing the calibrated repeater. Radar measurements were made at each rotation of the radar. The first experiment tested the radar by using a beacon, as this could be used to determine the monopulse antenna patterns in the anechoic environment in a controlled manner. For the second experiment, the repeater was configured to have only one path enabled at a time. This was done to obtain data on the true positions of the repeater antennas from the perspective of the radar. The third experiment was the testing of the cross-eye jammer's ability to create angular errors in radars. The

last three experiments used the same repeater configurations as the first three, but with the repeater antennas now mounted on the positioner. By rotating the repeater antennas, the retrodirectivity of the repeater in both its beacon and cross-eye jammer configurations could be tested.

The main findings of the study are summarised below.

1. **Significant Angular Errors Induced in the Radar due to a High Cross-Eye Gain**

   It was shown that the repeater in its cross-eye jammer configuration could induce large angular errors in the monopulse radar. On broadside of the radar, an angular error of almost 10° was made, for jammer antennas separated 0.324 m apart. This equated to the apparent target being almost 1 m from the closest antenna, considering that the range of the jammer from the radar was determined to be around 6.4 m for this experiment. The angular error was much higher at negative radar rotations but lower at positive radar rotations. This was because the target platform's apparent angular position was to the radar's side that corresponded to positive radar rotation angles.

   The parameters estimated by the optimisation process showed that the cross-eye gain for the case where the radar antennas were mounted on the positioner in the presence of the jammer was about 10 ($a = -1.30$ dB and $\phi = 175.35°$). However, the cross-eye gain for the case of the repeater antennas on the positioner was found to be only about 5 ($a = -0.28$ dB and $\phi = 174.02°$). Even though this was less than in the first case, the angular error was large as the separation between the jammer antennas were larger. It should be noted that as the values of the cross-eye gain were only based on the parameters that were retrieved from the optimisation process, they were only an estimate and not exact. However, it was shown in the measured results that the angular position of the apparent target was far out of the span of the jammer antennas, suggesting large cross-eye gain values. This was reinforced by the indicated angle of the apparent target platform always being much larger than 0°, with a minimum of around 9°. Finally, the large angular errors were induced with a cross-eye jammer that was implemented on a bladeRF 2.0 SDR. This proved that low-cost SDRs could be used to implement cross-eye jammers with significant cross-eye gains. However, it should be noted that the high latency in such devices would prohibit the jammers from being operational outside of controlled laboratory environments.

2. **Tracking Radar Lock**

   It was shown that the indicated angle of the radar in the presence of the jammer was never near 0°. This suggested that a tracking radar would not only experience an angular error due to the

cross-eye jammer itself but would also not be able to lock onto the target platform and track it.

3. **Jammer Calibration Technique**

   The large angular errors induced in the monopulse radar prove that the repeater was configured as a cross-eye jammer. This means that the method that was used to calibrate the jammer was very effective. This method could be used to calibrate cross-eye jammers in the field and could even help prevent cross-eye jammers from turning into beacons due to drifting jammer parameters.

4. **Retrodirectivity of the Repeater and Jammer**

   It was shown in the results that the indicated angle that was measured by the radar followed the theoretical indicated angle closely. The indicated angle was constant around broadside of the jammer but varied as the jammer rotation approached the extreme angles. This was expected as the projected distance between the jammer antennas, from the perspective of the radar, changed as they were rotated. Furthermore, the performance of the jammer did not decrease as the repeater antennas were rotated. This proved that the repeater was truly-retrodirective in both its beacon and cross-eye jammer configurations.

5. **Validation of Previous Analyses**

   It was shown that the measured results deviated significantly from the linear-fit model. This was expected as the linear-fit model assumed the sum- and difference-channel antenna patterns to be linear – something that was only true at broadside of the radar. However, it was shown that the extended cross-eye jamming model represented the measured results very well, and only small deviations were present, except for a deviation around broadside of the radar. These deviations are believed to be caused by mutual coupling in the radar antennas, but more measurements are needed to validate this theory. By considering the results, it is conclusive that the extended analysis is the best model for a retrodirective cross-eye jammer found in the literature to date.

7.2 FUTURE RESEARCH

Possible topics for future research are summarised below.

1. **Improvement of Results**

   There are two aspects of the practical results that could be improved upon in future research. The first is the use of a practical setup that is closer to the ideal. This would remove the need to calibrate the results after taking the measurements. The second aspect would be the use of a monopulse radar with greater isolation between antennas. This is needed to confirm that the deviations in the results were caused by mutual coupling, as is believed.

2. **Practical Testing of Platform Skin Return**

   Platform skin return can be defined as the adverse effect of the radar return from the target platform itself when using a jamming system to protect the target platform from radar threats [19], [44], [45]. A cross-eye jammer should operate at a sufficient power level to ensure that the radar detects the jamming signal and not the return from the target platform itself. The only results of platform skin return are confined to mathematical analyses and simulation. An author suggests that a JSR of at least 15 dB is needed to effectively deceive a monopulse radar with a cross-eye jammer [19]. Practical results are needed to validate the minimum value of the JSR, and can be obtained by artificially creating platform skin return with a controllable power level alongside the cross-eye jammer in this study.

3. **Practical Testing of Multi-Loop Cross-Eye Jamming**

   It is suggested that by using multiple cross-eye jammer loops, instead of one loop as in this dissertation, that higher cross-eye gains could be achieved for less strict cross-eye parameter tolerances, and that lower JSR values could be needed to effectively deceive radar systems [46]. However, by using multiple cross-eye jammer loops, differences between the path lengths are created, which could potentially transform a cross-eye jammer into a beacon [20], [47], [48]. Experimental results are needed to determine the practical effects of using multiple cross-eye loops and to investigate the effects of path-length differences between these loops. This can be done by duplicating the cross-eye jammer in this dissertation and creating a multiloop system with adjustable jammer element separations. It will likely be advantageous to synchronise the clocks of the two jammers SDRs to create constant, non-drifting phase differences between the jammer loops.

4. **Theoretical and Practical Effects of Environmental Reflections when using Different Jammer Antennas for Reception and Transmission**

   The analyses of cross-eye jamming only consider the case where the identical antennas are used to transmit and receive on the side of the jammer [9], [11], [12], [16]. However, this might not be the case in practice due to constraints in the setup. When the same antennas are used for transmission and reception, the signal travels the same path to and from the jammer. This leads to the cancelling of any environmental reflections. When separate antennas are used for reception and transmission, the signals to and from the jammer no longer travels the same path, and environmental reflections may adversely affect the performance of the jammer. The most considerable concern in this matter is for naval implementations, as the ocean is an enormous reflecting surface [16]. Theoretical analyses, validated with practical experiments, are needed to

determine the effects of using different jammer antennas for reception and transmission in the presence of reflecting bodies.

REFERENCES

[1] F. Neri, *Introduction to electronic defense systems*, 2nd ed. North Carolina, USA: SciTech Publishing, 2006.

[2] A. Price, *Instruments of darkness: the history of electronic warfare 1939–1945*. Barnsley, UK: Frontline Books, 2017.

[3] A. De Martino, *Introduction to modern EW systems*. Boston, USA: Artech House, 2010.

[4] S. M. Sherman and D. K. Barton, *Monopulse principles and techniques*, 2nd ed. Boston,USA: Artech House, 2011.

[5] M. I. Skolnik, *Radar handbook*, 3rd ed. Boston, USA: McGraw-Hill, 1990.

[6] D. Adamy, *EW 101: a first course in electronic warfare*. Norwood, USA: Artech House, 2000.

[7] D. C. Schleher, *Introduction to electronic warfare*. Norwood, USA: Artech House, 1986.

[8] F. Neri, "Anti-monopulse jamming Techniques," in *2011 SBMO/IEEE MTT-S International Microwave and Optoelectronics Conference (IMOC 2011)*, vol. 2, Aug. 2002, pp. 43–50.

[9] W. P. du Plessis, "A comprehensive investigation of retrodirective cross-eye jamming," Ph.D. dissertation, University of Pretoria, South Africa, 2010.

[10] D. D. Howard, "Radar target angular scintillation in tracking and guidance systems based on echo signal phase front distortion," in *Proceedings of The National Engineering Conference*, vol. 15, 1959, reprinted in Radars, Vol. 4, radar resolution & multipath effects, David K.Barton, Ed., Artech House, 1975.

[11] S. A. Vakin and L. N. Shustov, "Principles of jamming and electronic reconnaissance - Volume I," US Air Force, Tech. Rep. FTD-MT-24-115-69, AD692642, 1969.

[12] L. B. van Brunt, *Applied ECM*. Dunn Loring, Virginia: EW Engineering, 1978, vol. 1.

[13] W. P. du Plessis, J. W. Odendaal, and J. Joubert, "Extended analysis of retrodirective cross-eye jamming," *IEEE Transactions on Antennas and Propagation*, vol. 57, no. 9, pp. 2803–2806, Sept. 2009.

[14] W. P. du Plessis, J. W. Odendaal, and J. Joubert, "Experimental simulation of retrodirective cross-eye jamming," *IEEE Transactions on Aerospace and Electronic Systems*, vol. 47, no. 1, pp. 734–740, Jan. 2011.

[15] F. Neri, "Experimental testing on cross-eye jamming," presented at The 37th Annual AOC International Symposium & Convention, Las Vegas, USA, 1-4 Oct. 2000.

[16] L. Falk, "Cross-eye jamming of monopulse radar," in *2007 International Waveform Diversity and Design Conference (WDD 2006)*, Oct. 2007, pp. 209–213.

[17] Y. Jang, J. Park, C. Lee, I. Kim, G. Kim, and S. Cho, "Performance experiment of the angle deception of cross-eye jamming against a monopulse sensor," *Journal of Electromagnetic Engineering and Science*, vol. 29, no. 2, pp. 146–149, Feb 2018.

[18] A. Golden, *Radar electronic warfare*. New York, USA: American Institute of Aeronautics and Astronautics, Inc., 1987.

[19] W. P. du Plessis, "Platform skin return and retrodirective cross-eye jamming," *IEEE Transactions on Aerospace and Electronic Systems*, vol. 48, no. 1, pp. 490–501, Jan. 2012.

[20] W. P. du Plessis, "Path-length effects in multiloop retrodirective cross-eye jamming," *IEEE Antennas and Wireless Propagation Letters*, vol. 15, pp. 626–629, Aug. 2015.

[21] B. Petersson, "Modeling of a retrodirective channel with active antenna arrays for cross-eye jamming," Licentiate Thesis, KTH Royal Institute of Technology, Sweden, 2017.

[22] W. P. du Plessis, J. W. Odendaal, and J. Joubert, "Tolerance analysis of cross-eye jamming systems," *IEEE Transactions on Aerospace and Electronic Systems*, vol. 47, no. 1, pp. 740–745, Jan. 2011.

[23] F. Pieterse and W. P. du Plessis, "Retrodirective cross-eye jammer implementation using software-defined radio (SDR)," in *2021 IEEE Radar Conference (RadarConf21)*, 2021, pp. 1–4.

[24] G. W. Stimson, *Introduction to Airborne Radar*, 2nd ed. Mendham: SciTech Publishing, 1998.

[25] F. T. Ulaby, E. Michielssen, and U. Ravaioli, *Fundamentals of applied electromagnetics*, 6th ed. Boston, USA: Prentice Hall, 2010.

[26] B. P. Lathi and Z. Ding, *Modern digital and analog communication systems*, 4th ed. New York, USA: Oxford University Press, 2010.

[27] D. Halliday, R. Resnick, and J. Walker, *Principles of physics*, 9th ed. Chichester, UK: John Wiley and Sons Ltd, 2010.

[28] D. R. Rhodes, *Introduction to monopulse*. Artech House, 1980, reprint of the edition published by McGraw-Hill Book Company, Inc., 1959.

[29] R. A. Ross and M. E. Bechtel, "Scattering-center theory and radar glint analysis," *IEEE Transactions on Aerospace and Electronic Systems*, vol. 4, no. 5, pp. 756–762, Sept. 1968.

[30] K. S. B. Yau, "Development of a passive retrodirective van atta array reflector at X-band," in *2013 International Conference on Radar*, 2013, pp. 398–402.

[31] L. C. Van Atta, "Electromagnetic reflector," U.S.A. Patent 2 908 002, Oct. 6, 1959.

[32] Nuand, "bladeRF 2.0 micro – Nuand," Nuand.com. https://www.nuand.com/bladerf-2-0-micro/ (Accessed 16 Feb. 2021).

[33] W. P. du Plessis, "Modelling monopulse antenna patterns," in *2013 Saudi International Electronics, Communications and Photonics Conference (SIECPC)*, Riyadh, Saudi Arabia, 27-30 Apr. 2013, pp. 1–5.

[34] J. E. Meade, "Target considerations," in *Guidance*, A. S. Locke, Ed. Princeton, USA: D. Van Nostrand, 1955, ch. 11, pp. 435–444.

[35] P. E. Redmill, "The principles of artificial glint jamming ("cross eye")," Royal Aircraft Establishment (Farnborough), Tech. note RAD. 831, Mar. 1963.

[36] H. C. Yin and P. K. Huang, "Unification and comparison between two concepts of radar target angular glint," *IEEE Transactions on Aerospace and Electronic Systems*, vol. 31, no. 2, pp. 778–783, 1995.

[37] H. C. Yin and P. K. Huang, "Further comparison between two concepts of radar target angular glint," *IEEE Transactions on Aerospace and Electronic Systems*, vol. 44, no. 1, pp. 372–380, 2008.

[38] P. Kajenski, "Comparison of two theories of angle glint: polarization considerations," *IEEE Transactions on Aerospace and Electronic Systems*, vol. 42, no. 1, pp. 206–210, 2006.

[39] Analog Devices, "RF agile transceiver," AD9361 datasheet, Sept. 2013 [Revised Nov. 2016].

[40] Ettus Research, "PCB-LP antenna," LP0965 datasheet, Jan. 2012.

[41] Mini-Circuits, "Power splitter/combiner," ZX10-2-71+ datasheet, rev. J.

[42] W. P. du Plessis, private communication, Apr. 2021.

[43] W. L. Stutzman and G. A. Thiele, *Antenna theory and design*, 2nd ed. New York, USA: John Wiley & Sons, Inc., 1998.

[44] T. Liu, Z. Liu, D. Liao, and X. Wei, "Platform skin return and multiple-element linear retrodirective cross-eye jamming," *IEEE Transactions on Aerospace and Electronic Systems*, vol. 52, no. 5, pp. 821–835, May 2016.

[45] W. P. du Plessis, "Limiting apparent target position in skin-return influenced cross-eye jamming," *IEEE Transactions on Aerospace and Electronic Systems*, vol. 49, no. 3, pp. 2097–2101, Jul. 2013.

[46] W. P. du Plessis, "Cross-eye gain in multiloop retrodirective cross-eye jamming," *IEEE Transactions on Aerospace and Electronic Systems*, vol. 52, no. 4, pp. 875–882, Apr. 2016.

[47] W. P. du Plessis, "Analysis of path-length effects in multiloop cross-eye jamming," *IEEE Transactions on Aerospace and Electronic Systems*, vol. 53, no. 10, pp. 2266–2276, Oct. 2017.

[48] W. P. du Plessis, "Path-length effects in multiloop retrodirective cross-eye jamming," *IEEE Antennas and Wireless Propagation Letters*, vol. 15, pp. 626–629, Aug. 2016.

ADDENDUM A DERIVATIONS AND EQUATIONS

A.1 MATHEMATICAL IDENTITIES

The trigonometric identities that were used in the simplification of terms in the extended cross-eye jamming analysis are given by

$$\sin(A \pm B) = \sin A \cos B \pm \cos A \sin B \,, \tag{A.1}$$

$$\cos(A \pm B) = \cos A \cos B \mp \sin A \sin B \,, \tag{A.2}$$

and

$$\sin(A \pm B) = \sin A \cos B \pm \cos A \sin B \,. \tag{A.3}$$

The well-known Euler's identity is given by

$$e^{j\phi} = \cos(\phi) + j\sin(\phi) \,. \tag{A.4}$$

A.2 CROSS-EYE JAMMING SIMPLIFICATIONS

The simplification of the multiplied cosine term in the sum-channel antenna pattern calculation for the extended cross-eye jamming analysis is done as

$$\cos(k+k_c)\cos(k-k_c) = [\cos(k)\cos(k_c) - \sin(k)\sin(k_c)][\cos(k)\cos(k_c) + \sin(k)\sin(k_c)] \tag{A.5}$$

$$= \cos^2(k)\cos^2(k_c) - \sin^2(k)\sin^2(k_c) \tag{A.6}$$

$$= \frac{1}{2}[1+\cos(2k)]\frac{1}{2}[1+\cos(2k_c)] - \frac{1}{2}[1-\cos(2k)]\frac{1}{2}[1-\cos(2k_c)] \tag{A.7}$$

$$= \frac{1}{4}[1+\cos(2k)\cos(2k_c)+\cos(2k)+\cos(2k_c)] - \frac{1}{4}[1+\cos(2k)\cos(2k_c)-\cos(2k)-\cos(2k_c)] \tag{A.8}$$

$$= \frac{1}{4}[2\cos(2k)+2\cos(2k_c)] \tag{A.9}$$

$$= \frac{1}{2}[\cos(2k)+\cos(2k_c)]\,. \tag{A.10}$$

Similarly, the simplifications of the terms were a sine and cosine are multiplied in the difference-channel antenna pattern derivation, for the extended cross-eye jamming analysis, are done as

$$\sin(k+k_c)\cos(k-k_c) = [\sin(k)\cos(k_c)+\cos(k)\sin(k_c)][\cos(k)\cos(k_c)+\sin(k)\sin(k_c)] \tag{A.11}$$

$$= \sin(k)\cos(k)\cos^2(k_c) + \sin(k)\cos(k)\sin^2(k_c) + \sin(k_c)\cos(k_c)\cos^2(k) + \sin(k_c)cos(k_c)\sin^2(k) \tag{A.12}$$

$$= \sin(k)\cos(k)[\sin^2(k_c)+\cos^2(k_c)] + \sin(k_c)\cos(k_c)[\sin^2(k)+\cos^2(k)] \tag{A.13}$$

$$= \sin(k)\cos(k)+\sin(k_c)\cos(k_c) \tag{A.14}$$

$$= \frac{1}{2}[\sin(2k)+\sin(2k_c)]\,, \tag{A.15}$$

and

$$\sin(k-k_c)\cos(k+k_c) = [\sin(k)\cos(k_c)-\cos(k)\sin(k_c)][\cos(k)\cos(k_c)-\sin(k)\sin(k_c)] \quad \text{(A.16)}$$

$$= \sin(k)\cos(k)\cos^2(k_c)+\sin(k)\cos(k)\sin^2(k_c)$$

$$-\sin(k_c)\cos(k_c)\cos^2(k)-\sin(k_c)\cos(k_c)\sin^2(k) \quad \text{(A.17)}$$

$$= \sin(k)\cos(k)[\sin^2(k_c)+\cos^2(k_c)]$$

$$-\sin(k_c)\cos(k_c)[\sin^2(k)+\cos^2(k)] \quad \text{(A.18)}$$

$$= \sin(k)\cos(k)-\sin(k_c)\cos(k_c) \quad \text{(A.19)}$$

$$= \frac{1}{2}[\sin(2k)-\sin(2k_c)]\,. \quad \text{(A.20)}$$

ADDENDUM B RESULTS BEFORE POST-MEASUREMENT CALIBRATION

B.1 OVERVIEW

The results of the radar in the presence of the repeater, before post-measurement calibration were done, are given in this addendum. These results are only presented to support the calibrated results in the dissertation. Note that the results in this section were obtained by using the monopulse radar that was calibrated for a null at broadside for its difference-channel patter, and a cross-eye jammer that was calibrated for the ideal values of the magnitude factor and phase difference between paths. The results were just not corrected for deviations of the setup from the ideal setup by using the optimisation method yet.

B.2 RADAR ROTATION

The results for the case where the radar antennas were placed on the positioner are given in this section. Figure B.1 shows the results of the radar against the beacon. It can be seen that the measured data sets are almost identical. The indicated angle of the radar can be seen to be a linear function of time, that deviates somewhat from the theoretical function.

The results of the radar in the presence of the repeater, with only one repeater path at time enabled, can be seen in Figure B.2. These results played an important role in the post-measurement calibration, as the data described the angular positions of the jammer antennas.

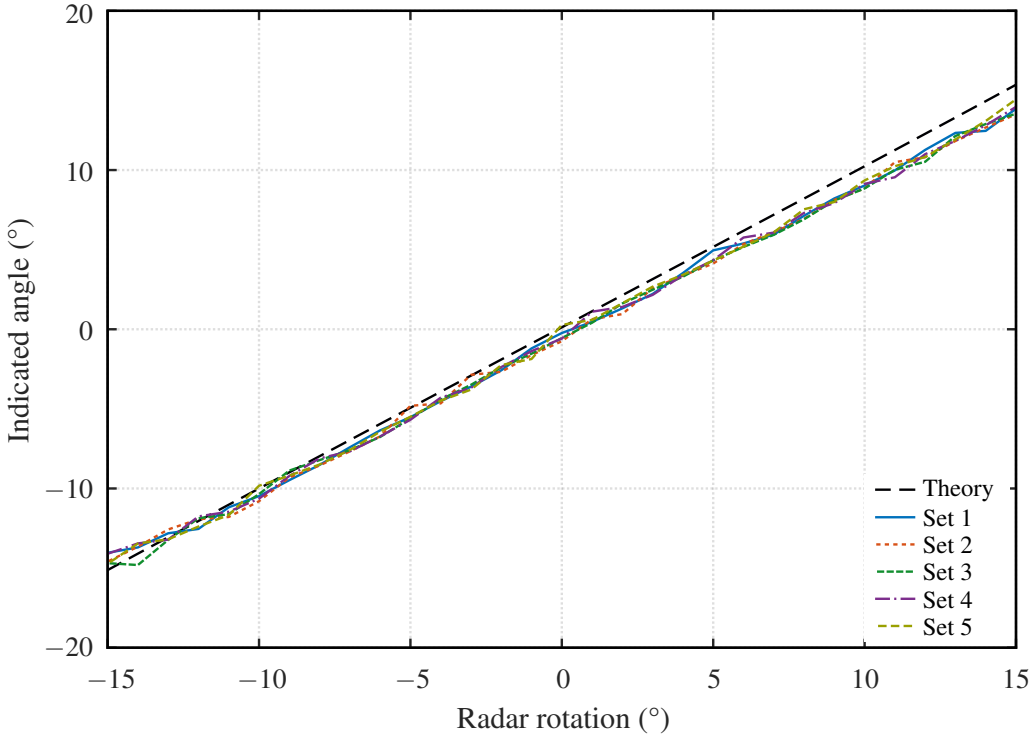

Figure B.1. Plots of the indicated angle of the monopulse radar against a beacon.

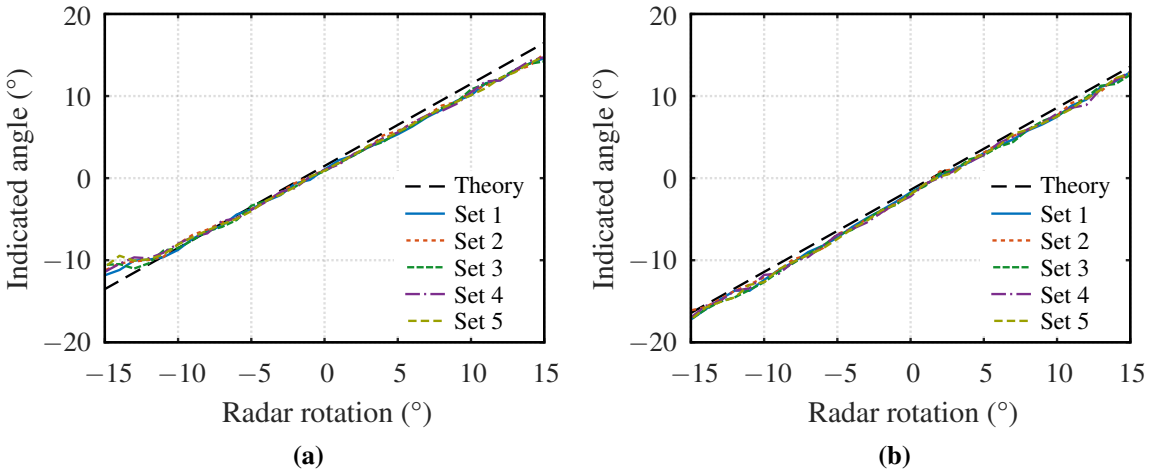

Figure B.2. Plots of the indicated angle of the monopulse radar against the repeater, with (a) only the first path, and (b) only the second path of the repeater switched on.

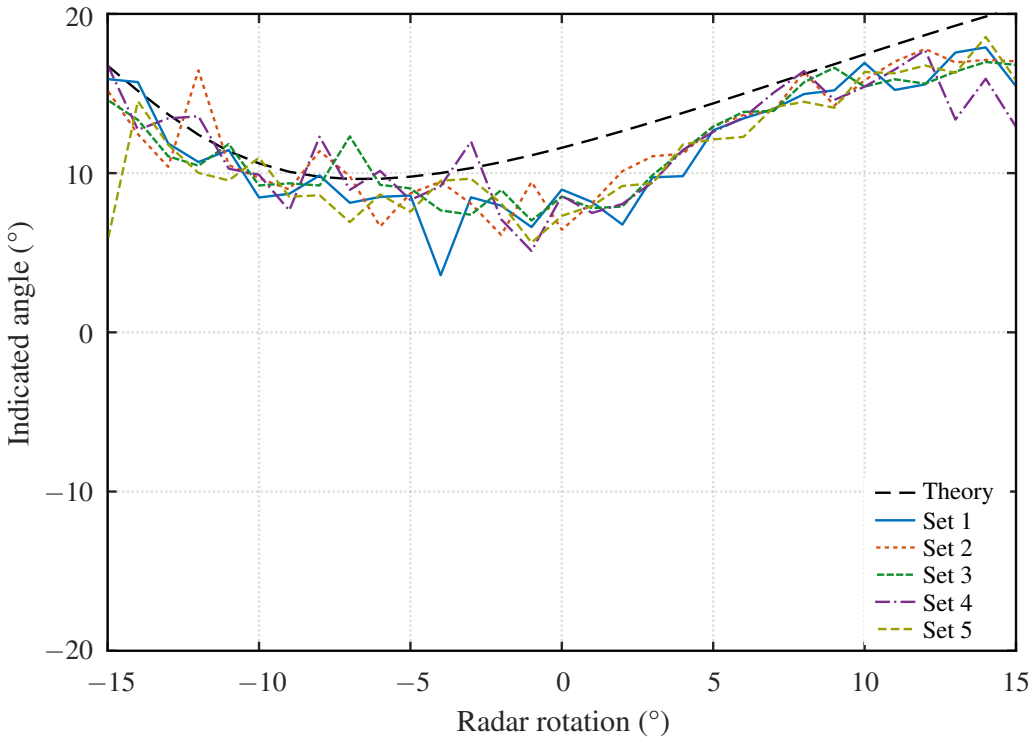

Figure B.3. Plots of the indicated angle of the monopulse radar against the repeater, with the repeater in its cross-eye jammer configuration.

The jammer results before post-measurement calibration are given in Figure B.3. It can be seen that, as with the results after post-measurement calibration, that very large angular errors were induced in the radar. The results of the jammer here are very similar to that of that after post-measurement calibration, which suggests that the effects of the setup discrepancies were small.

B.3 REPEATER ROTATION

The results of the radar, with the repeater antennas mounted on the positioner, are given in this section. The results here were not corrected for setup discrepancies. The results of the radar in the presence of the repeater, configured as beacon, are shown in Figure B.4. It can be seen that the results show very little deviation from the theoretical, and suggest that the beacon was retrodirective. The setup discrepancies did not affect these results adversely.

The results of the radar in the presence of the repeater in its cross-eye jammer configuration, with the repeater antennas rotated by the positioner, are shown in Figure B.5. It is clear that the jammer results,

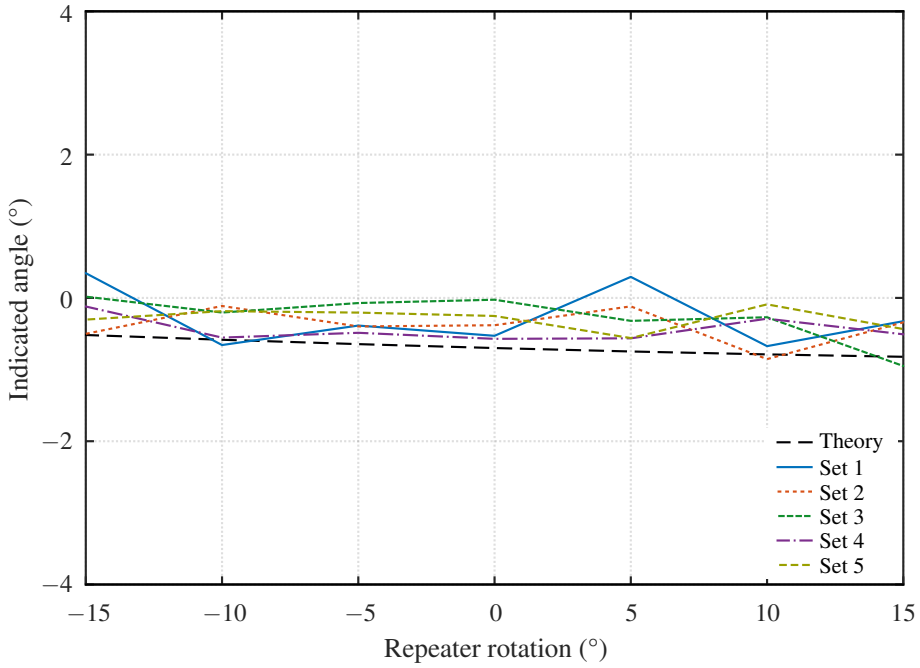

Figure B.4. Plots of the indicated angle of the monopulse radar against the repeater, with the repeater in its beacon configuration.

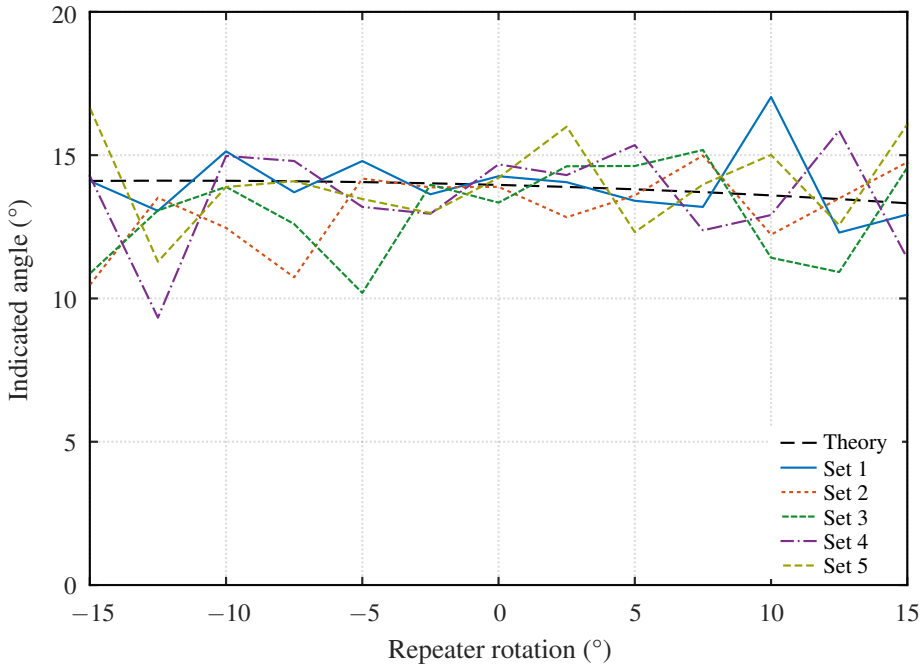

Figure B.5. Plots of the indicated angle of the monopulse radar against the repeater, with the repeater in its cross-eye jammer configuration.

even though noisy, tend to the theoretical results, where large angular errors can be seen. These results show that the cross-eye jammer was retrodirective. As with the beacon, the setup deviations did not noticeably affect the results.